Studies on crystal structure of functional rare earth sesquioxides at high pressures

By

K. A. IRSHAD
PHYS 02 2013 04 004

Indira Gandhi Centre for Atomic Research,
Kalpakkam, India

A thesis submitted to the
Board of Studies in Physical Sciences

In partial fulfillment of requirements
for the Degree of
DOCTOR OF PHILOSOPHY
of
HOMI BHABHA NATIONAL INSTITUTE

August, 2018

Homi Bhabha National Institute

Recommendations of the Viva Voce Committee

As members of the Viva Voce Committee, we certify that we have read the dissertation prepared by Mr. K. A. Irshad entitled " Studies on crystal structure of functional rare earth sesquioxides at high pressures" and recommend that it may be accepted as fulfilling the thesis requirement for the award of Degree of Doctor of Philosophy.

G. Amarendra
Chairman - Dr. G. Amarendra **Date:**

Guide / Convener - Dr. N. V. Chandra Shekar N.V. Chandra Sh **Date:** 19/12/2018

Examiner - Dr. G. S. Vaitheeswaran G. Vaitheeswaran **Date:** 19/12/2018

Member 1- Dr. T. R. Ravindran TR Ravindran **Date:** 19/12/2018

Member 2- Dr. Ravi Chinnappan **Date:** 19/12/2018

Final approval and acceptance of this thesis is contingent upon the candidate's submission of the final copies of the thesis to HBNI.

I hereby certify that I have read this thesis prepared under my direction and recommend that it may be accepted as fulfilling the thesis requirement.

Date: 19/12/2018

Place: IGCAR, Kalpakkam

N.V. Chandra Sh

Dr. N. V. Chandra Shekar

Guide

STATEMENT BY AUTHOR

This dissertation has been submitted in partial fulfillment of requirements for an advanced degree at Homi Bhabha National Institute (HBNI) and is deposited in the Library to be made available to borrowers under rules of the HBNI.

Brief quotations from this dissertation are allowable without special permission, provided that accurate acknowledgement of source is made. Requests for permission for extended quotation from or reproduction of this manuscript in whole or in part may be granted by the Competent Authority of HBNI when in his or her judgment the proposed use of the material is in the interests of scholarship. In all other instances, however, permission must be obtained from the author.

19/12/2018

K. A. Irshad

DECLARATION

I, hereby declare that the investigation presented in the thesis has been carried out by me. The work is original and has not been submitted earlier as a whole or in part for a degree / diploma at this or any other Institution / University.

19/12/2018

K. A. Irshad

List of Publications arising from the thesis

Journal

1. X-ray diffraction and Raman studies on Ho: Eu_2O_3. **K. A. Irshad**, N. V. Chandra Shekar, T. R. Ravindran, V. Srihari and K. K. Pandey, Journal of Molecular Structure **1128**, 325-329 (2017).
   doi: http://dx.doi.org/10.1016/j.molstruc.2016.08.077
2. A novel and simple X-ray slit for diamond anvil cell based X-ray diffraction experiments. **K. A. Irshad**, N. R. S. Kumar and N. V. C. Shekar, Measurement Science and Technology **28** (4), 047002 (2017).
   doi: https://doi.org/10.1088/1361-6501/aa5e25
3. Anomalous lattice compressibility of hexagonal Eu_2O_3. **K. A. Irshad** and N. V. Chandra Shekar, Materials Chemistry and Physics **195**, 88-93 (2017).
   doi: http://doi.org/10.1016/j.matchemphys.2017.04.012
4. High pressure structural phase transitions in Ho: Eu_2O_3. **K. A. Irshad**, N. V. Chandra Shekar, V. Srihari, K. K. Pandey and S. Kalavathi, Journal of Alloys and Compounds **725**, 911-915 (2017).
   doi: http://dx.doi.org/10.1016/j.jallcom.2017.07.224
5. Presure induced structural phase transition in rare earth sesquioxide Tm_2O_3 : Experiment and *ab initio* calculations. **K. A. Irshad**, P. Anees, Shradhanjali Sahoo, N. R. Sanjay Kumar, V. Srihari, S. Kalavathi and N. V. Chandra Shekar, Journal of Applied Physics **124** (15), 155901 (2018).
   doi: https://doi.org/10.1063/1.5049223
6. Micro strain assisted polymorphic phase transitions in $(Eu_{1-x}La_x)_2O_3$. **K. A. Irshad**, A. Saikumaran, V. Srihari, S. Kalavathi and N. V. Chandra Shekar, Journal of Applied Crystallography, Journal of Applied Crystallography **52** (1) (2019).
   doi: https://doi.org/10.1107/S1600576718016989
7. Pressure induced anomalous lattice compression and layer movement in the hexagonal La_2O_3, **K. A. Irshad**, P. Anees, R. Rajitha, T. R. Ravindran, V. Srihari, S. Kalavathi and N. V. Chandra Shekar (**Under Correction**)
8. High pressure phase structure of $(Eu_{1-x}La_x)_2O_3$, **K. A. Irshad**, V. Srihari, S. Kalavathi and N. V. Chandra Shekar, (**Under Correction**)

Conferences

1. Polymorphism in rare earth sesquioxides: dependence on pressure and cationic radii. **K. A. Irshad**, N. V. Chandrashekar and S. Kalavathi, 24th Congress and General Assembly of the International Union of Crystallography, 21–28 August 2017, Hyderabad**,** Acta Crystallographica Section A **73** (a2), C1256 (2017). doi: http://dx.doi.org/10.1107/S2053273317083188
2. High Pressure Structural Phase Transition in Tm_2O_3 . **K. A. Irshad**, N. V. Chandra Shekar and S. Kalavathi, 2nd International Conference on Condensed Matter and Applied Physics (2017), Bikaner, Rajasthan.
3. Investigation of pressure-concentration (P-X) phase diagram for rare earth mixed oxide ceramic system: $(Eu_{1-x}Ho_x)_2O_3$. **K. A. Irshad** and N. V. Chandra Shekar MRSI, 27th AGM, 18-20 Feb. 2016, CSIR North East Institute of Science and Technology, Jorhat, p.46

Publications not included in the thesis

1. High pressure studies on Thorium-Praseodymium mixed oxides. **K. A. Irshad**, D. Sanjay Kumar, G. Paneerselvam, K. Ananthasivan, N. V. Chandra Shekar and S. Kalavathi, Journal of Nuclear Materials **498** (Supplement C), 221-226 (2018). doi: https://doi.org/10.1016/j.jnucmat.2017.10.029
2. High Pressure Studies on Thorium-Praseodymium Mixed Oxides. **K. A. Irshad**, N. V. C. Shekar, G. Paneerselvam, D. S. Kumar and K. Ananthasivan, (61st DAE Solid State Physics Symposium, KIIT University, Bhubaneswar, 2017).

19/12/2018

K A Irshad

DEDICATIONS

Devoted to my Father and Mother for encouraging me how to confront the impediments and not to give up

ACKNOWLEDGEMENTS

I am deeply grateful to a number of people who have been directly or indirectly instrumental in getting this thesis to completion and shaping up my personal and academic career. However, some deserve special mentions.

In the first place, I would like to thank Dr. N. V. Chandra Shekar, my adviser and thesis supervisor, who has extended his unflinching support both academically and personally throughout the tenure of my thesis works. I truly enjoyed the friendly environment and freedom of research under his supervision. It is without his timely help and constant support the thesis work would not have been in its present shape.

Besides my adviser, I am also thankful to my Doctoral Committee (DC) members, Dr. G. Amarendra (Chairman), Dr. T. R. Ravindran and Dr. Ravi Chinnappan and the Ex-DC members, Dr. P. Ch. Sahu, Dr. B. V. R. Tata, Dr. A. Arulraj and Dr. K. V. G. Kutty. Their creative criticisms and timely involvements have helped me in crossing the obstacles and to step forward in the right direction.

I appreciate the members of High Pressure Physics section (HPPS) for their collective effort. I thank Dr. S. Kalavathi, Head, HPPS, for continuous assessment, feedbacks and careful review of my thesis work amidst her busy schedules. I must be indebted to Dr. N. R. Sanjay Kumar for the fruitful discussions and advices. I admire his simple, creative and logical approach towards every scientific obstacle. I thank Dr. M. Shekar for his leading role in developing my diamond anvil cell skills. I also thank Shri. L. M. sundaram, Dr. Balmukund Shukla, Mr. Anand Kumar, Ms. Arpita, Dr. G. Shwetha and Mr. Shitikantha for creating a friendly scientific environment in the lab.

I also appreciate the efforts of my collaborators, Dr. V. Srihari and Dr. K. K. Pandey from RRCAT, Indore, Dr. P. Anees from MPD, IGCAR, Dr. R. Mythili and Mr. A. Saikumaran from PMG, IGCAR and Ms. Sharadhanjali Sahu from CMPD, IGCAR for *their scientific inputs and timely help in completing my experiments. I also thank Dr. V. Sridharan from, CMPD, IGCAR for providing the lab facility for sample synthesis.*

I thank, Dr. A. K. Bhaduri, Director IGCAR, Dr. P. R. Vasudeva Rao and Dr. S. A. V. Sathyamurthi (former Directors, IGCAR) for providing the opportunity to do research over here and IGCAR management for their help and support in all way.

This acknowledgement would not be complete without mentioning the name of my seniors, juniors and my bellowed friends with whom I spent all these years.

Dr. Karthikeyan, Dr. Sivadasan, Dr. Devidas, Dr. Subrata, Dr. Mahendran, Dr. Raghavendra, Dr. Srinivasan, Dr. Greeshma, Dr. Sanjay Kumar and many other seniors, for creating a friendly and inspiring environment.

My fellow friends, who have been with me right from the beginning of my research work, Lakshmanan, Nilakantha, Vairavel, Padmalochan, Zaibudeen and Madhusmita. No formal thanks, but I cherish the moments which we spent together.

My juniors, Saikumaran, Sivakumar, Dilipan, Bala, Ragavendran, Manu, Anoop, Paulson, Sachin, Prince, Guna, Velraj, Arpita, Reshma, Parvathy, Deepitha. Sruthi, Rasitha. Reshmi, Rajitha, Vaishnavi and many others for providing joyful and homely ambience at JRF enclave.

Special thanks to Radhikesh for being my roommate, sharing joys and sorrows and above all for respecting the differences.

I appreciate the sports ambience created by the Inter lab cricket tournament, Intra Enclave Cricket League and Enclave Badminton League.

My deepest appreciation belongs to my family for their patience and understanding, without their love and support over the years none of these would have been possible.

TABLE OF CONTENTS

SYNOPSIS

Rare earth sesquioxides (RES) are known to be an important material owing to the wide spread applications in many of the fields like solid state lasers, solid oxide fuel cells, control rods in nuclear reactors, phosphors, wave guides, scintillating materials and so on[1]. They are also fundamentally interesting materials due to their existence in different polymorphic structures. Depending on the cation size, RESs are known to exist in any of the three polymorphic structures at ambient temperature and pressure (ATP)[1, 2]. The sesquioxides with small cation size (Dy-Lu) follows the C-type (cubic) structure whereas, the large cation sized RES (La-Nd) adopts the A-type (hexagonal) structure. Depending on the thermal history, the medium cation sized RES (Sm-Gd) crystallizes either in the B-type (monoclinic) or in the C-type. In addition to these structure types, they do show X-type (cubic) and H-type (hexagonal) structures at very high temperatures. A systematic investigation revealing the evolution of these structure types as a function of cationic radii is scarce. Hence, it is necessary to do a precise structural characterization with a smooth variation in cationic radii.

Although the cationic radii in the RES's increase in the sequence C→B→A, the molar volume is observed to be decreasing in the same sequence[2]. Considering this fact, a structural sequence of C→B→A is expected to occur under high pressure (HP). In RES with small cation size, the C-type structure is found to be transforming to the A-type through the intermediate B-type. But the medium size RES's do not obey this sequence and instead go through a direct C→A transition[3-5]. In this case, the B-type structure is identified as HP and high temperature (HT) phase[5]. A systematic study on the pressure effect on the solid solutions, having a smooth variation in cationic radii, of intermediate and small cation sized RES can reveal substantial information about the phase structure and transition boundaries of C→A and C→B. In general, the A-type structure is known to be stable under pressure. Hence it has received less attention. The report on the La_2O_3 showed a transition to a novel superlattice structure near 8 GPa whereas, a novel distorted monoclinic phase is predicted for Nd_2O_3 at around 27 GPa[6, 7]. However, no transitions are reported for Ce_2O_3[8]. A recent investigation on A-type Nd_2O_3 has shown an anomalous compression behavior and is reported as an indicative of an isostructural electronic transition as observed in the HP hexagonal phase of Gd_2O_3[9, 10]. It shows that, the reports on the HP behavior of A-type sesquioxides are inconsistent and need to be investigated more carefully and precisely. Above all, across the rare earth series, the transition pressure increases with decreasing cationic radii. Despite this increasing trend, HP studies reported a comparatively lower transition pressure for the C-type Tm_2O_3[2]. Further investigation is necessary to remove this ambiguity.

The present thesis is aimed to understand the cation size dependant high pressure behavior of various RES's. In order to understand the phase behavior, simple RES of C-type, B-type and A-type will be investigated at high pressures. Further to address the simultaneous dependence of cationic radii and pressure, the solid solutions of RES with similar structure and small difference in cationic radii and the solid solutions of RES with dissimilar structure and significant difference in cationic radii will be investigated both at ATP and at high pressures.

The thesis is divided into seven chapters. The content of each chapter is briefly described below:

Chapter 1: This chapter of the thesis will give a brief introduction about the polymorphic structure of RES and their stability with increase/decrease of cationic radii and temperature. A brief discussion about the electronic structure of RES shown by different polymorphic structure types also forms the content of this chapter. The HP behaviour of small, medium and large cation sized RES will be discussed in detail by reviewing the available literature. The objective of the thesis is also stated at the end of this chapter.

Chapter 2: This chapter deals with the HP experimental techniques, characterization tools and analysis methods followed for the works mentioned in the thesis. The generation of high pressure using the Mao-Bell type diamond anvil cell (DAC), alignment of DAC, sample assembly inside the DAC, pressure calibration methods which are adopted for the present thesis work are discussed in detail as subsections to the experimental tools. The details of the instruments/techniques like synchrotron XRD, laboratory XRD, Raman scattering and SEM EDAX used to characterise the samples and the basic principle behind these tools are also discussed here. Finally, in the last section, the basic concepts and details about the Rietveld structure refinement and *ab initio* density functional theory is provided in brief.

Chapter 3: A short account of the novel experimental technique developed for carrying out HPXRD studies is given in chapter 3. Here, the details of design, development and successful testing of a novel internal X-ray slit assembly to carry out laboratory based HPXRD experiments in a Mao Bell type Diamond anvil cell is described. In this assembly, a tiny sheet of lead with a 100 μm hole immediately below the diamond table acts as an X-ray slit. The resolution and statistics of acquired data were compared with the older slit. This novel slit assembly has two major advantages i) eliminates cumbersome and the lengthy procedure usually adopted for alignment of x-ray slit ii) provides high flux and improved resolution due to the comparatively low beam divergence and effective utilization of the maxima of the beam profile. This novel slit assembly is highly beneficial for the HP studies using the laboratory X-ray sources.

Chapter 4: In this chapter, C-type Tm_2O_3, B-type Eu_2O_3 and A-type La_2O_3, each from the small, medium and large cation sized RES respectively are studied at high pressures.

The HP synchrotron XRD and HP Raman studies revealed the irreversible nature of C→B structural phase transition in Tm_2O_3 at ~12 GPa. This is in contradiction with the available literature but fits best to the trend observed in the C-type RES. A bulk modulus of 149(2) GPa and 169(2) GPa for the cubic and monoclinic phase respectively is determined from the experiment and is in good agreement with the values obtained from the *ab initio* DFT calculations, 146 GPa(C-type) and 151 GPa (B-type). Raman modes for the B-type phase of Tm_2O_3 are measured and reported for the first time. The mode Grüneisen parameter of different Raman modes for both C-type and B-type structure of Tm_2O_3 has also been determined. The experimental results are correlated with changes in the DOS near the Fermi level which are indicative of structural instabilities in the parent cubic structure.

HP laboratory XRD is carried out for the B-type Eu_2O_3. A reversible structural phase transition from B→A is observed at 4.3 GPa. A bulk modulus of 159(9) GPa and 165(6) GPa is reported for B-type and A-type structure respectively. In the B-type phase, the axial compressibility follows $\beta_a > \beta_c > \beta_b$. Anomalous lattice compressibility is observed for the HP A-type structure, characterized by pronounced hardening along the *a* axis above 15 GPa. The observed incompressible nature of the hexagonal *a* axis in the pressure range 15-25 GPa is found to be compensated by doubling the compressibility along the *c* axis.

To shed light on the anomalous compressibility observed for the A-type structure, high pressure synchrotron based XRD is carried out for the A-type La_2O_3. The A-type structure is found to be stable up to 26.5 GPa. The *a* axis is found to be compressing up to a critical pressure of 9.7 GPa and then expands in the region 9.7 GPa < P < 19.8 GPa. The Rietveld structure refinement in conjunction with the Stephans anisotropic strain model indicates the onset of this anomaly at an earlier pressure of 5.6 GPa, where an atypical bond compression behavior is observed. A significant increase in the intensity of *100* reflection and a clear decrease in the intensity of *103* reflections under HP suggests a plausible movement of the LaO layers in the opposite direction. Hence, the pressure is engaged in moving these layers rather than compressing along the *a* axis resulting in the observed anomalous compression behaviour. A bulk modulus value of B_0 = 102(5) GPa in the region P ≤ 9.7 GPa and B_0 = 177(3) GPa in the region P ≥ 22.3 GPa is obtained.

The results of this chapter provide a basic understanding of the HP behavior of simple RES.

Chapter 5: This chapter is intended to understand the simultaneous effect of cationic radii and HP on the RES. The synthesis of $(Eu_{1-x}Ho_x)_2O_3$, ($0 \leq x \leq 1$), solid solution, having a smooth variation in cationic radii, by the *chemie douce* method, characterization of these solid solutions using the XRD and Raman scattering will form the first part of this chapter. A single phase solid solutions are obtained for the entire range of compositions. Evolution of crystal structure parameters with change in cationic radii, R_{RE}, is obtained by employing the Rietveld structure refinement. A random cationic distribution in the two crystallographic sites and a translational motion of the RE ion in the 24*d* site was observed. Hardening of Raman modes in the high frequency range reveals an increasing bond strength, hence an increasing structural rigidity with the decrease of average cationic radii, R_{RE}.

In order to understand the effect of cationic radii, HP behavior of these solid solutions was investigated using the in-situ angle dispersive high pressure X-ray diffraction technique. Studies on various compositions of the mixed oxide show that when the average cationic radius, R_{RE} is equivalent to or below 0.9164 Å the system prefers a cubic to monoclinic transition as a function of pressure, whereas average cationic radii equivalent to or above 0.9220 Å prefers a transition from cubic to hexagonal. In the composition range $0.4 \leq x \leq 0.6$ following trend is observed: the bulk modulus goes up after a drastic reduction at x=0.4, whereas, the transition pressure decreases. This is identified as a consequence of the increasing internal pressure induced by the doping. A pressure concentration phase diagram for $(Eu_{1-x}Ho_x)_2O_3$ upto a pressure of 15 GPa is constructed based on the high pressure structural investigations. Average cationic radii $0.9164Å < R_r < 0.9220Å$ is observed to form the phase boundary between cubic to hexagonal and cubic to monoclinic phase transitions.

The results of this chapter provide a systematic understanding of the dependence of rare earth cationic size and pressure on different structure type in the region of small-medium cation size.

Chapter 6 : The objective of this chapter is to understand the phase behaviour of solid solutions of medium and large cation sized RES under HP. Solid solutions, $(Eu_{1-x}La_x)_2O_3$ has been prepared by the *chemie douce* method. The compositions are verified using the energy dispersive spectroscopy (EDS). The scanning electron microscopy (SEM) revealed the irregularly shaped particles in the submicron size. Structural parameters are obtained through Rietveld refinement of the Angle dispersive XRD (ADXRD) data. A structural phase transition from cubic (C-type) to monoclinic (B-type) and subsequently to the hexagonal (A-type) structure has been observed with increasing substitution of La. A detailed analysis on the transition boundaries in terms of their average cationic radii, R_{RE}, shows that, the onset of C→ B transition is at R_{RE}=0.980 Å whereas B→A is at R_{RE}=1.025 Å. A biphasic region of cubic and monoclinic structure is observed for $0.2 \leq x \leq 0.4$ and that of the monoclinic and hexagonal structure is observed for $0.5 \leq x \leq 0.6$. It is found that, the micro strain induced by the difference in the size of the rare earth ions introduces a substitutional disorder in the crystal structure which is a plausible cause for the observed phase transitions in these oxides.

The structural stability and compression behaviour of these solid solutions are investigated using the HP ADXRD. The cubic structure in the region 0.95 Å ≤ R_{RE} < 0.98 Å prefers a C→ A transition with increasing pressure. For the biphasic region of cubic and monoclinic structure, 0.98 Å ≤ R_{RE} < 1.025 Å, a C/B→A transition is preferred under pressure. In the biphasic region of the monoclinic and hexagonal structure, 1.025 Å ≤ R_{RE} <1.055 Å, the B phase is found to be progressing towards the hexagonal A phase under pressure. The pure A phase in the region, 1.055 Å ≤ R_{RE} ≤ 1.10 Å, is structurally stable under HP. The compressibility data shows a monotonous decrease in the bulk modulus of the hexagonal structure with the increasing R_{RE} except for x=0.2 and 0.6. A pressure-concentration (P-x) phase diagram up to a pressure of 25 GPa is constructed from the HPXRD investigation on $(Eu_{1-x}La_x)_2O_3$.

The results of this chapter establish the role of microstrain in driving the C→B→A transition. Also, it provides a systematic understanding of the phase structure of RES in the region of large-medium cation size under HP.

<u>Chapter 7</u> : This chapter gives an overall summary and the salient features of the thesis work along with the scope for the future works.

LIST OF FIGURES

LIST OF TABLES

Chapter 1

Structural phase transitions in rare earth sesquioxides

1.1. Introduction

Rare earth sesquioxides (RES) are RE_2O_3 type compounds, where RE stands for the rare earth atom. All the rare earth atoms together with the oxygen atoms can form stable sesquioxide structure. They play a vital role in many of the technologically important applications in the field of solid state lasers, solid oxide fuel cells, radiation detectors, wave guides, scintillating materials, random access memory (RAM) devices and sensing[11-16]. The entire lanthanide oxide series has been found to be intrinsically hydrophobic in nature. They sustain hydrophobicity even after exposure to harsh environments of high-temperature and abrasion leading to the wide spread applicability as robust hydrophobic surfaces[17]. Improving the properties of materials and implementing them to the large scale industrial applications have always been a challenging task in terms of both fundamental and technological aspects. It has been demonstrated that doping of materials to the pristine samples is a promising way to improve the desired physical properties of materials. High-power solid-state lasers based on rare-earth doped sesquioxides, Lu_2O_3, Sc_2O_3 , and Y_2O_3, as well as different mixed sesquioxides $(Lu_aSc_bY_c)_2O_3$ have been found to be highly efficient[11]. An increase in the electrical conductivity and activation energy with a decrease in the mole percentage of the $Gd_2O_3$was observed in the $Bi_{1-x-y}Ho_xGd_yO_{1.5}$, used as an electrolyte for solid oxide fuel cell applications[12]. Moreover, an enhancement in the Luminescence properties of CeO_2 has been observed by lanthanide doping[18]. However, most of the differences in the physical properties are known to be structure dependent.

1.2. Polymorphism in rare earth sesquioxides

The capability of existing in different structure type for a given compound brought the RESs under the category of the compounds showing Polymorphism. At ambient temperature and pressure (ATP), depending on the cationic radii, RES's are known to exist in the cubic (C-type), monoclinic (B-type) and hexagonal (A-type) polymorphic structures[19]. These polymorphic structures are shown in Fig. 1.1. A complete structural description of the binary rare earth oxide phases known to exist, along with their structural and thermodynamic characteristics, including symmetry types and inter-relationships is available elsewhere in the literature[19, 20]. A brief description about each of the known structure types are given below.

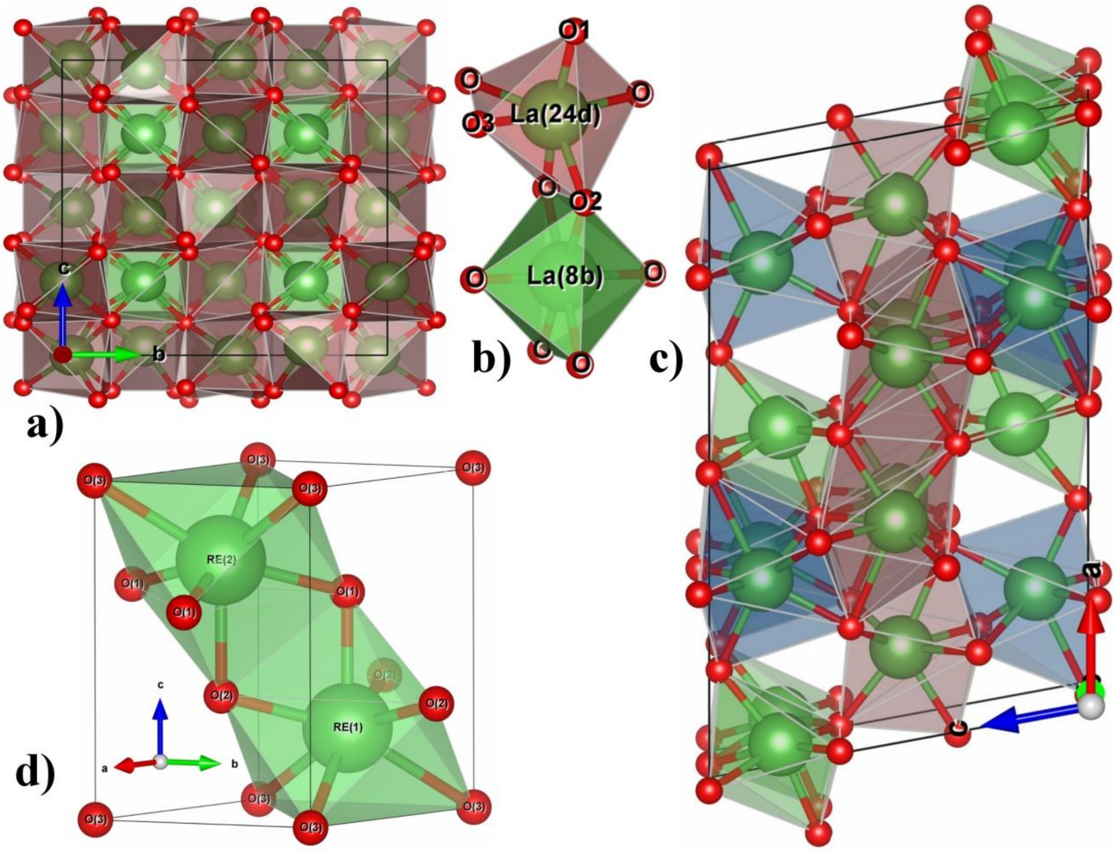

Fig. 1.1 The polymorphic structure types of rare earth sesquioxides: a) C-type cubic structure, b) the octahedral environment in the C-type structure c) B-type monoclinic structure and d) A-type hexagonal structure. The rare earth ions are represented by large spheres of green colour whereas the oxygen is small in size and red in colour. The RE-O6 or RE-O7 polyhedral arrangements centered at the RE cation sites are indicated with different colours.

C-type Cubic structure

The Cubic structure of RES crystallizing in the space group (SG) *Ia-3* is conventionally designated as C-type. This structure can be related to the cubic fluorite type CaF_2 structure (SG: *Fm3m*). Doubling the cubic unit cell of CaF_2 along the three crystallographic axes will result in a cell in close resemblance with the unit cell of C-type RES. In CaF_2, the Fluorine atoms are in cubic (8) co-ordination with Calcium atoms. The C-type structure can be obtained by removing a pair of anions along the body diagonal and face diagonal of the co-ordination cube in an ordered way[20]. As a result, this will form a distorted octahedral environment of oxygen anions around the cation. The structure thus obtained is known as the defect fluorite structure and is same as that of C-type cubic structure. The unit cell of C-type RES consists of 16 formula units with 32 cations distributed over 8*b* (with site symmetry C_{3i}) and 24*d* (with site symmetry C_2) crystallographic sites/Wyckoff positions. The cations at 8*b* and 24*d* are in octahedral coordination with oxygen atoms, sitting at 48*e* general site. The octahedron at 8*b* site is made up of a single bond length, designated as RE(8*b*)-O, whereas three different bond lengths, designated as RE(24*d*)-O1, RE(24*d*)-O2 and RE(24*d*)-O3 forms the octahedron at 24*d* site. This structure is adopted by most of the RES with small cation size (Sm-Lu).

B-type monoclinic structure

The Monoclinic structure of RES crystallizing in the SG C2/*m* is conventionally known as B-type. The unit cell is composed of 6 formula units with 12 cations distributed over three different 4*i* Wyckoff positions. The oxygen atoms reside over four 4*i* and one 2*b* position. In this structure, cations are in 6 and 7 co-ordination with the oxygen atoms. This structure is the stable form of intermediate cation size (Sm_2O_3, Eu_2O_3 and Gd_2O_3) RES, when it is quenched back to ATP from 800°C, 1200°C and 1400°C respectively [21].

A-type hexagonal structure

The hexagonal structure of RES crystallizing in the SG *P-3m1* is conventionally known as A-type. The unit cell is composed of a single formula unit with 2 cations occupying the symmetrically equivalent 1*a* site and the oxygen ions are distributed over the Wyckoff positions, 1*a* and 2*d*. Here, the cations are in 7 co-ordination polyhedral environment comprised of three different bond lengths. These are designated as RE-O1(2*d*), RE-O2(2*d*) and RE-O1(1*a*). This structure belongs to the large cation sized RES (La-Pm).

Apart from these three structure types there are two high temperature structures reported for the RES's, H-type and X-type. The former is a hexagonal structure with lattice parameters close to that of A-type but with a different SG, $P6_3/mmc$ while the later is a cubic structure with SG *Im-3m*.

1.3. Electronic structure of RES

RES's are typical *f* -electron systems for which the highly localized *f*-states play an important role in determining their chemical and physical properties[22]. Usually, the *f* electrons do not participate in bonding and electronic conduction but they are available for optical absorption and can establish strong magnetic order[23]. Typically, itinerant *spd* states and highly localized *f* states are present in such systems. The *f* electrons are assumed to be highly correlated and they do interact with the itinerant states. The difficulty in treating both localized and itinerant character of these electronic states on the same footwork is a major challenge to the current theoretical approaches, like in the density functional theory (DFT). The electronic band structure of RES has been investigated by several groups[22-25]. Irrespective of the polymorphic structure in which they belong, the band structure of a particular compound is shown to have similar characteristics[26]. The valence band is majorly populated with O-2*p* contribution, whereas

RE-5*d* contributes more to the conduction band. In general, the occupied *f* states fall below the O-2*p* conduction band whereas, the unoccupied ones fall in between the O-2*p* valence band and RE-5*d* conduction band. However, the energy of occupied and unoccupied *f* bands are different in different phases. Moreover, the band structure shows a noticeable peak splitting due to the difference in the local co-ordination and symmetry[26]. The features in the band structure of B-type monoclinic structure are found to be a mixture of those observed in C-type and A-type.

The investigations on the valence state of RES have shown that, trivalent ground state configuration is the most favourable valence state for majority of the RES[23, 24]. However, the degree of trivalency increases from Ce_2O_3 to Gd_2O_3, then decreases slightly at Tb_2O_3 to increase again through Dy_2O_3 to Ho_2O_3. Leaving the extra stability shown by the half filled *f* orbitals, the increasing tendency to form a trivalent state has a clear relation to the increasing localization of the *f* electrons with increase in atomic number[24]. This extra stability combined with the position of *f* bands in the electronic structure has shown to have a major role in deciding the band gap of the RES's. The experimentally determined band gap of all the RES were summarized and a detailed report is available in the literature[23, 25]. The band gap varies from 2.4 eV for Ce_2O_3 to 5.5 eV for La_2O_3 indicating a more or less insulating nature of all the RES. Minimum values were observed at the beginning (Ce and Tb) and at the end of the two halves (Eu and Yb) of the rare earth series. The reduction for Ce and Tb is attributed to the presence of *f* states in between the O-2*p* state and the RE-5*d* states whereas, a smaller energy gap between the valence and conduction band is responsible for the reduction for Eu_2O_3 and Yb_2O_3[25]. If the *f* band is present in the forbidden region, *f-d* gap will determine the band gap otherwise the position of O-2*p* state and the RE-5*d* states will determine the band gap [23, 25].

1.4. Stability of rare earth sesquioxide

The 14 elements from Lanthanum (Z=57) to Lutetium (Z=71) in the periodic table of elements are classified as rare earths or commonly Lanthanides. They have an electronic ground state configuration of the form [Xe] $4f^{n}5d^{1}6s^{2}$ where n stands for the number of *f* electrons. The primary member, Lanthanum is characterized by an empty 4*f* shell whereas, a fully occupied 4*f* shell is the characteristics of the end member, Lutetium. As the atomic number (Z) increases, more and more electrons will start occupying the localized 4*f* shell rather than the valence orbitals, 5*s* and 5*p*. As the f electron occupancy increases, the effective screening of nuclear potential reduces. This is due to the poor shielding power of the 4*f* orbitals. This effectively increases the coulomb attraction between the nucleus and the valence electrons resulting in a constant decrease of ionic radii of the lanthanides. This effect is the well known lanthanide contraction. The effect of cationic radii on the molar volume of the RES with different structure types were summarized by Zinkevich[19] and are reproduced in the Fig. 1.2a. It is clear that, molar volume follows a linear dependence on the cationic radius. As the *f* electron occupancy increases, A→B→C is the preferred structure type. Even though the cationic radius increases in the C→B→A sequence, the molar volume found to be decreasing in the same order[2]. Hence, a transition from C→B→A is expected under pressure. A volume reduction of ~8% and 2% is expected during the C→ B and B→ A phase transitions respectively.

Inorder to understand the dependance of the cationic radii on the structural stability, several studies were carried out on the solid solutions of RES's. The first comprehensive study on the phase relations between trivalent rare earth ion oxides, $(RE^{i}\text{-}RE^{ii})_2O_3$, systems were reported by Schneider[27]. Single phase, C, B or A, solid solutions have been observed in the whole range of compositions for those systems with similar structure and very small difference, (ΔRE), between RE^{i} and RE^{ii}, whereas those with significant difference in ΔRE are found to form di/triphasic regions with different compositions and depending on the parent strcucture of $RE^{i}_2O_3$ and $RE^{ii}_2O_3$. The $(RE^{i}-RE^{ii})_2O_3$ systems with still larger ΔRE were found to crystallize in $RE^{i}RE^{ii}O_3$ perovskite type structure. In a recent review by Zinkevich, the phase stability of some of these $(RE^{i}-RE^{ii})_2O_3$ systems with molar concentration and temperature were calculated using the solution approximation method and a comparison was made with the experimentaly obtained thermal analysis data[19]. At ambient conditions, diphasic regions of A+B and A+C have been predicted for the $(La-RE)_2O_3$ (RE= Sm, Gd, Dy and Ho) solid solutions whereas a pure B-phase or a C+B diphasic region was not obtained in any of the composition range studied. All the three polymorphic modifications have been predicted for $(Nd-Yb)_2O_3$ and $(Nd-Y)_2O_3$ systems in different molar concentration. The phase structure of $(Eu-La)_2O_3$ solid solutions are not investigated till date. Hence, a systematic study on this solid solutions will be benificial.

Fig. 1.2b represents the stability of all the RES at high temperature and ambient pressure, reproduced from reference[19]. The RES Lu_2O_3 exists only in the C-type structure up to melting point and Yb-Er found to have a stable H-type structure at elevated temperatures. The C-type structure of Ho_2O_3 shows a transition from $C \rightarrow B \rightarrow H$ whereas for Dy-Tb it further transforms to the X-type before the melting point. The medium cation sized RES, Gd-Sm, are the only compounds which shows all the five polymorphic structures. In this case, the transition take a path of $C \rightarrow B \rightarrow A \rightarrow H \rightarrow X$ with the increase in temperature. For the large cation sized RES, Nd-La, the A-type is the stable structure at ATP and they transform to H-type and further to X-type with increasing temperature. In all the observed transitions, the transition temperature is found to be increasing with decreasing cationic radii.

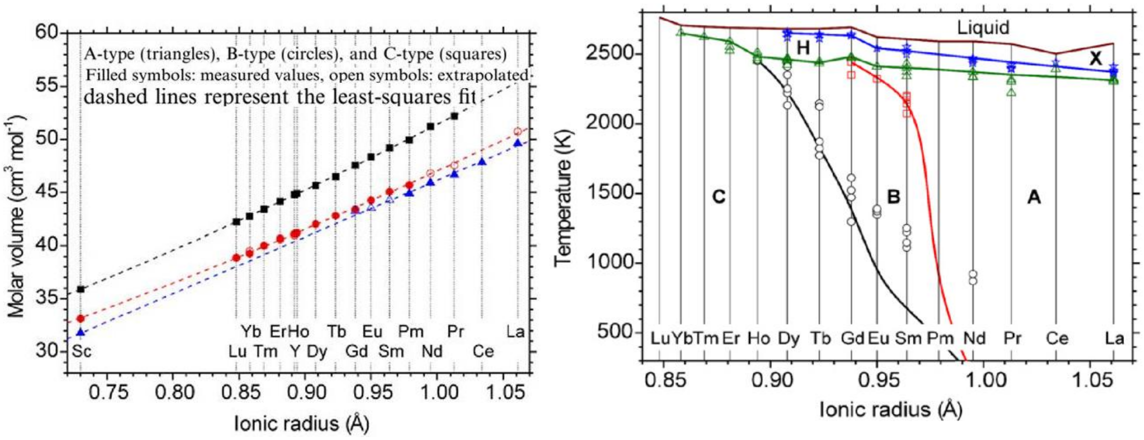

Fig. 1.2 a)The effect of cationic radii on the molar volume of RES with different structure types. Reproduced from reference[19]. b) The phase stability of all the RES at high temperature and ambient pressure. Reproduced from reference[19].

1.5. High pressure behavior of RES

Effect of pressure on the structural stability of RES was intensively studied by several group of researchers. As we have seen in the previous section the phase transition induced by temperature is dependent on the cationic radii of the RES. A similar dependence is observed when these materials are subjected to high pressure. The following subsections will describe how the behavior of the RES is different when they are subjected to extreme conditions of pressure.

1.5.1. Phase structure of large cation size RES

High pressure studies on the large cation sized RES are scarce. Reports on the high pressure study of RES show that, hexagonal is the extreme structure and they undergo no structural phase transition further[6, 8, 9]. Probably this could be the reason for drawing less attention towards the hexagonal structure of large cation sized RES. Even though pressure induced super lattice formation has been observed in the La_2O_3 at around 8 GPa, no such super lattice reflections have been observed in the case of isostructural Ce_2O_3 and Nd_2O_3[6-9]. A structural transition from hexagonal Nd_2O_3 to a distorted monoclinic structure has been proposed by Pandey et.al[7]. Nonetheless, it has not been confirmed. Recently, an anomalous lattice expansion in the 10.2-20.3 GPa pressure range has been reported for Nd_2O_3 [9]. The same has been confirmed using Raman spectroscopy, in which the A_{1g} and E_{1g} stretching modes are stated to have different compressibilities. Our own investigation on the high pressure hexagonal phase of Eu_2O_3 (section 4.3 of Chapter 4) and other work on Gd_2O_3 and Er: Gd_2O_3 has reported this anomaly prior to the one in Nd_2O_3 [10, 28]. In the majority of the available reports, the reason for the observed anomalous behavior in hexagonal structure of RES is associated with the isostructural electronic transition[9, 10, 29]. However, the electronic structure calculations on the A-type RES has not predicted any isostructural electronic transitions in the pressure regions where the anomaly is observed[8, 30, 31]. These reports indicate the necessity of addressing the anomalous high pressure behavior of the hexagonal RES in detail.

1.5.2. Phase structure of medium cation size RES

The medium cation sized RES can be found at ATP either in the C-type or the B-type structure depending on their thermal history. Pressure induced structural phase transition from C→B→A is expected due to the observed decreasing trend of molar volume in the same sequence[2]. However, the medium size RES do not obey this sequence and instead go through a direct C→A transition[3-5]. Such a pressure induced C→A transition in Eu_2O_3 has been observed at 5.2 GPa, without the presence of the intermediate monoclinic phase[4]. Similar transition is observed for Gd_2O_3 and Sm_2O_3 at a pressure of 7.2 GPa and 4.2 GPa respectively[5, 32]. The reason for the absence of intermediate phase in these medium rare earth sesquioxides is not fully understood and the preference of a particular structure type over the other is still under debate. A Report on the high pressure transitions of Gd_2O_3 revealed that the monoclinic phase of this intermediate RES is a high pressure (HP) and high temperature (HT) phase[5]. In support of this argument, the DFT calculations showed that, the monoclinic phase has the highest lattice energy and is associated with the HT phase and the transition from C→B cannot be obtained by pressure alone at low temperatures[5]. Studies on high pressure hexagonal phase of intermediate cation sized RES Gd_2O_3 and Er: Gd_2O_3 have shown that, there exist an anomalous lattice compression beyond a certain pressure region[10, 28]. The hexagonal *a* axis is shown to have an expansion in the pressure region 20.1-28.1 GPa in the case of Gd_2O_3 and it has resulted in a slight discontinuity of the unit cell volume compressibility. This observation was later confirmed in the parent hexagonal structure of Nd_2O_3[9]. The description of the mechanism of these structural phase transitions either from C→A or C→B→A is scarce or unknown. The structural correlation between B-type and A-type are described elsewhere in the literature[1, 33, 34]. Even though the hexagonal A-type structure is known to be a distorted form of the monoclinic B-type structure, a clear picture describing the possible distortions in these RES under pressure that could lead to the observed phase transitions is not considered in detail anywhere. The high pressure energy dispersive studies on B-type Eu_2O_3 revealed a phase transition from monoclinic to hexagonal (B→A) at 4.7 GPa, while in a luminescent spectroscopic study the same was reported at 4 GPa[35, 36]. In addition, in both these studies the behavior of high pressure hexagonal phase was given much less attention and a reinvestigation would give a better understanding. B→ A phase transition in Sm_2O_3 and Gd_2O_3 is also reported earlier. Sm_2O_3 found to transform at a pressure of 2.5-3.2 GPa, while it was 6.2 GPa for Gd_2O_3[5, 32, 37].

1.5.3. Phase structure of small cation size RES

Pressure induced C→B structural phase transition has been observed in the small cation sized RES of Dy, Ho, Er, Tm, Yb and Lu[2, 38-43]. Among them, a C→B→A transition is observed only for Dy_2O_3 and Ho_2O_3, probably due to the limited pressure range covered in those experiments. A transition pressures of 7.7 GPa, 8.9 GPa, 9.9 GPa, 7 GPa,13 GPa and 12.7 GPa have been reported for the C→B transition of Dy_2O_3, Ho_2O_3

, Er_2O_3, Tm_2O_3, Yb_2O_3 and Lu_2O_3 respectively[2, 38-43]. Discarding the lower transition pressure reported for Tm_2O_3, this clearly indicates that, the C→B transition pressure is increasing from Dy_2O_3 to Lu_2O_3. This is attributed to the nature of increasing covalent bond due to the increasing bond strength with decreasing cationic radii[24]. Looking at the general trend of cation size dependance on the transition pressure across the lanthanides, such a lower transition pressure of Tm_2O_3 is surprising. The transition pressure reported for the Tm_2O_3 (7 GPa) is much less compared to its neighbouring RESs Er_2O_3 and Yb_2O_3. [2]. Hence, a reinvestigation is necessary to remove the ambiguity in the transition pressure.

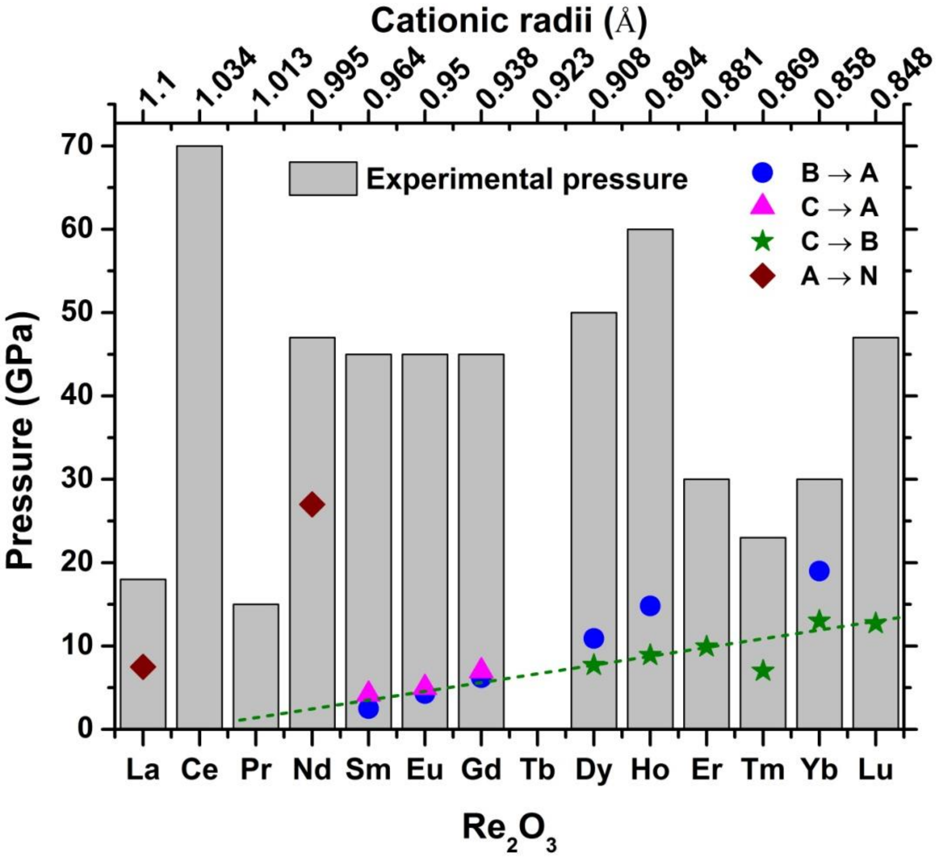

Fig. 1.3 The general phase diagram of RESs across the Lanthanides constructed using the literature in which the high pressure X-ray diffraction measurements are reported for the bulk powder samples. The data is taken from other measurements wherever X-ray diffraction data is not available.

A general phase diagram of RESs describing the C→B, C→A and C→B→A structural phase transitions along with the maximum experimental pressure achived in each of the RES is shown in the Fig. 1.3. It is clear that, the transition pressure is increasing with decreasing cationic radii. This is due to the increasing strength of covalent bonding with the decreasing cationic radii across the Lanthanides [2]. As a consequence of this increasing degree of covalency, an increase in bulk modulus is also observed across the lanthanides.

1.6. Objective of the thesis

Investigation of crystal structure and phase transitions of the RESs under high pressures forms the central theme of the present thesis. The objectives of the thesis are subdivided into the following three parts:

1. Investigate the structure of small (C-type), medium (B-type) and large (A-type) cation size rare earth sesquioxides under high pressures

In order to understand the phase behavior of simple RESs, the structural stability and phase transitions of representatives from C-type, B-type and A-type RES will be studied under pressure. To address the issue of ambiguity in the transition pressure, Tm_2O_3, representative of the C-type RES, is planned to study in the present thesis. Among the B-type RESs, the high pressure behaviors of Eu_2O_3 will be studied in detail as this information is not available anywhere in the literature. To compare the behavior of high pressure hexagonal structure of B-type Eu_2O_3, the A-type La_2O_3 will be investigated.

2. Investigate the effect of cationic radii and pressure on the solid solutions of RESs with similar structure and small difference in cationic radii

Solid solutions of Eu_2O_3 (medium cation size) and Ho_2O_3 (small cation size) crystallizing in the C-type structure and having a cationic radii difference of 0.056 Å are selected to address this objective. Eu_2O_3 shows a C→A structural phase transition whereas Ho_2O_3 shows a C→B→A transition. Hence solid solutions, $(Eu_{1-x}Ho_x)_2O_3$ $[0.0 \leq x \leq 1.0]$, of these two are desirable candidates to study the cation size dependence of phase structure at high pressures.

3. Investigate the effect of cationic radii and pressure on the solid solutions of RES with dissimilar structure and significant difference in cationic radii

Solid solutions of Eu_2O_3 (medium cation size), crystallizing in the C-type structure, and La_2O_3 (Large cation size), crystallizing in the A-type structure, with the difference of cationic radii 0.15 Å are opted to address this objective. Eu_2O_3, as mentioned earlier, shows a C→A structural phase transition whereas La_2O_3 shows no structural phase transition. Hence it is expected that, studies on the solid solutions, $(Eu_{1-x}La_x)_2O_3$ $[0.0 \leq x \leq 1.0]$, may provide substantial information about the cationic size dependence of different polymorphic structure types and their high pressure behavior.

These three objectives are addressed in the Chapters 4, 5 and 6 of the thesis.

Chapter 2

Experimental methods and analysis tools

2.1. Introduction

This chapter deals with the experimental and analysis methods adopted for the high pressure studies mentioned in the present thesis. The chapter is divided into three parts. The various experimental tools used for generating high pressures and their alignment, sample assembly and pressure calibration methods will be described in the first part. The second part describes the in-situ high pressure X-ray diffraction using the laboratory and synchrotron sources and Raman spectroscopy which were used as characterization techniques. The third part consists of the details regarding the Rietveld refinement, computational methods and the equation of states opted for the data analysis.

2.2. Diamond anvil cell (DAC) for the generation of high pressures

The static pressures on materials can be generated by either using a piston-cylinder apparatus or by an opposed anvil device. Tungsten carbide pistons against a cylinder made up of high strength steel was the major component of the piston cylinder apparatus. A maximum pressure of ~5 GPa can be achieved in this way[44]. The opposed anvils devices work on the principles of massive support. In this device, a large pressure is generated on a smaller area (working area) by applying a massive load at the larger area (loading face). Bridgman opposed anvil device and diamond anvil cell are the two major variants of this type. In Bridgman opposed anvil device two symmetrical assemblies of anvils are placed one above the other and an electrically powered hydraulic pump is used to apply load to the anvils[44]. Even though the upper pressure limit is ~10 GPa, a large sample size of the order of several millimeters can be studied in this type of cells.

Diamond anvil cell (DAC) is an excellent tool to generate the high pressure of the order of giga Pascals in the laboratory. In a typical DAC assembly, the sample is squeezed in between two opposing anvils, made up of diamonds, which are driven together by an external force. The first DAC was designed and fabricated in 1958 by two different groups of researchers simultaneously. One for high-pressure X-ray powder diffraction study by Jamieson, Lawson, and Nachtrieb[45] and the other was used for infra red spectroscopic studies of powdered calcite up to a pressure of 3 GPa[46]. Weir in 1960 redesigned his DAC in order to carry out the crystallographic studies of materials at high pressure[47]. Development of a metal foil gasket technique to confine liquids inside the DAC helped in collecting powder diffraction patterns in a hydrostatic environment for the samples[47]. With this, several organic and inert fluids could be used as pressure transmitting medium[48, 49]. Pressure in the cell was estimated either from equation of state data of NaCl or from the shift of R1 and R2 fluorescent lines of ruby crystal with pressure[47, 50]. Presently diamond anvil cell has established itself as a tool par excellent which could be used with several probes from microwave to gamma radiation[51].

Even though the basic principle behind the DAC is the same, various kinds of DACs have been designed and fabricated for a variety of probes used and pressure ranges. The variations in the DAC are mainly from the different ways in which the force is generated and the mechanism designed for anvil-alignment. Based on this, five types of DACs have been developed and are being used. NBS cell, Bassett cell, Mao-Bell cell, Syassen-Holzapfel cell, Merrill-Bassett cell are the five types of DACs[52]. Several simple, inexpensive and compact modified versions of DACs are now commercially available. Miniature Merrill–Bassett cell, four-post cryogenic cell, compact cylinder cell etc are some of them[48]. Membrane DAC in which the force on the piston is generated by pressurized helium, which pushes an annular membrane is a major variant among the new comers[53]. Among all these a Mao-Bell type DAC was designed and fabricated in our laboratory, IGCAR, which is used for the high pressure and high temperature experiments[54-56]

2.2.1. Principle of Mao-Bell type DAC

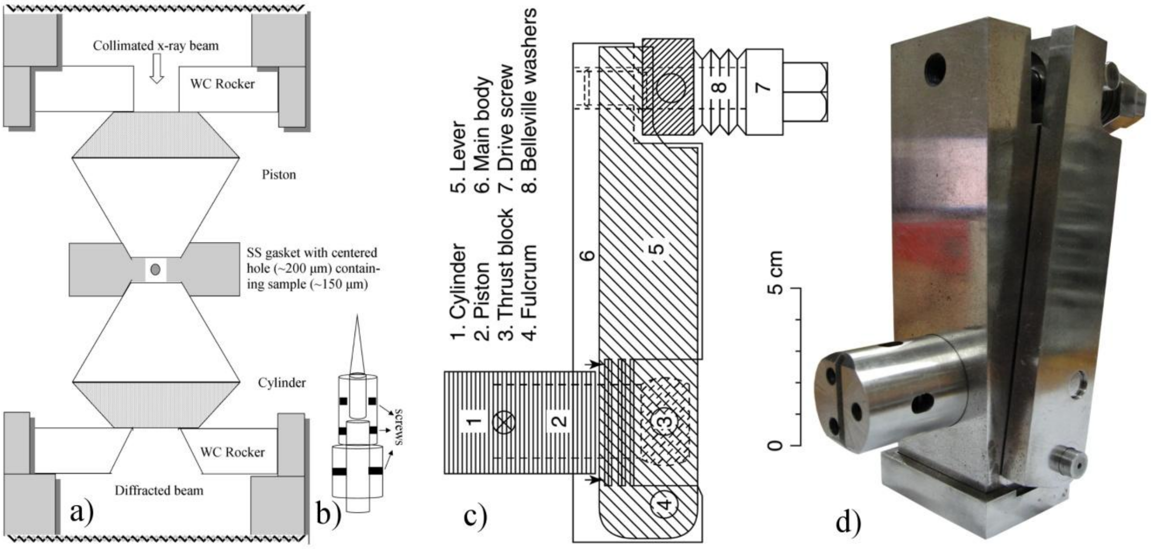

Fig. 2.1 Schematics representation of a) the opposed diamond anvils b) the X-ray collimator used in our laboratory c) a Mao-Bell type DAC with labeled parts and d) a photograph of home built (IGCAR) Mao-Bell type DAC used for the studies mentioned in the present thesis.

Mao-Bell type DAC works on the principle of massive support coupled with the lever arm mechanism to generate force. In order to achieve maximum pressure, the working area (diamond face or culet) of the anvils are reduced to micron size. The Fig. 2.1a-c shows the schematic of the opposed DAC assembly and the Mao-Bell type DAC. The photograph of the home built Mao-Bell type DAC used for the studies described in the present thesis is also shown in the Fig. 2.1d. Here, gem quality diamonds with a culet (diamond face) dimension of ~500 micron and a table dimension of 2 mm mimics the anvils. Diamonds of approximately equal dimensions were mounted on the hemispherical and cylindrical tungsten carbide rockers which can be fixed, by the screw mechanism provided, to the cylinder (1) and piston (2) respectively. The samples under investigation are confined to the culet area with the help of a gasket. The piston cylinder assembly is supported by a pressure cell holder (6) and is in touch with the thrust block (3) of the lever arm (5). The Belleville spring (8) loaded lever-arm (5) exerts force on the long cylinder-piston assembly by the mechanical driving of the screws (7). A maximum pressure of 100 GPa can be achieved in our home built DAC.

2.2.2. Alignment of Mao-Bell type DAC

In order to limit the anvil and gasket failure, three different alignments are necessary prior to the high pressure experiment using the Mao-Bell type DAC.

Axial alignment: In this procedure, diamonds are moved laterally to align them along the axis of the piston cylinder assembly. This is achieved by viewing through a microscope and rotating the piston inside the cylinder. Any axial deviation can be corrected using the 4 screws provided to hold the piston rocker. This alignment is necessary for the effective conversion of applied force to obtain a maximum pressure along the axial direction.

Lateral/ horizontal alignment: In this alignment, the diamonds on the piston and cylinder are mated together with their culets facing each other. Culet has to be laterally matched within 10% uncertainity. This is achieved by the translational movement of the rocker in the xy plane perpendicular to the axis of the piston using the same 4 piston screws. This is necessary to deliver maximum pressure and helps to avoid breakage of diamonds at high pressure. Fig. 2.2a shows the schematic of laterally misaligned culets.

Tilt alignment: A wedge in between the two diamond faces can cause breakage of diamond at HP due to the concentration of applied force to a small part of the culets in contact. The diamonds on the piston and cylinder are kept face to face and a source of white light is passed through the bottom of the cylinder. The culet face is observed visually through the piston and if the wedge is present an optical interference fringe (Newton’s rings) can be seen. This fringe is eliminated by tilt adjustments of the hemispherical cylinder rocker. Fig. 2.2b is a schematic representation of the formation of fringes due to the presence of wedge between the culets.

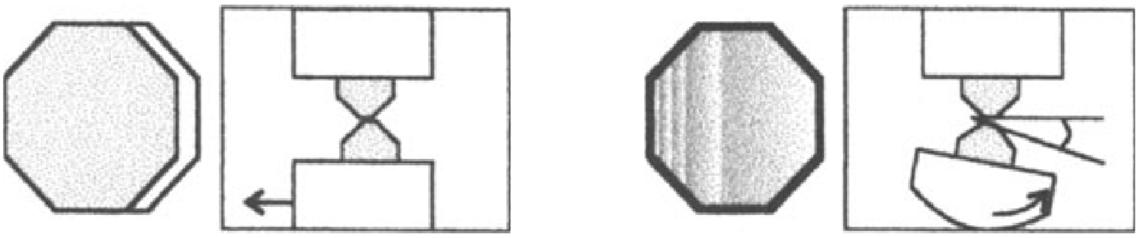

Fig. 2.2 a)The schematic representation of laterally misaligned culets. b) Schematic representation of the formation of fringes due to the presence of a wedge between the two diamond culets. Image taken from reference[57].

Collimating X-ray beam to the sample: The whole cell assembly with the collimator is kept on the sample stage and X-rays are passed through the diamond culet and ensured the passage using a GM counter. The piston cylinder assembly is made light-proof with electrical tape around the access ports. A photo graphic film of suitable dimension is placed in between the two culets. A slight pressure is applied to get the culet impression on the film. This assembly is exposed to X-ray for 10 sec. The exposed films are developed in dark room. The collimator control screws are aligned according to the photographic image. This procedure is repeated until the X-ray spot is at the centre of the culet. Optical images of the film in which the collimator is misaligned and aligned precisely with respect to the culet impression are shown in the Fig. 2.3.

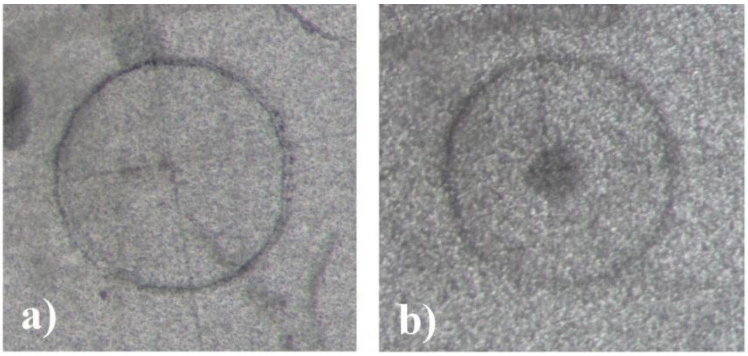

Fig. 2.3 Optical image of the developed photographic film after the X-ray exposure of 10 sec. a) Collimator is misaligned and the X-ray spot (dark spot) is just outside the culet region. b) X-ray spot at the centre of the culet showing a precisely aligned collimator.

2.2.3. Principles of Symmetric DAC

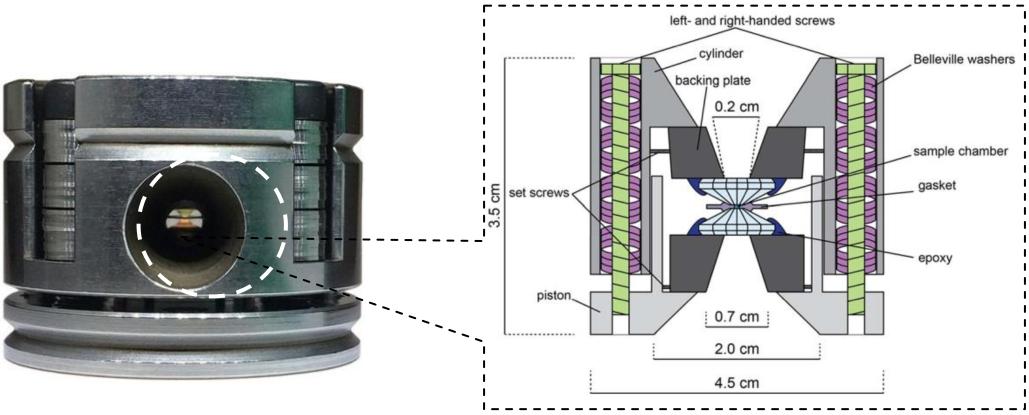

Fig. 2.4 The symmetric diamond anvil cell used for the high pressure Raman studies of Tm_2O_3 (left side) and the schematic representation of the same (right side)

The working principle of symmetric diamond anvil cell is more or less the same as that of the Mao-Bell type cell except for the fact that the load is transferred to the rockers via a set of four steel screws. High pressure Raman spectroscopy of the Tm_2O_3 sample described in the present thesis has been carried out using the symmetric DAC shown in the Fig. 2.4.

2.2.4. Pressure calibration

For the determination of pressure inside the DAC, generally two methods are employed.

i) Pressure marker method: In this method, the unit cell volume of a metal with a well-known relationship with pressure (equation of state, hence forth EOS), with the volume determined from X-ray-diffraction measurements is used to calibrate the pressure. Au, Ag, Pt metal powders are some of the commonly used pressure calibrants. The metal powder is loaded along with the sample and the Birch-Murnaghan EOS is employed to determine the pressure. As the sample and pressure markers are probed at the same region of the assembly, this method guarantees precise pressure estimation at the sample spot. More over the peak width variation of the calibrant with respect to the pressure is indicative of the nature of hydrostaticity.

ii) Ruby fluorescence: The energy level diagram of a ruby crystal (Al_2O_3:Cr^{3+}) is shown in Fig. 2.5a. The doping of Cr in Al_2O_3 induces crystal field splitting which creates metastable energy levels. When excited with suitable wave length (λ <600 nm), transition from metastable states to ground states takes place resulting in the two fluorescents peaks, R_1 and R_2 in the red region. It is observed that, R_1 and R_2 lines shift with pressure and the shifts have been calibrated with several pressure markers [58]. The observed line shift is fitted to a non linear equation:

$$P(\lambda) = \frac{A}{B}\left[\left({}^{\lambda}/_{\lambda_0}\right)^B - 1\right] \qquad (2.1)$$

where λ is the wavelength of the ruby R_1 line at pressure *P*, λ_0= 694.24 nm is the ambient-pressure value of R_1 at 298 K and A= 1904 and B= 5, 7.665 for non hydrostatic and quasi hydrostatic conditions respectively. The pressure dependent shift of R_1 and R_2 lines are shown in Fig. 2.5b.

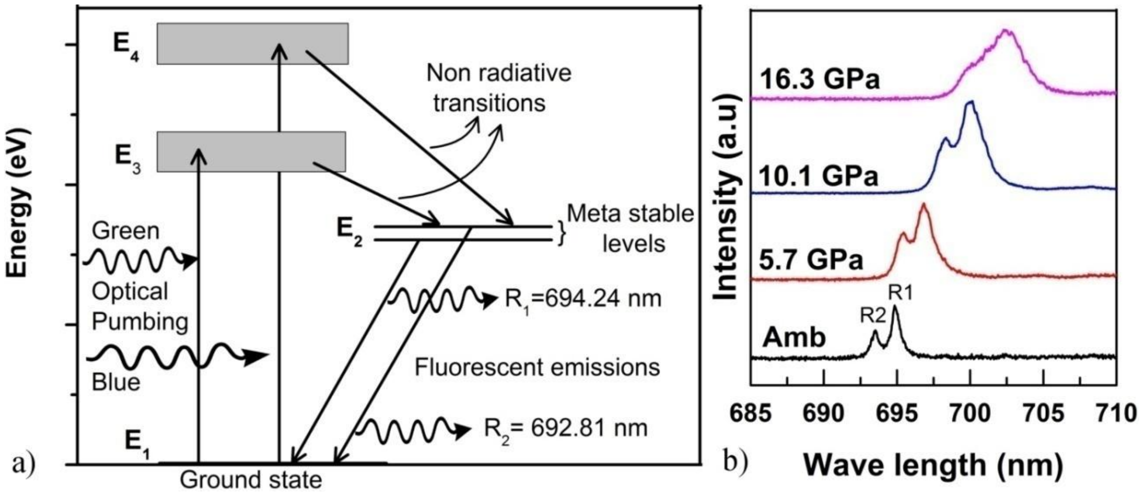

Fig. 2.5 a) Energy level diagram of Ruby. R_1 and R_2 correspond to the metastable to ground state fluorescent transitions. b) R_1 and R_2 lines at different pressures, showing the shift towards higher wave length with increasing pressure

For the work reported in the present thesis, either of these two methods was used to calibrate the pressure. EOS of Gold was used for Tm_2O_3 while, a combination of both

EOS of silver and ruby fluorescence was used in the case of $(Eu_{1-x}Ho_x)_2O_3$ solid solutions. In all other experiments, Ruby fluorescence method was employed to determine the pressure.

2.2.5. Pressure transmitting medium

Ensuring hydrostatic condition is necessary to probe the intrinsic properties of the materials under pressure. Such a condition is achieved by immersing the sample in pressure transmitting medium (PTM), typically a fluid with low yield strength and no shear stress is an ideal choice. In addition to this, PTM should be non reactive with the sample, pressure calibrant, gasket or the diamond. Also, a minimum background contribution is desirable. Since the melting point of fluids increases under pressure, the solidification of different fluids occurs at high pressures. Above this pressure the fluids will become inhomogeneous and generate shear stress across the sample volume. A systematic and comparative study of the hydrostatic limit of 11 commonly used PTM is reported elsewhere in the literature[59]. The work described in the present thesis used either methanol, ethanol, water in the ratio 16:3:1 or silicone oil as pressure transmitting medium which have a hydrostatic limit of 10.5 and 12 GPa respectively [59]. As the La_2O_3 is known to be highly hygroscopic, silicone oil has been preferred in the high pressure studies of $(Eu_{1-x}La_x)_2O_3$ solid solutions. In all other high pressure studies methanol ethanol water (16:3:1) has been used as the PTM.

2.2.6. Sample assembly inside the DAC

A metal foil gasket technique was used to load the sample in a typical high pressure study using DAC[47]. This has helped to confine the sample, reduce the pressure gradient across the sample and provide an additional support to the anvils. Stainless steel, Rhenium or Tungsten are the commonly used gasket materials. In the present work, a stainless steel (tungsten in the case of Tm_2O_3) gasket is preindented to 40-60 µm and it has been used as sample chamber in all the experiments. A schematic representation of the sample assembly inside the DAC is shown in Fig. 2.6. Sample with the pressure calibrant and pressure transmitting medium are loaded into the hole of diameter 200-250 μm drilled at the centre of the pre-indented gasket. After preheating the sample, a quick loading (within a span of 30 minutes) is ensured for the highly hygroscopic $(Eu_{1-x}La_x)_2O_3$ solid solutions.

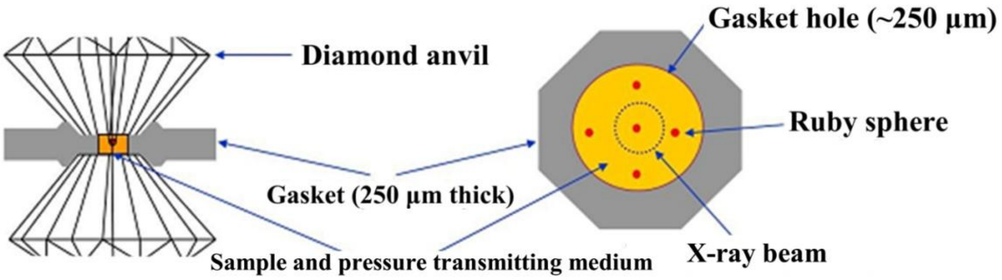

Fig. 2.6 Schematic representation of the sample assembly inside the diamond anvil cell

2.3. Characterization tools

The following subsections will discuss the basic concepts, practical methods and tools used to characterize the materials investigated in the present thesis.

2.3.1. X-ray diffraction

X-ray diffraction is the collection of intensities from the constructive interference of the scattered X-rays by the electron clouds of any crystalline material. The relationship between the direction of the incident and diffracted beam was first given by Laue in 1912 in a form of three simultaneous equations known as Laue equations. This gives the most general representation of a three dimensional diffraction pattern and can be used to describe the diffraction from a single crystal. One year later, In 1913 W. H. Bragg and his son W. L. Bragg came up with a law which established a relationship among the diffraction angle (θ), wave length (λ) and interplanar spacing (d). According to Bragg, the diffraction in periodic crystal can be visualized by using the notion of reflections of incident X-rays from a series of crystallographic planes. All planes with identical miller indices are parallel to each other and they are equally spaced with an interplanar distance d_{hkl}. Diffraction from a set of equally spaced planes is only possible for certain values of incident angle. A simple geometric analysis of Fig. 2.7 results in the well known Bragg's law as

$$2d_{hkl}\sin(\theta_{hkl}) = n\lambda \qquad (2.2)$$

Here, the integer n indicates the order of reflection. This law got wide attention in the field of X-ray powder diffraction studies.

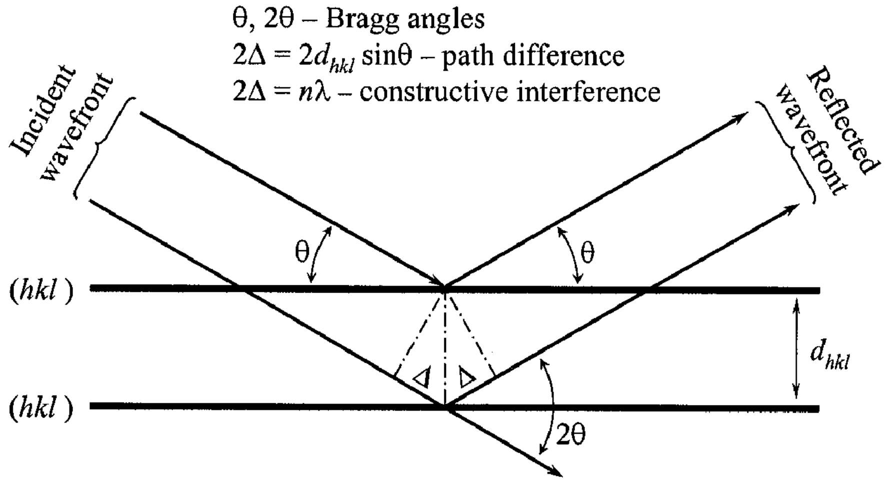

Fig. 2.7 Geometrical illustration of the reflection of X-rays from a set of crystallographic planes with spacing, d_{hkl} obeying Bragg's law

Practically, there are two ways of collecting the diffracted beam from a powder sample. As per the Bragg's law, θ and λ are the two parameters that can be varied in the data collection process. If λ is fixed (monochromatic X-ray) and θ is varied to fulfill the Bragg's condition then it is called angle dispersive X-ray diffraction (ADXRD), whereas if λ is varied (white light) and θ is fixed then it is known as energy dispersive X-ray diffraction (EDXRD). Also, depending on the position of the detector with respect to the sample and X-ray source, the diffracted beam can be collected in two geometries. When scattered intensity is collected after reflection from the sample it is known as Bragg-Brentano geometry and if it is collected after the transmission through the sample then it is known as Debye-Scherrer geometry.

The X-ray diffraction studies reported in the present thesis were carried out in the Debye-Scherrer geometry in ADXRD mode. In order to identify the structural stability and phase transitions in the investigated materials, either in house micro X-ray diffractometer or the Indus-2 synchrotron facility was used. In the case of $(Eu_{1-x}Ho_x)_2O_3$ solid solutions a combination of both has been employed to derive meaningful conclusions.

Laboratory based micro focusing X-ray diffractometer

High pressure X-ray diffraction studies of monoclinic Eu_2O_3 and $(Eu_{1-x}Ho_x)_2O_3$ [x =0.2, 0.6 and 0.8] solid solutions has been carried out using the in-house micro XRD setup[60] in angle dispersive mode. In this set up, a sealed tube (GENIX 3D supplied by M/s Xenocs, France) with Mo target was used as an X-ray source thereby providing X-rays of wave length of 0.711 Å. An X-ray spot size of 130x140 μm at a focal length of 25 cm from the source was achieved using the modern X-ray multi layer mirror optics. The X-ray flux delivered at the focal spot is $\sim 15.5\times10^6$ photons/sec at 50 kV and 1 mA. The system is equipped with a mar345 image plate area detector with a spatial resolution of 150x150 μm to collect the diffracted beam in transmission mode. Fit2D[61] software was used to convert the image plate data into one dimensional intensity versus 2θ patterns. In order to achieve better resolution of Bragg peaks, the image plate was kept on a guiding track allowing the back and forth movement. The DAC was mounted on a motorized stage which is capable of moving in the x-y-z and θ directions remotely. Fig. 2.8 shows the In house micro X-ray diffraction setup with labeled parts.

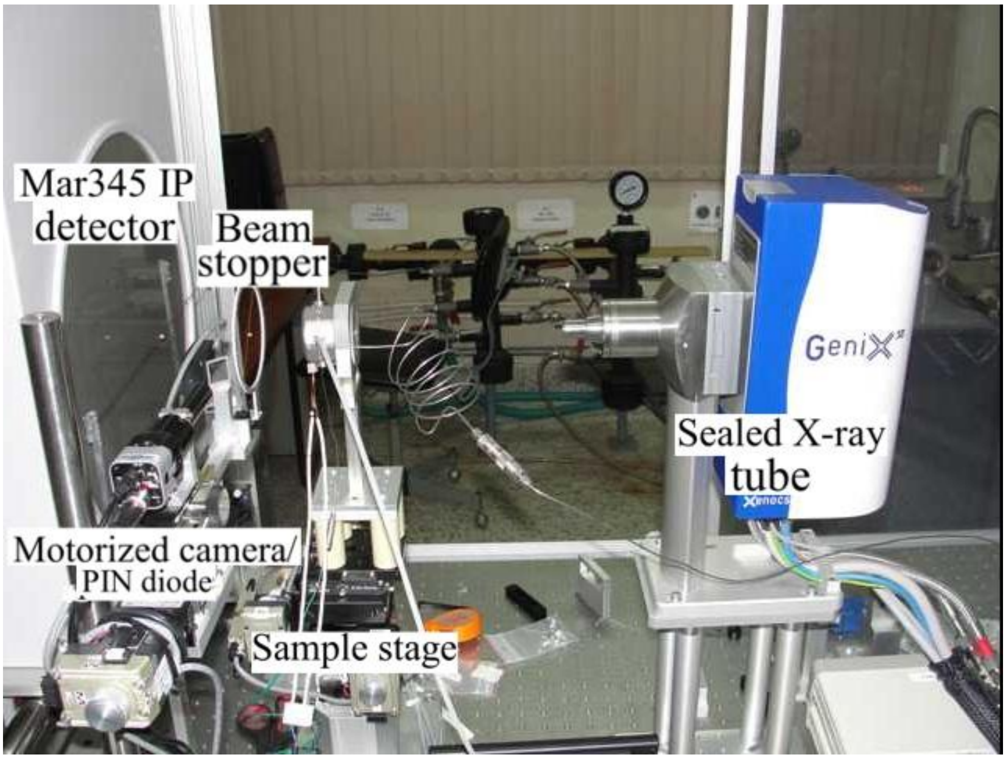

Fig. 2.8 In-house micro focusing X-ray diffractometer with a Helios membrane DAC mounted on the sample stage. The major parts are labeled. A motorized translational/ rotational sample stage is used to align the sample with the X-ray beam.

2.3.2. Synchrotron X-ray diffraction

A synchrotron is a particle accelerator where the electrons are accelerated to high energies through a circular orbit called storage ring. When these electrons, being charged particles, are accelerated or decelerated they emit Bremsstrahlung radiations[62, 63]. Dipole magnets are known to be the building blocks of a synchrotron which produces a vertical magnetic field in the gap between its poles. The electrons follow a circular orbital motion due to the centripetal acceleration generated by the magnetic Lorentz force of the dipole magnet. By setting up a series of such dipole magnets as shown in the Fig. 2.9a, it is possible to make the electrons revolve around a circular orbit of appropriate radius. The electrons are radially accelerated through a curved path inside the dipole magnet resulting in the emission of X-rays, whereas it follows a straight line path between the two dipole magnets. Initially high energy electrons need to be injected to the storage ring. This is done by a Linear accelerator (LINAC) which produces electrons with energies varying from several MeV to GeV range. Also a booster synchrotron is used in some of the synchrotron facilities which essentially used to achieve the desired input beam energy (in GeV) to inject into the storage ring from the output beam (in MeV) of LINAC. Typically the electrons are injected as discrete pulses so that they exist as bunches inside the storage ring. Because of this, the X-ray beam is not continuous in time but produced only as the bunch pass through the dipole magnet. A radio frequency (RF) generator/cavity is another major component of the synchrotron accelerator. This device is to synchronously feed energy to the bunch of electrons in the storage ring in order to compensate the loss of energy during their emission of radiation. Even then, this electron current eventually decays due to the collision between themselves and with other molecules present in the ring. Hence, it is necessary to refill the storage ring typically about every 24 hours. The main features of the synchrotron are: superior data statistics in a short experimental time due to the high intense radiation, high resolution data collection due to highly collimated beam, flexibility for polychromatic or monochromatic wave length and a horizontally polarized X-rays.

Part of the high pressure X-ray diffraction studies mentioned in the thesis were carried out at beam line 11 (BL-11) of Indus2 synchrotron facility at Raja Ramanna Centre for Advanced Technology (RRCAT), Indore, India. The circumference of the storage ring of Indus-2 is 172.47 m to which the electrons of energy 550 MeV (output from a booster synchrotron) are injected into the storage ring and the beam is accelerated to 2.5 GeV and is kept for several hours[64]. Indus-2 has 16 bending magnets, 72 quadrupole magnets and 32 sextupole magnets. There are eight 4.6 m long straight sections; two are utilized for RF cavities, one for beam injection and remaining five for insertion devices. A set of 4 RF cavities with an operating frequency of 505.812 MHz provides the required energy for beam acceleration from 550 MeV to 2.5 GeV as well as for compensating the energy lost due to emitted synchrotron radiation. Fig. 2.9b shows the different beam lines that are functional/ planned at Indus-2. As of now 13 beam lines for various purposes are commissioned and functioning well.

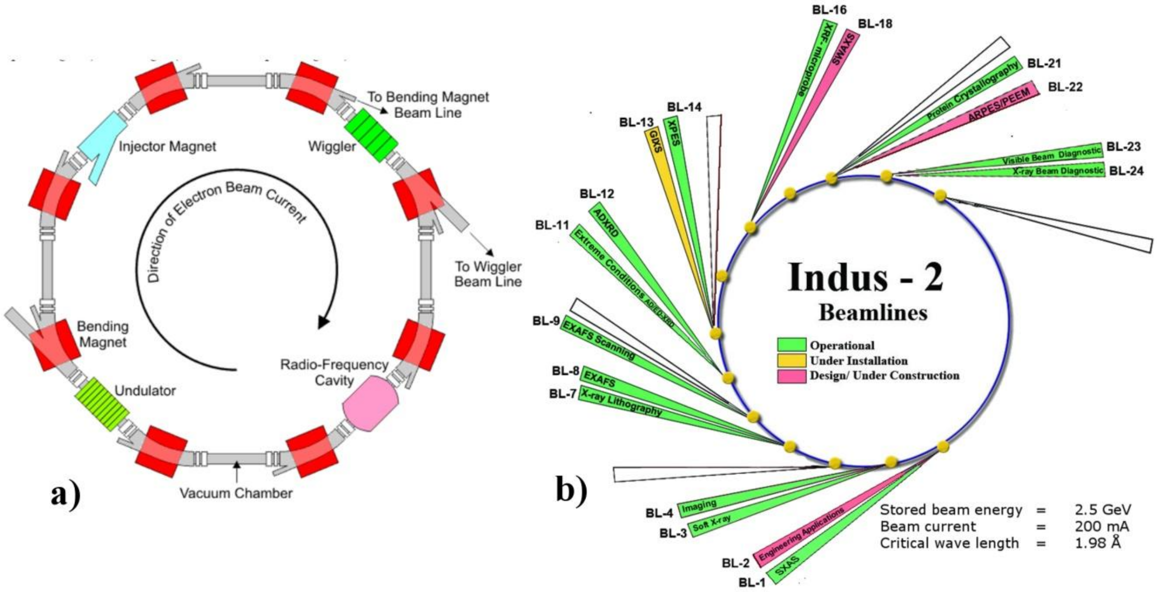

Fig. 2.9 a)A schematic representation of a typical synchrotron storage ring with labeled parts where some main components like bending magnets, insertion devices (undulator, wigglers) and the RF cavity are shown[65]. b) Schematic view of the beamlines of Indus 2 synchrotron facility at RRCAT, Indore, India [66]. The experiment reported in the present thesis has been carried out at extreme conditions AD/ED-XRD beamline (BL-11).

Angle dispersive high pressure X-ray diffraction experiments of all the samples except the monoclinic Eu_2O_3 described in the present thesis has been carried out at BL-11 of Indus-2 synchrotron facility. A Si(111) channel cut monochromater was used to tune the wavelength to 0.619 Å for Tm_2O_3, 0.620 Å for $(Eu_{1-x} Ho_x)_2O_3$ and 0.449 Å for $(Eu_{1-x} La_x)_2O_3$. In order to avoid diffraction peaks from the gasket material used for high pressure measurements, a Kirkpatrick-Baez (KB) mirror arrangement was used to focus the direct beam and x-y translational stages were used to align the sample into the X-ray beam. Standard Ce_2O_3/LaB_6 powder was used to calibrate the X-ray detector. A mar345 image plate detector was used to collect the diffracted data and was converted to intensity versus 2θ patterns using Fit2D[61].

2.3.3. SEM – EDS Measurements

The scanning electron microscope (SEM) is an instrument that creates magnified images which reveals microscopic-scale information on the size, shape, composition, crystallography, and other physical and chemical properties of a specimen [67]. The interaction of electron beam with the specimen produces backscattered electrons (BSEs) and secondary electrons (SEs). BSEs are produced by the elastic scattering of the incident beam by the electric field of the atoms in the sample whereas the electrons ejected from the atoms on the surface of the sample by the beam are known as the SEs. Though the SEs escape the specimen surface with very low kinetic energies in the range 0–50 eV, majority of them fall below 5 eV. The high energy electron beam is focused onto the desired sample area using the electromagnetic lenses and at each beam location, these outgoing electron signals are measured using one or more electron detectors. Typically, an Everhart-Thornley secondary electron detector (which is actually sensitive to both SEs and BSEs) and a “dedicated backscattered electron detector” that is insensitive to SEs are used. The signal measured at each individual raster scan location on the sample is digitized and recorded using a computer controlled software system. This is used to determine the gray level at the corresponding x-y location of a computer display screen, forming a single picture element (or pixel). Compositional microstructure, topography (shape), grain size and grain boundaries, crystal defects, and crystal deformation are some of the specimen properties that can be obtained from the SEM image.

Apart from the BSEs and SEs, the interaction of electron beam with the elements in the specimen produces characteristic X-rays (fingerprint of individual elements) over the continuous X-ray background (Bremsstrahlung radiation). A semi conductor energy dispersive (EDS) X-ray spectrometer, which can detect photons from a threshold of approximately 40 eV to 30 keV is used to collect this spectrum. The energy dispersive analysis of X-rays (EDAX) uses this X-ray spectrum to identify and quantify the specific elements present within the beam-excited interaction volume. The “k-ratio protocol” is used for the quantitative elemental analysis. The intensity of the characteristic X-ray peak for all the elements present in the specimen spectrum is compared against a suite of standards containing those same elements via a set of k-ratios given by $k = I_{specimen} / I_{standard}$ for each element in the specimen. However, the intensity of the emitted characteristic X-rays is influenced by the atomic-number (Z), absorption (A) and the fluorescence excitations (F). This is known as ZAF correction. Using the modern silicon drift detector EDS (SDD-EDS), uncertainity within 5% can be achieved in quantifying major and minor constituents.

In the present thesis, composition and morphological characterizations of $(Eu_{1-x}La_x)_2O_3$ has been carried out using the FEI make Helios NanoLab-600i dual beam field emission Scanning Electron Microscope (SEM) and an Apollo X Silicon Drift Detector attached to it. An acceleration voltage of 30 KV is used.

2.3.4. Raman spectroscopy

When materials are excited with radiations of suitable frequency, in addition to the incident frequency, there could be scattered radiations with frequency slightly above and below the incident frequency. This process of inelastic scattering is known as Raman effect. The scattered radiation with the same incident frequency is known as the Rayleigh line whereas the one with lower and higher frequency are known as the Stokes’ and anti-Stokes’ lines respectively (See Fig. 2.10). The classical theory of electromagnetic radiation was successful in describing the phenomena using the concept of molecular polarizability[68]. When a molecule is subjected to a static electric field, a charge separation occurs within the molecule. This charge separation causes an induced dipole moment to be set up in the molecule and the molecule is said to be polarized. The induced dipole moment can be represented as $P = \alpha E$, where E is the applied electric field and α is the polarizability of the molecule. The classical theory also leads to an important conclusion that, molecular vibrations which involve no change in polarizability can never be Raman active. Further using the classical harmonic oscillator approximation, the vibrational frequency can be expressed as:

$$\nu = \frac{1}{2\pi}\sqrt{\frac{K}{\mu}} \quad ; \quad \frac{1}{\mu} = \frac{1}{m_1} + \frac{1}{m_2} \qquad (2.3)$$

where K is the force constant of the bond, μ is the reduced mass of the two atoms (in case of diatomic molecule) with individual mass m_1 and m_2 constituting the bond. The force constant *(K)* which represents the bond strength and the type of vibration and the reduced mass *(μ)* are the two factors which determine the position of each Raman modes. Once these parameters are known the Raman modes can be calculated. Also, one can calculate the force constant of a bond from the Raman mode (provided the reduced mass is known). Subsequently, the quantum theory of radiation in which the radiation is treated as a stream of particles called photons with energy *hv*, has successfully explained the mechanism behind Raman scattering. The photons of energy *hv* undergo collisions with the molecule either elastically or inelastically. If the collision is elastic, a Rayleigh line is expected, whereas an inelastic collision results in the exchange of energy between the photon and the molecule. The molecule loses/gains energy in the discrete quanta of *hv* corresponding to the transitions between the allowed vibrational/ Rotational energy levels of a particular molecule. The selection rule for the transition between the allowed vibrational energy states is $\Delta n = \pm 1$ and the energy (corrected for anharmonicity) of each state is given as[68, 69]:

$$E_n = h\nu\left(n + \frac{1}{2}\right) - h\chi\nu\left(n + \frac{1}{2}\right)^2 \qquad (2.4)$$

where n is the integer, h is the Planck's constant, v is the vibrational frequency of the oscillator and χ is the magnitude of anharmonicity.

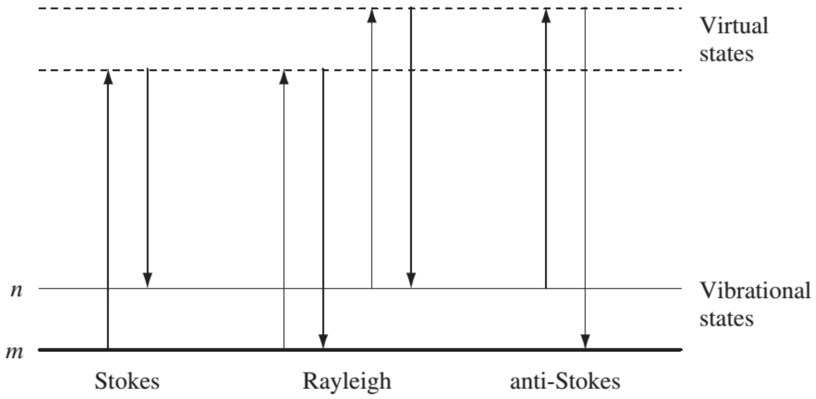

Fig. 2.10 Schematic of the Rayleigh and Raman scattering process. The lowest vibrational state m is shown at the bottom with states of increasing energy above it.

In practice, a laser light is focused on the sample and the intensity of the scattered light is collected as a function of wave length. In a typical Raman spectrum, the intensity is plotted as a function of the wavenumber, $\bar{\nu}$, given by $\bar{\nu} = 1/\lambda$, expressed in cm^{-1}. $\bar{\nu}$ is related to the difference in frequency between the scattered and the incident electromagnetic radiation. The position of a peak (mode/band) in the Raman spectrum is determined by the energy difference between the ground state and the vibrational excited states of a molecule. Hence, Raman spectroscopy is an invaluable analytical tool to explore the vibrational energy states (phonon modes) of molecules. Also, the number and positions of Raman modes present in a material varies with the symmetry of the molecule. Any change in the vibrational modes or the change in the symmetry of the molecules will reflect in the raising/ vanishing of new modes in the Raman spectrum. Typically, the structural phase transitions are accompanied by a change in the crystal symmetry. This is one of the major reasons behind the wide spread use of Raman spectroscopy in identifying and characterizing the materials at extreme conditions of temperature and pressure.

Renishaw micro-Raman spectrometer

Renishaw Invia micro-Raman spectrometer was used to record the Raman spectra of the samples studied in the present thesis. A schematic view of the spectrometer is shown in Fig. 2.11. An Ar^+ laser light of wavelength 514.5 nm has been used as an excitation source. The laser unit contains a delivery optics tube consisting of a filter wheel used to attenuate the laser power and an alignment mirror for aligning and sending the laser beam into system unit. This laser beam is directed via a set of mirror arrangement (M1) to the beam expander which shapes the laser beam and sends to a pin hole filter that turns the lazer into a spot of 10 µm from a line. After passing through the beam splitter, it hits the second mirror (M2) which directs the laser spot into the holographic notch filter unit and the laser light is reflected to a standard optical microscope. The microscope is used to focus the laser light into the sample with the help of an objective lens. The inelastically scattered radiations from the sample were collected by the same objective lens and transmitted back to the holographic notch filter through the same microscope. In order to ensure the maximum efficiency in transmission characteristics, the notch filter is aligned and placed at a specific position and tilt orientation (angle) with respect to the incident beam of a given laser light. Notch filter rejects the incident light, here 514.5 nm, with high efficiency and transmits the red shifted light with very high transmittance to the spectrometer. Also, a 514 nm edge filter is used to absorb all light up to 516 nm including the laser emission. It allows the detection of Raman spectrum by transmitting the light above 534 nm. Due to the very small transition width, below 1% of the laser wavelength, it collects information even at low Raman shifts. The spectrometer consists of a lens that focuses the scattered light into a slit and gets dispersed in a single monochromator using a holographic grating with 1800 grooves/mm. This spatially dispersed signal is focused on a charge coupled device (CCD) in which the charges stored are proportional to the intensity at a particular wavenumber and then the attached read out electronics will give the Raman intensity as a function of wavenumber. The spectrometer resolution for 1800 grooves/mm grating is 1.5 cm^{-1} per CCD pixel. The spectral range, accumulation time and laser power can be controlled using the data acquisition software, WiRE™ (Windows-based Raman Environment). A spectral range of 80-800 cm^{-1} has been selected for the studies mentioned in the present thesis. The Raman shift in wavenumber is calibrated using the 520.5 cm^{-1} Raman line from a Si single crystal.

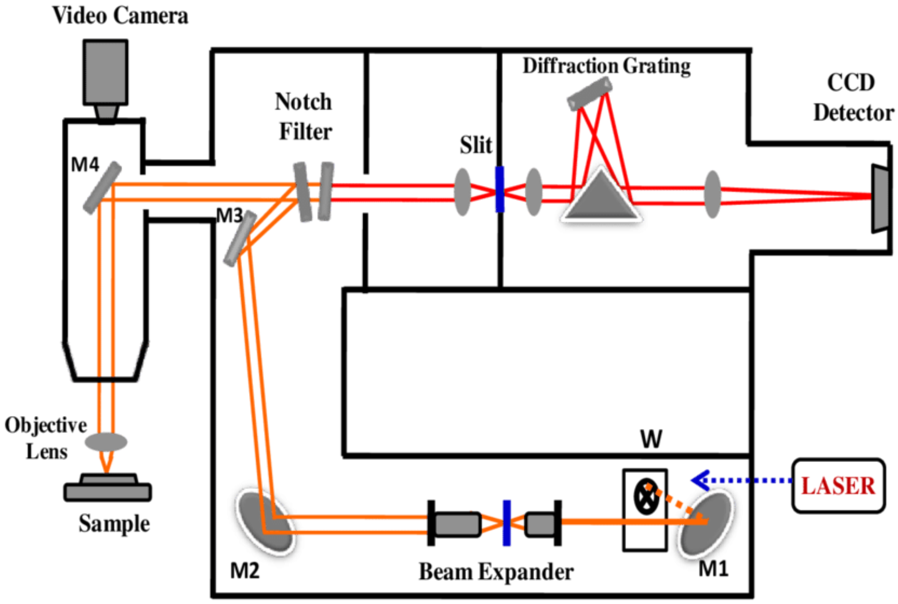

Fig. 2.11 The schematic block diagram of the Renishaw Invia micro-Raman spectrometer consisting of a laser unit, a system unit, an optical microscope, a monochromator and a CCD detector which is used in the present studies.

2.4. Analysis Methods

The following subsections will describe the methods of data analysis employed in the present thesis.

2.4.1. Rietveld structure refinement

Rietveld structure refinement of the X-ray diffraction data described in the present thesis has been carried out using the GSAS+EXPGUI software package[70, 71]. Rietveld refinement is a non linear least square method used to refine crystal structure parameters from a starting structure to obtain the best fit between the observed and the calculated profile intensities of a powder diffraction pattern[72]. The use of directly measured intensity points of the entire spectrum makes it less sensitive to the experimental error and hence its wide applicability among the powder diffraction community. Generally, a well resolved powder diffraction pattern with a good counting statistics, a starting structural model and a non linear least square code will be good enough to start the refinement. The quantity being minimized is the residue, $S_i= \sum w_i(y_{io}-y_{ic})^2$, where w_i is the statistical weight factor, y_{io} is the observed intensity at i^{th} position and y_{ic} is the calculated intensity at i^{th} position. The intensity at i^{th} 2θ position is calculated as $y_{ic}= S\sum F_k P_k L_k \Phi(2\theta_i-2\theta_k)A+y_b$, where S is the scale factor, k represents different hkl plane, F_k is the structure factor for the k plane, P_k, is the preferred orientation function, L_k, is the Lorentz-polarization factor, Φ is the peak profile function, A is the absorption correction factor and Y_b is the background function. For a particular plane, k, F_k is defined as $F_k= \sum N_j f_j exp[2\pi i(hx_j+ky_j+lz_j)]$ where, N_j is the site occupancy multiplier for the j^{th} atom site, f_j is the atomic form factor of the j^{th} atom and x_j, y_j, z_j are the fractional positions of the j^{th} atom. Depending on the instrument, any one of the available peak functions, Φ, can be used to model the observed peak profile. Gaussian, Lorentian and Pseudo-Voigt are some of the peak profile functions that are readily available with the Rietveld software. An elaborate discussion on the different peak shape functions, Geometrical correction factors and their implementation in the Rietveld software like GSAS are available elsewhere in the literature[70-72].

In the present thesis, the Rietveld structure refinement of the diffraction data has been carried out using the GSAS+EXPGUI software package. The instrument parameter file has been extracted from the refinement of standard powder diffraction pattern of LaB_6 or CeO_2 collected with the same conditions. The crystal structure of La_2O_3, Eu_2O_3, Tm_2O_3, and Ho_2O_3 are available in the literature and are considered as the starting model for the refinement[73]. In the case of solid solutions, refined structure of the x =0 composition was used as the starting model for x =0.1 composition and refined structure of x =0.1 was used as the starting model for x =0.2 and so on. X-ray peak profile is modeled with constant wave length profile function 3 employed in the GSAS package. 5 profile terms, including the crystallite size and strain broadening parameters are refined/ used to model the peak profile. A constrained refinement of site occupancy, atom position and thermal parameters has been performed individually at the final stage of the refinement of $(Eu_{1-x} Ho_x)_2O_3$ and $(Eu_{1-x} La_x)_2O_3$ solid solutions. These parameters are left invariant in the refinement of high pressure data of individual solid solutions. The details are presented in the forth coming chapters.

2.4.2. *Ab-initio* Density functional theory (DFT)

Density functional theory (DFT) is a computational method used to solve the complex Schrödinger equation of a many body system by implementing several logical approximations. As the quantum mechanical wave function contains all the information about the system, this has wide applications in investigating the structural, magnetic and electronic properties of materials. The success of the DFT formalism lies in solving the Schrödinger equation, which can be written as $\hat{H}\Psi = E\Psi$ where, $\hat{H}$ is the Hamiltonian operator, E is the ground state energy of the many body system and Ψ is the many body wave function. An explicit form of the time independent, non relativistic Hamiltonian where multiple electrons interact with multiple nuclei is written as:

$$\hat{H} = \hat{T}_N(\boldsymbol{R}) + \hat{T}_e(\boldsymbol{r}) + \hat{V}_{eN}(\boldsymbol{r},\boldsymbol{R}) + \hat{V}_{ee}(\boldsymbol{r}) + \hat{V}_{NN}(\boldsymbol{R}) \tag{2.5}$$

$$\hat{H} = -\hbar^2\sum_I \frac{\nabla_I^2}{2M_I} - \frac{\hbar^2}{2m}\sum_i \nabla_i^2 - \sum_{iI}\frac{Z_I e^2}{|\mathbf{r_i} - \mathbf{R_I}|} + \frac{e^2}{2}\sum_{i\neq j}\frac{1}{|\mathbf{r_i} - \mathbf{r_j}|} + \frac{e^2}{2}\sum_{i\neq j}\frac{Z_I Z_J}{|\mathbf{R_I} - \mathbf{R_J}|} \tag{2.6}$$

here, M_I and m are the mass of the Ith atomic nucleus and the electron respectively. $\mathbf{r} = \{r_1, r_2, r_3 \ldots r_n\}$ are the set of electronic co-ordinates and $\mathbf{R} = \{R_1, R_2, R_3 \ldots R_n\}$ are the set of nuclear co-ordinates. The first two terms in equation (2.6) represent the kinetic energy of nuclei and electrons respectively. The third term corresponds to the electron–nucleus Coulomb interaction whereas, the last two terms represent the Coulomb interaction between electron-electron and nucleus-nucleus. Here the $\hat{H}$ acts on the many particle wave functions which depends on both nucleus and electron co-ordinates. Unfortunately, the term $\hat{V}_{eN}(\boldsymbol{r},\boldsymbol{R})$ in the equation (2.5) prevents us from separating H into nuclear and electronic parts. This was not practical until the introduction of Born and Oppenheimer (B-O) approximation[74]. The B-O approximation rests on the fact that the nuclei are much more massive than the electrons, which allows one to conclude that the nuclei are nearly fixed with respect to electron motion. As a consequence of B-O approximation, the kinetic energy of the nuclei (first term in equation (2.6)) and the potential energy of nucleus-nucleus interaction (fifth term in equation (2.6)) are considered to be zero and constant function respectively. This simplified the many body problem into a many electron problem and the Hamiltonian is reduced to;

$$\hat{H} = \hat{T}_e + \hat{V}_{ee} + \hat{V}_{ext} \qquad ; \hat{V}_{ext} \equiv \hat{V}_{eN} \tag{2.7}$$

As the equation involves n electrons, Ψ is a function of 3N spatial co-ordinate and is represented as $\Psi(r_1, \ldots, r_n)$. Further, Ψ is approximated to the product of individual one electron wave functions, $\varphi_i(r)$, as $\Psi(r) = \varphi_1(r)\,\varphi_2(r) \ldots \ldots \varphi_n(r)$, Hartree product. The inability of finding Ψ(r) without simultaneously considering the individual electron wave functions associated with all the other electrons (due to the electron –electron interaction) makes the problem extremely complex. Hence, to further simplify the many electron problem, Thomas and Fermi proposed that, the individual electron wave functions can be used to model the electron density, $\rho(\boldsymbol{r})$, at a particular position in space[75, 76];

$$\rho(\mathbf{r}) = 2\sum_{i} \varphi_{\mathrm{i}}(\mathrm{r})^{*}\varphi_{\mathrm{i}}(\mathrm{r}) \tag{2.8}$$

here, the total electron density at **r** is the sum of the probability of finding the individual electrons with wave function $\varphi_{\mathrm{i}}(\mathrm{r})$ at that position, which is a function of only three coordinates. This model is the stepping stone to the modern DFT formalism. Due to the crude approximations used in this model in computing the total energy of electrons, it failed in many cases especially in predicting the bonding between atoms of solids and molecules[77].

The two fundamental mathematical theorem proved by Kohn and Hohenberg and the derivation of a set of equations by Kohn and Sham are the core of the modern density functional theory formalism[78, 79]. The theorem by Hohenberg and Kohn says: The ground-state energy of an electron gas is a unique functional of the electron density, $\rho(\mathbf{r})$, i.e. E= E[$\rho(\mathbf{r})$]. This gave an idea to solve the Schrodinger equation by finding a function of three spatial variables, $\rho(\mathbf{r})$, rather than a function of 3N variables. However, the theorem says nothing about the actual form of the functional. The second Hohenberg–Kohn theorem says: the $\rho(\mathbf{r})$ that minimizes the energy of the overall functional is the true electron density corresponding to the full solution of the Schrödinger equation. Once the ground state density is known, all other properties of the system can be calculated. Following the Hohenberg–Kohn theorem, the energy functional corresponding to the equation 2.8 can be written as

$$E[\rho] = T_e[\rho] + E_{ee}[\rho] + E_{ext}[\rho] \tag{2.9}$$

where, $T_e[\rho]$ is the kinetic energy of the interacting system, $E_{ee}[\rho]$ is the Coulomb repulsion energy and $E_{ext}[\rho]$ is the energy functional corresponding to the electron nucleus interaction. Still an accurate approximation of the kinetic energy as an explicit functional of the density was a difficult task. This limitation was overcome by mapping a system of n interacting electrons in an external potential to n non interacting electrons in an effective potential by Kohn and Sham[79]. According to the Kohn and Sham formalism, the energy functional and its corresponding Hamiltonian can be written as;

$$E[\rho] = T_0[\rho] + E_H[\rho] + E_{ext}[\rho] + E_{XC}[\rho] \tag{2.10}$$

$$\hat{H}_{KS} = \hat{T}_0 + \hat{V}_H(\mathbf{r}) + \hat{V}_{ext}(\mathbf{r}) + \hat{V}_{XC}(\mathbf{r}) \tag{2.11}$$

where, $\hat{T}_0$ is the kinetic energy operator of a single electron and $\hat{V}_{ext}(\mathbf{r})$ is the potential described by the interaction between an electron and the effective potential and $\hat{V}_H(\mathbf{r})$ is the Hartree potential operator representing the interaction potential of an electron with the electron cloud, formed by all the electrons in the system, and is expressed as $V_H(\mathbf{r}) = \frac{\delta E_H[\rho(\mathbf{r})]}{\delta\rho(\mathbf{r})} = \int \frac{\rho(\mathbf{r}')}{|\mathbf{r}-\mathbf{r}'|} d\mathbf{r}'$. The exchange-correlation potential $\hat{V}_{XC}(\mathbf{r})$ is introduced to accommodate all the quantum mechanical interaction effects like exchange and correlations present in the system and is defined as $V_{XC}(\mathbf{r}) = \frac{\delta E_{XC}[\rho(\mathbf{r})]}{\delta\rho(\mathbf{r})}$ .The difficulty of finding the true electron density is further simplified by using a set of Kohn–Sham equations of the form:

$$\left[-\frac{\hbar^2}{2m}\nabla^2 + V_{ext}(\boldsymbol{r}) + V_H(\boldsymbol{r}) + V_{XC}(\boldsymbol{r})\right]\varphi_i(\mathbf{r}) = \epsilon_i\varphi_i(\mathbf{r}) \tag{2.12}$$

where ϵ_i is the Kohn Sham eigenvalue. Now, to solve the Kohn– Sham equations, V_H needs to be defined, and to define the V_H $\rho(\mathbf{r})$ must be known. But to find the $\rho(\mathbf{r})$, $\varphi_i(\mathbf{r})$ must be known, and to know what these $\varphi_i(\mathbf{r})$ are, the Kohn–Sham equations must be solved. Hence, the problem loops around. The best way to solve this is by treating the problem in an iterative way as follows: i) define a trial electron density, $\rho(\mathbf{r})$. ii) Solve the Kohn–Sham equations using the $\rho(\mathbf{r})$ and find $\varphi_i(\mathbf{r})$. iii) Calculate the $\rho(\mathbf{r})$ from $\varphi_i(\mathbf{r})$ using $\rho_{KS}(\mathbf{r}) = 2\sum_i^n \varphi_i(\mathbf{r})^*\varphi_i(\mathbf{r})$. iv) compare the $\rho_{KS}(\mathbf{r})$, with $\rho(\mathbf{r})$. If the two densities are the same, then this is the ground-state electron density, if not, update the

$\rho(\mathbf{r})$ and repeat (from step ii)) the iteration until the two densities are comparable. Further to solve the Kohn–Sham equations $E_{XC}[\rho]$ should be specified and it is a painful task. The true form of the exchange–correlation functional can be derived exactly only in the case of a uniform electron gas [78]. Using this model, the exchange–correlation potential at each position can be represented as:

$$V_{XC}[\rho(\mathbf{r})] = V_{XC}^{electron\ \ gas}[\rho(\mathbf{r})] \quad (2.13)$$

This approximation uses only the local density to define the approximate exchange–correlation functional, so it is called the local density approximation (LDA)[80-82]. In real systems the electron density need not to vary uniformly in space. In such case the EXC calculated using LDA varies significantly from their actual values. The best known alternative is the generalized gradient approximation (GGA) which uses the local electron density and the local gradient in the electron density[83, 84]. Several GGA functional are defined and used based on the ways in which the information from the gradient of the electron density is included in the GGA functional. Two of the most widely used functional in calculations involving solids are the Perdew–Wang functional (PW91)[84] and the Perdew–Burke–Ernzerhof functional (PBE)[85].

A frozen core approximation is used to reduce the computational burden due to the core electrons which are tightly bound to the nuclei and do not participate in chemical bonding. Most of the physical properties of solids are dominated by the valence electron contributions than the core-electrons. Thus near the core region the strong electron-nuclei potential is replaced by a pseudo-potential, which will have the same behavior of total potential outside the core region[86]. There are different approaches to construct pseudo-potentials within the DFT codes. Projected Augmented Wave (PAW)[87] potential employed in Vienna *Ab initio* Simulation Package (VASP) has been used in the present study.

First principle calculations are performed using VASP with PAW pseudo-potentials[88]. The exchange correlation functional is computed using generalized gradient approximation (GGA) of Perdew–Burke–Ernzerhof (PBE)[85]. The kinetic energy cut-off and k-point mesh size are fixed by performing several convergence tests. A kinetic energy cut off 550 eV is used to truncate the size of plane wave basis set. Monkhorst–Pack [89] grid of size 7x7x7 and 5x17x9 are used to integrate over the Brillouin zone for cubic (80 atoms) and monoclinic (30 atoms) Tm_2O_3 systems respectively.

2.4.3. Equation of state for bulk modulus estimation

In order to obtain the bulk modulus, the pressure volume (P-V) data obtained from the high pressure X-ray diffraction measurements are fitted to the third order Birch-Murnaghan EOS:

$$P(V) = 3/2\,B_0\left[\left(\frac{V_0}{V}\right)^{(7/3)} - \left(\frac{V_0}{V}\right)^{(5/3)}\right]\left\{1 + 3/4(B_0{}' - 4)\left[\left(\frac{V_0}{V}\right)^{(2/3)} - 1\right]\right\} \tag{2.14}$$

here B_0, B_0', V_0 and V are the bulk modulus, derivative of bulk modulus, volume at ambient pressure and volume at pressure P respectively. In some cases the compressibility curve has been fitted with the modified Birch - Murnaghan equation of state [90, 91]:

$$P(V) = P_r + (3/2)B_0\left[\left(\frac{V_r}{V}\right)^{(7/3)} - \left(\frac{V_r}{V}\right)^{(5/3)}\right]\left\{1 + 3/4\,(B'_0 - 4)\left[\left(\frac{V_r}{V}\right)^{(2/3)} - 1\right]\right\} \tag{2.15}$$

here P_r and V_r represents the experimental pressure and volume at a fixed reference point and B_0 and B'_0 has their usual meaning.

2.5. Summary

As a summary to the present chapter of the thesis, the samples which have been investigated, the experiments performed on a given set of samples and the specific experimental conditions under which the experiments are performed has been tabulated in Table 2.1.

Table 2.1 The list of samples, characterization methods and the experimental conditions under which the experiment was performed for all the samples investigated in the present thesis.

Sample	**Experiments**	**$\lambda_{x\text{-ray}}$(Å)**	**Gasket**	**PTM**	**P_{calib}**
$(Eu_{1-x}Ho_x)_2O_3$ $[0.0 \leq x \leq 1]$	SXRD Raman	0.620 -	-	- -	- -
$(Eu_{1-x}Ho_x)_2O_3$ [x =0.0, 0.4, 0.5 and 1]	HP SXRD	0.620	Steel	MEW	Ag
$(Eu_{1-x}Ho_x)_2O_3$ [x =0.2, 0.6 and 0.8]	HP LXRD	0.711	Steel	MEW	Ruby
Eu_2O_3 (B-type)	HP LXRD	0.711	Steel	MEW	Ruby
Tm_2O_3 (C-type)	HP SXRD HP Raman DFT	0.619 - -	Tungsten Steel -	MEW MEW -	Au Ruby -
La_2O_3 (A-type)	HP SXRD	0.449	Steel	Silicone oil	Ruby
$(Eu_{1-x}La_x)_2O_3$ $[0.0 \leq x \leq 1]$	SXRD SEM-EDS HP SXRD	0.449 - 0.449	- - Steel	- - Silicone oil	- - Ruby

HP- High pressure	P_{calib}- Pressure calibrant
SXRD- Synchrotron XRD,	LXRD- Laboratory XRD
PTM- Pressure transmitting medium	Ag: Silver
MEW- Methanol ethanol water (16:3:1)	Au: Gold
DFT - Density Functional Theory	

Chapter 3

Development of a novel X-ray slit for DAC based XRD studies

3.1. Introduction

The collimation of X-ray beam with an external collimator as described in the section 2.2.2 is extremely involved because of the following reasons: i) the position of the X-ray beam through the external collimator with respect to the diamond culet is identified by placing an X-ray film in between the diamond culets and developing them after a short time exposure of approximately 5-10 sec. This has to be done for each fine adjustment that is made to the collimator head. Thus it consumes a great amount of time. ii) Due to the difference in take off angle for different instruments, the alignment is dependent on the particular X-ray diffractometer. iii) Once the lateral alignment of the anvils in the DAC is disturbed, the collimator has to be realigned. Because of the above mentioned reasons we have developed an internal collimation/slit assembly which overcomes all of the above mentioned limitations.

3.2. Making of rocker-slit assembly

A step by step process involved in the making of the X-ray slit to our DAC is shown in the Fig. 3.1. Usually a circular disc shaped tungsten carbide rocker with a well polished flat surface is used as massive support to the diamond anvils[92]. Such a polished rocker is shown in the Fig. 3.1a. There is a 1 mm diameter hole at the centre of the rocker which allows the X-rays to pass through. The surface of the rocker is pressed against a thin lead sheet (thickness ~0.3mm) so that the impression of the rocker hole is copied on to the lead sheet. This lead sheet is carefully trimmed for the copied portion by viewing through a calibrated Nikon SMZ 1000 stereomicroscope. The tiny piece of lead sheet, thus made, is pasted over the rocker hole. It is mandatory to ensure that the lead sheet pasted maintains the same level of height with the rocker surface. This has two advantages: i) It minimizes the beam divergence as much as possible ii) the slit will not get distorted while mounting the diamond or during high pressure experiments. Fig. 3.1b shows the rocker with the tiny lead sheet pasted over the 1 mm rocker hole. An adhesive can be applied to fix the lead sheet. It is advisable to apply the adhesive from the backside of the rocker hole, so that the surface level will not get disturbed. By viewing through the stereomicroscope, a hole of 100 μm diameter is drilled at the centre of the lead sheet using a tungsten carbide drill bit. The drilled hole has to be axially perpendicular to the rocker surface. Any deviation in this may cause reduction in the maximum X-ray intensity focused to the sample. Fig. 3.1c is the representation of such a rocker slit assembly.

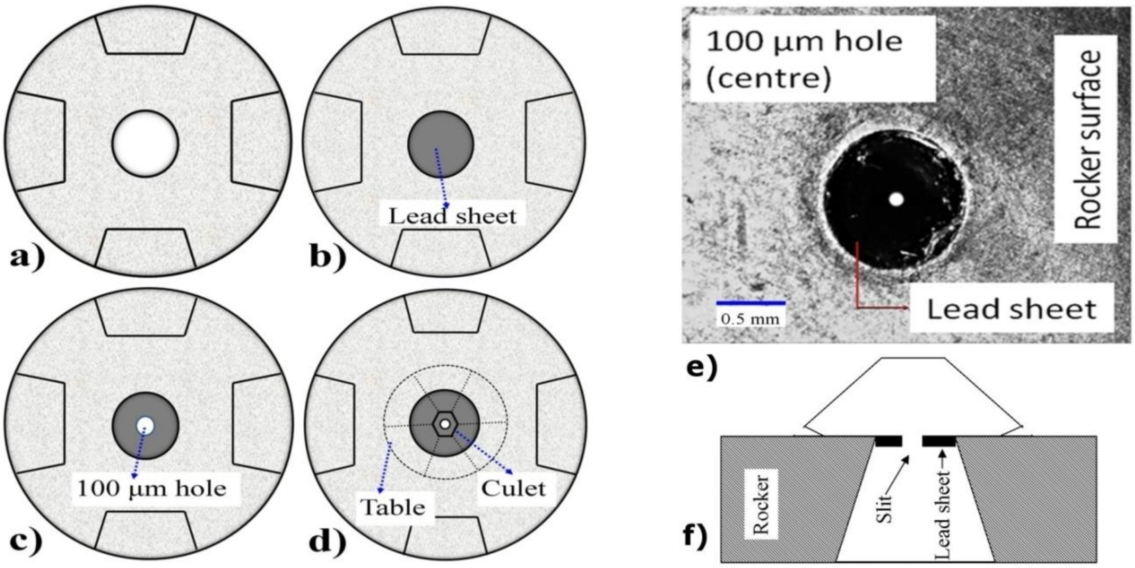

Fig. 3.1 Schematic representation of the various steps involved in making the rocker slit assembly. a) Tungsten carbide rocker with a well polished surface. b) Rocker showing a lead sheet stuck over the X-ray passage. c) Hand drilled 100 μm hole at the centre of the rocker hole. d) A diamond mounted on top of the rocker slit assembly. e) Photograph showing the rocker slit assembly before mounting the diamond and f) the schematic of the same after mounting the diamond.

3.3. Diamond mounting procedure

A diamond with culet size of ~450 μm is mounted on top of the rocker. As compared to the previous diamond mounting procedure[92], a different method was adopted here due to the invisibility of the full culet through the X-ray slit. In this method the diamond was made to sit on the rocker surface and the optical microscope was focused halfway between the slit and the diamond culet. The bottom light of the microscope was used to illuminate the slit so that both the slit and culet is visible. In order to position the slit at the centre with respect to the diamond culet, the diamond was gently slided over the rocker surface using a miniature tweezer. After centering, a small amount of adhesive is applied at the base of the diamond anvil without disturbing the position of the diamond with respect to the slit. Once it is dried the Epoxy resin (Stycast) is applied to affix the diamond on to the tungsten carbide anvil for carrying out high pressure experiments. Fig. 3.1d shows the schematic representation of the rocker slit assembly with a diamond mounted on top. The dotted lines, circle and the octagon are representatives of the diamond parts. The photographed image of the as prepared rocker slit assembly before mounting the diamond is shown in Fig. 3.1e and a schematic of the cross section of the same after mounting the diamond is shown in Fig. 3.1f.

3.4. Alignment of DAC

Alignment procedures followed here are slightly different from the usual ones[92]. The Prepared rocker slit assembly along with the mounted diamond is placed on the piston. The diamond anvils are laterally aligned by placing the DAC horizontally in a V-block and viewing through the microscope. Routinely Newton fringe method is employed to reduce the wedge between the anvils[92]. Since the slit size is less compared to the culet size, viewing the entire culet through the piston is not possible in this case. To overcome this, the two diamonds are kept in contact and the whole piston cylinder assembly is inverted in a way that the cylinder diamond rests on the piston diamond. This configuration will ensure the visibility of full culets through the cylinder diamond. Then the culets are illuminated by the bottom light and visual observations of the fringes are made through the stereo microscope. The adjustments of locking plate by the three socket-head-cap screws, in the bottom of the cylinder, will result in the complete removal of the fringes present.

3.5. Test results and conclusions

For testing and comparing purpose, X-ray diffraction patterns of Silver (Ag) powder has been collected inside the DAC using the in house micro XRD setup (GENIX 3D supplied by M/s Xenocs, France) with Mo target of wavelength 0.711Å and a mar345 IP detector. The diffraction patterns are shown in the Fig. 3.2. The peak shape parameters for the new and old collimation assembly are tabulated in Table 3.1.

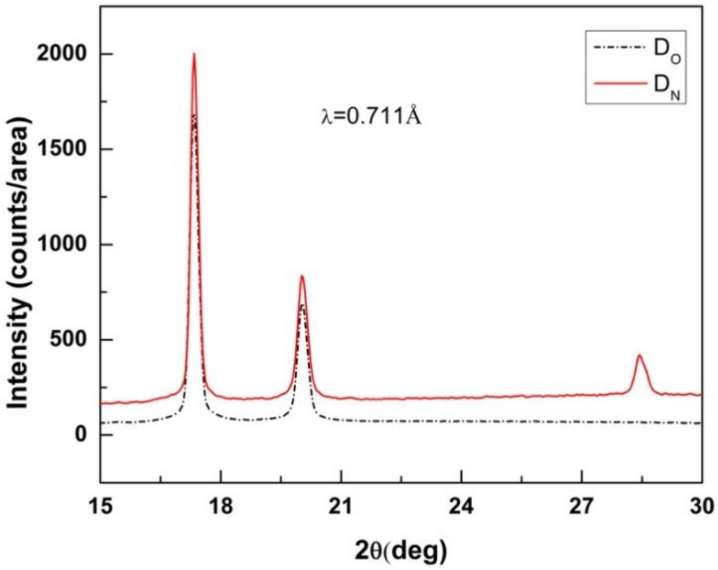

Fig. 3.2 XRD patterns of Silver powder collected for the new (D_N) and old collimation assembly (D_O). Data were collected for 30 minutes in both cases.

It is seen that the new collimation gives sharp peak with less FWHM in the lower 2θ range compared to the old collimation technique. This indicates the increase in resolution in this range. This could be due to the effective utilization of the incident beam profile by the new slit assembly. As the path length of the beam through collimator is reduced, aligning it to the maximum incident beam intensity is easier. Also the new collimation assembly is closer to the sample, which reduces the beam divergence.

Moreover with the new system, we are able to get comparatively better counts with increased peak height. The first high pressure experiment using this slit assembly has been carried out for the monoclinic Eu_2O_3 up to 25 GPa (described in the section 4.3), indicating the stability of the new slit assembly even at higher pressures.

Table 3.1 Comparison of peak shape parameters for both collimation assemblies. $D_{N/O}$ represents the new and old collimation assembly. Parameters are extracted from CMPR software[93].

	D_N/D_O	D_N/D_O	D_N/D_O
2θ	17.346	20.041	28.465
Peak height	1796.70/ 1616.81	631.92/ 600.46	203.87/ -
FWHM	0.217/ 0.241	0.280/ 0.279	0.321/ -
Peak Area	14178/ 14294	6831/ 6470	2460/ -

3.6. Summary

A novel X-ray slit for the diamond anvil cell based X-ray diffraction experiments, providing an improved resolution in the lower 2θ range, has been designed, developed and successfully tested for practical applications.

Chapter 4

High pressure phase transitions in Tm_2O_3, Eu_2O_3 and La_2O_3

4.1. Introduction

The present chapter is intended to understand the structural phase transitions exhibited by some of the simple RES under pressure. For this purpose a set of representative compounds from small, medium and large cation sized RES, Tm_2O_3, Eu_2O_3 and La_2O_3 respectively, have been selected for the present study. Contradicting the general trend observed for the RES of large cation size, X-ray diffraction studies on La_2O_3 carried out up to 18 GPa revealed the occurrence of a new phase transition at around 7.5 GPa[6]. This new phase is characterized from the observation of super lattice reflections. This phase transition from hexagonal structure to a novel high pressure phase is attributed to the anisotropic compressibility of the two RE-O bonds, which is aligned along the *c*-axis. This anisotropic change in bond length becomes periodic with respect to a unit cell doubled in length along the c-axis, leading to the formation of a super lattice. On the other hand high pressure energy dispersive studies on B-type Eu_2O_3 revealed a phase transition from monoclinic to hexagonal (B→A) at 4.7 GPa, while in a luminescent spectroscopic study the same was reported at 4 GPa[35, 36]. In addition, in both these studies the behaviour of the high pressure hexagonal phase was given much less attention and was unexplored. Tm_2O_3 belongs to the small cation sized RES. Hence a C→B→A transition is expected under the application of pressure. The studies on cubic Tm_2O_3 revealed that, the transition from cubic to monoclinic starts at around 7 GPa[2]. However, this transition pressure was much less compared to the expected transition pressure, of ~12 GPa, from the trend observed in the RES. Hence, a reinvestigation appeared to be necessary in the case of Tm_2O_3. In short, the present chapter will focus on the pressure effect on the following RES.

i. Tm_2O_3 (Small cation sized RES, in the cubic structure)

ii. Eu_2O_3 (Medium cation sized RES, in the monoclinic structure)

iii. La_2O_3 (Large cation sized RES, in the hexagonal structure)

4.2. High pressure structural phase transitions in Tm_2O_3

The following subsections will discuss the results of high pressure XRD, high pressure Raman and DFT calculations carried out on the RES Tm_2O_3.

4.2.1. X-ray diffraction studies

Cubic Tm_2O_3 (99.9% purity, Alfa Aesar) powder has been preheated at 800° C for 12 hours to remove the moisture, carbonates and hydroxides present. This powder was ground well and characterized by angle dispersive X-ray diffraction technique with λ=0.6194 Å at Indus-2 synchrotron facility, RRCAT, Indore, India. In order to confirm the phase purity, Rietveld structure refinement has been carried out to the as collected diffractogram. A shifted Chebyschev background function with 6 parameters has been used to model the back ground. The profile function 3 described in the GSAS manual was used to model the diffraction peak profile[94]. Initially, GU, GV, GW and LX profile parameters were varied independently and later they have been varied altogether during the refinement. Lattice parameter was refined to match the observed peak positions. Other structural parameters like atom positions and thermal parameters were refined independently by keeping all other refined parameters constant. Atom positions of Tm is refined first followed by the O. Thermal parameters are refined independently at the end. Fig. 4.1 shows the Rietveld fit to the diffraction data at ambient temperature and pressure. The observed diffraction peaks in the ambient structure could be indexed to the cubic phase (type- C) with space group (SG) *Ia-3*[95]. It is seen that, there is no trace amount of carbonates, hydroxides or any other impurity phase present in the pristine sample. The structural parameters of the pristine Tm_2O_3 are tabulated in the Table 4.1.

Table 4.1 Ambient structure parameters of Tm_2O_3 crystallizing in the *Ia-3* space group. The lattice parameter is 10.48766(5) Å.

Atom	x/a	y/b	z/c	Uiso
Tm_1	0.96804(5)	0.0	0.25	0.0112(1)
Tm_2	0.25	0.25	0.25	0.0112(1)
O	0.3905(6)	0.1517(6)	0.3805(7)	0.0112(1)

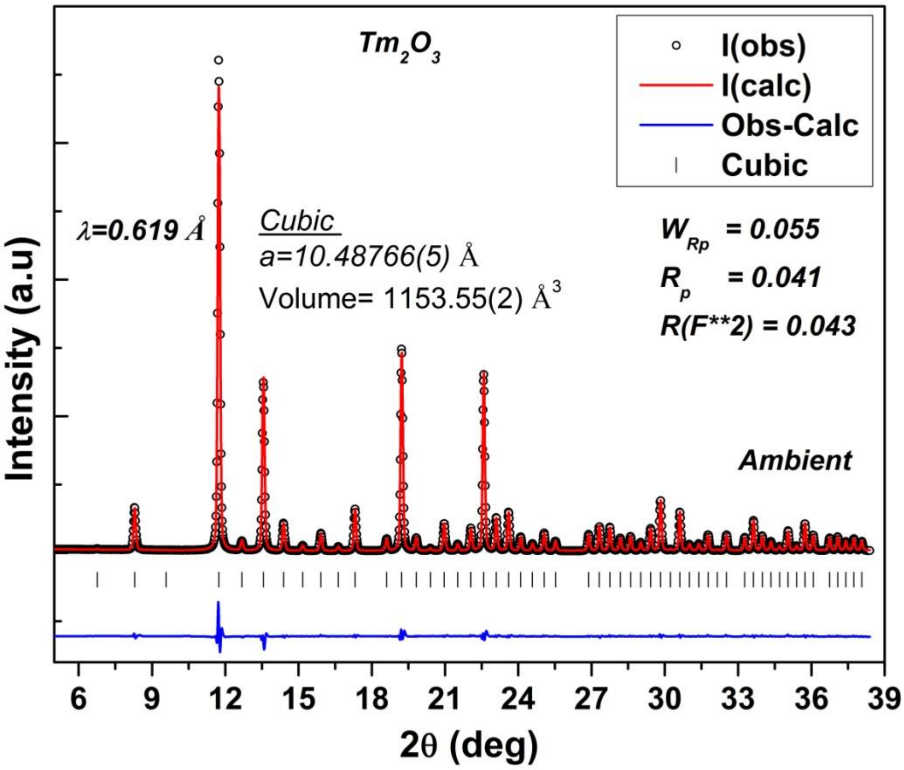

Fig. 4.1 Rietveld refined XRD pattern of pristine Tm_2O_3 at ambient condition

High pressure experiments were carried out in a Mao-Bell type diamond anvil cell (DAC) with a culet dimension of ~500μm. Angle dispersive X-ray diffraction pattern (ADXRD) of Tm_2O_3 recorded at various pressure steps at 298 K are shown in Fig. 4.2 a&b. Up to a pressure of 11.5 GPa, a shift in the diffraction peaks towards the higher 2θ angle along with the broadening of peaks has been observed, but no structural transition could be observed. At 11.5 GPa, origin of a new peak at 2θ = 13.51° near to the cubic *123* peak (see Fig. 4.2b) has been observed. As the pressure is further increased to 13.1 GPa, another new peak emerged at 2θ = 10.92° on the left of the high intense *222* cubic peak. These clearly indicate the onset of phase transition along with the parent cubic phase. At 17.1 GPa, several new reflections were observed and the high pressure phase was observed to be dominant over the parent cubic phase. The new high pressure phase could be indexed to the monoclinic phase (B-type) with space group *C2/m*[96]. The cubic phase coexisted with the high pressure monoclinic phase up to a pressure of 20.4 GPa and the transition is complete at 22 GPa. This monoclinic phase is found to be stable up to the highest pressure, 24.7 GPa. Upon releasing the pressure, there is no phase transition observed except a shift in the peak positions of the monoclinic phase towards the lower 2θ. The high pressure retrieved sample was observed to be of purely monoclinic in nature, signifying the irreversible nature of the C→B phase transition in cubic Tm_2O_3.

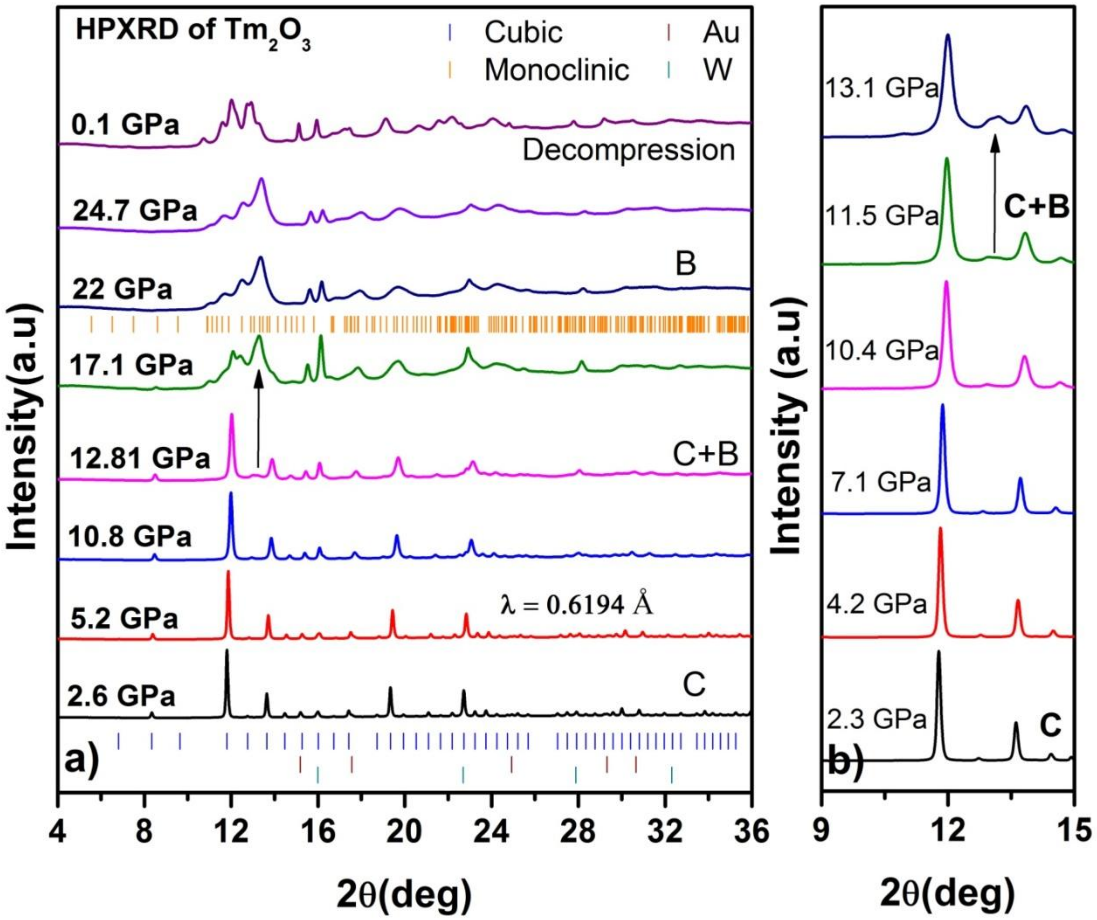

Fig. 4.2 a) ADXRD pattern of Tm_2O_3 collected at various pressure steps showing the C→B structural phase transition. The tick marks indicate the reflection positions for cubic, monoclinic, gold (marked as Au) and tungsten (W) gasket peaks. The pattern collected after decompressing to 0.1 GPa shows that the transition is irreversible. b) ADXRD pattern collected with lower pressure increments near the transition pressure showing the onset of structural phase transition at 11.5 GPa.

Pressure induced structural phase transition from cubic to monoclinic phase in Tm_2O_3 has been reported at a pressure of 7 GPa[2]. However, the present experiment yields a transition pressure which is far above the reported one. For the RES, Dy-Lu, crystallized in the cubic structure, the C→B transition pressure is found to be varying from 7.7-13.6 GPa and is found to be increasing with the decreasing cationic radii[38, 39, 41, 43, 97]. Hence, the transition pressure of Tm_2O_3 is expected to be somewhere around 12 GPa. Considering this fact, the present experimental transition pressure of 11.5 GPa might be the right transition pressure for cubic Tm_2O_3. In general, the C→B or B→C phase transitions in the RES are reconstructive type, involving a breakage of the existing bonds and formation of new bonds. Hence, these transitions require to overcome the huge energy barrier. In the compression process, the applied external pressure provides the required energy and favors the C→B transition. On the other hand, the decompression does not involve any additional supply of energy to the system, hence the observed C→B transition is irreversible in nature. To substantiate this, when the decompressed Gd_2O_3 was laser heated to approximately 550 °C, it has been observed that, a small fraction of cubic phase could be recovered[2].

In order to obtain the lattice parameters of the cubic and high pressure monoclinic phase at each pressure, Le Bail whole profile unit cell refinement has been carried out for all the high pressure X-ray diffraction patterns using the LHPM-Rietica software package[98]. The refinement was performed by considering the cubic (from Table 4.1) and monoclinic structure of Tm_2O_3 as the starting structural model[99]. Fig. 4.3 represents the Le Bail fit carried out for the X-ray diffraction data at 2.7 GPa and 22 GPa. The R factors are reasonable, indicating a good quality fit to the experimental data. The refined lattice parameters for the cubic and monoclinic structure at different pressure are tabulated in the Table 4.2. The refined data during the decompression cycle is also included.

Table 4.2 Lattice parameters of the cubic and monoclinic structure at different pressures. The parameters corresponding to the decompression cycle of the monoclinic phase also tabulated. The numbers in the parenthesis represents the error in the last decimal place.

Pressure (GPa)	**a (Å) Cubic**	**Pressure (GPa)**	**a (Å) Monoclinic**	**b (Å)**	**c (Å)**	**β (deg)**
0	10.48803(5)	17.1	12.990(2)	3.405	8.377(1)	98.17(1)
2.6	10.42886(5)	20.4	12.9309(8)	3.37	8.3512(1)	98.08(5)
3.3	10.41398(5)	22.0	12.914(1)	3.3669(5)	8.3513(1)	98.22(8)
3.9	10.40142(6)	24.7	12.852(1)	3.3558(8)	8.3327(6)	97.988(7)
5.2	10.37572(6)	**Pressure release**				
7.7	10.33074(8)	23.4	12.875(1)	3.3579(3)	8.3406(6)	98.030(8)
10.8	10.2711(1)	22.6	12.891(1)	3.3600(4)	8.3462(7)	98.075(8)
12.8	10.2410(1)	20.1	12.954(1)	3.3725(6)	8.3567(8)	98.257(9)
15.5	10.2138(3)	18.4	13.004(1)	3.3824(7)	8.371(1)	98.43(1)
		16.1	13.111(2)	3.415(1)	8.353(2)	98.92(1)
		13.5	13.186(2)	3.4168(8)	8.388(1)	99.16(1)
		10.9	13.221(2)	3.4242(9)	8.435(1)	99.18(1)
		5.9	13.438(3)	3.4375(8)	8.497(1)	99.89(2)
		3.3	13.558(3)	3.4462(6)	8.526(1)	100.10(1)
		0.1	13.686(2)	3.4598(5)	8.564(1)	100.24(1)

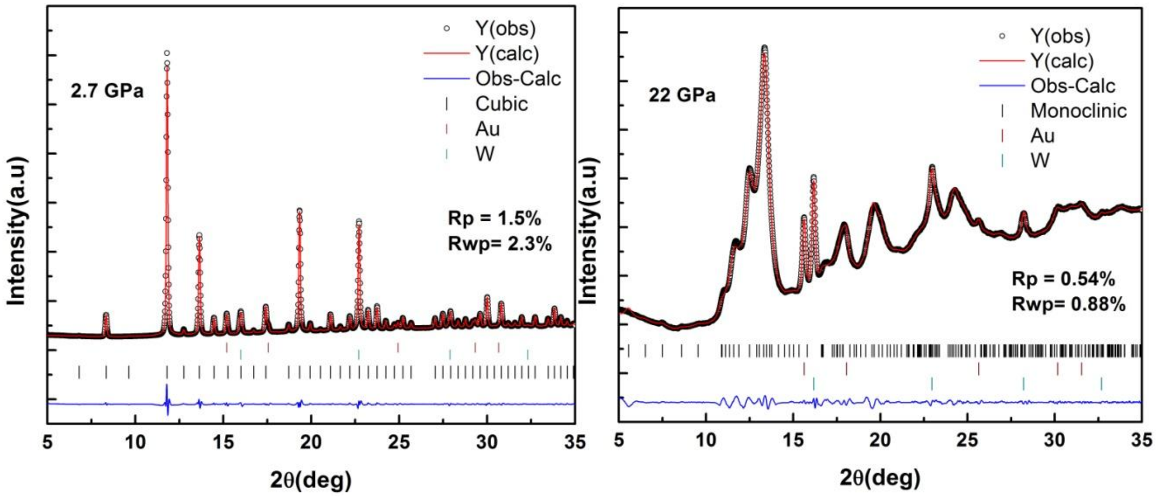

Fig. 4.3 Le Bail fitting of the high pressure X-ray diffraction data at 2.7 GPa and 22 GPa. Au and W stands for the reflections belonging to the Gold (pressure calibrant) and Tungsten (gasket material) respectively.

Unit cell compressibility and equation of states

The pressure dependence of the unit cell volume at room temperature is shown in Fig. 4.4. The change in volume of high pressure phase has been monitored both in compression and decompression cycle. It is seen that, the monoclinic phase follows the same path on compression and decompression cycle. There has been no hysteresis loss observed in the PV curve for the high pressure phase. The P-V data for both the phases are fitted to the Birch-Murnaghan EOS (see section 2.4.3) by considering only the data points collected during the compression cycle. Fitting the experimental data to the EOS results in the bulk moduli of 149(2) GPa with B_0' =4. 8(5) and 169(2) GPa with B_0' =4 (fixed) and the ambient volume of 72.10 Å^3 and 66.52 Å^3 for cubic and monoclinic phases respectively. The bulk modulus of both cubic and monoclinic phase is more or less the same, indicating the similar compressibility of both the structures. The phase transition from type-C cubic to type-B monoclinic structure is accompanied by a 7.25 % volume collapse at 11.5 GPa.

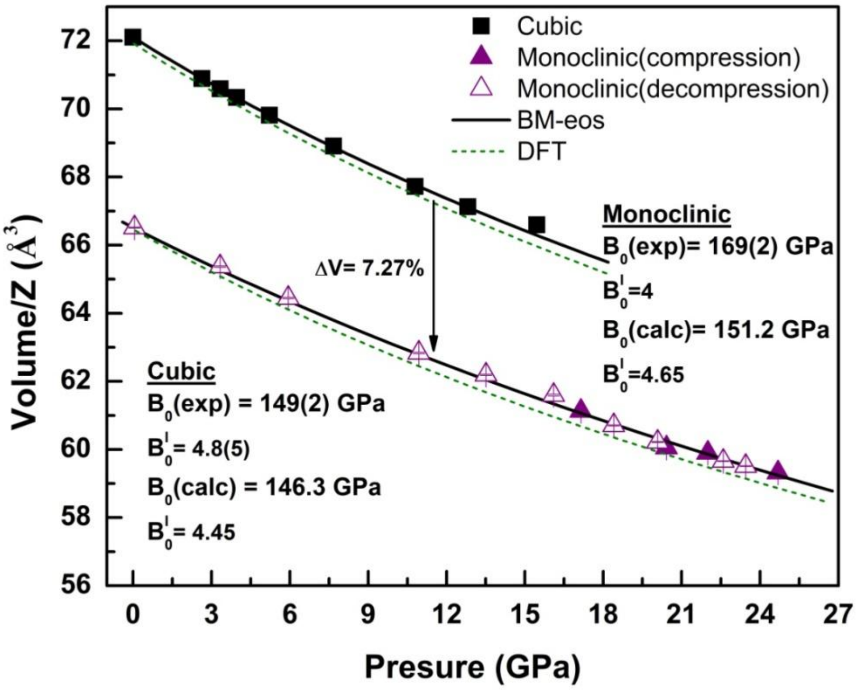

Fig. 4.4 The compressibility data of Tm_2O_3. The solid line represents the Birch-Murnaghan EOS to the P-V data, the open symbol represents the data collected during the reverse cycle and the dotted line is the compressibility curve calculated from the DFT.

A bulk modulus of 143 GPa for the cubic phase of Tm_2O_3 was calculated using the relation between Young's and shear modulus with the volume fraction porosity of cubic Tm_2O_3 whereas, the same has been reported to be 155(8) GPa from the angle dispersive X-ray diffraction measurements[2, 100]. Both the reported values are in good agreement with the present experimental result. To the best of our knowledge, there has been no report on the bulk modulus of high pressure monoclinic phase of Tm_2O_3 elsewhere in the literature. A bulk modulus of 151 GPa and 181 GPa has been reported for the cubic phase of nearby RES Er_2O_3 and Yb_2O_3[41, 42]. These values are close to the one obtained from the present experiment.

4.2.2. Raman spectroscopic studies

The vibrational frequencies of the material are determined by their phonon modes which in turn are related to their crystal structre. In order to support the observed phase transition from X-ray diffraction measurement, high pressure Raman spectroscopic study has been carried out on Tm_2O_3. The spectra collected for the parent cubic Tm_2O_3 sample at ambient temperature and pressure is shown in the Fig. 4.5a. The spectra show a good agreement with the previously available reports[101-103]. Factor group analysis for RE_2O_3 compounds with SG *Ia-3* predicted a total of 22 Raman active modes, $4A_g+4E_g+14T_g$ [104]. However, only 10 Raman modes could be observed, possibly due to the accidental degeneracy or insufficient intensity due to the small polarizability change of some of the reflections. The high pressure Raman data collected at various pressure steps are shown in the Fig. 4.6. 7 out of the 22 Raman modes are identified for the cubic structure. Rest of the low intense modes which were observed in the ambient spectrum has not been observed when the sample is loaded inside the DAC. This could be due to the absorption of the scattered signal by the DAC. Apart from a systematic shift towards the high frequency region and the broadening in the observed modes, there are no changes observed in the spectrum upto 12.2 GPa. This indicates that the cubic structure is stable up to this pressure.

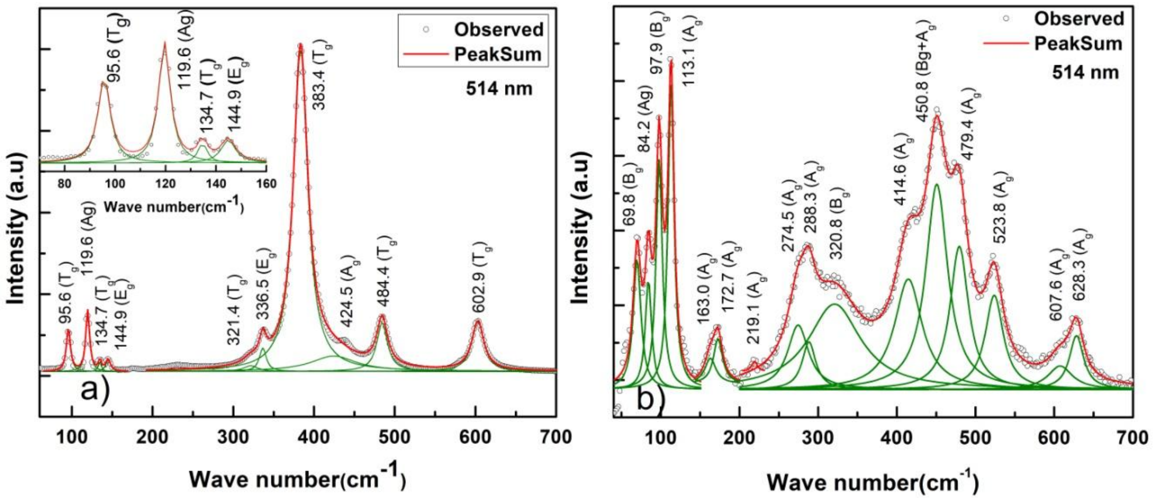

Fig. 4.5 Raman spectra of a) pristine cubic Tm_2O_3 b) high pressure retrieved monoclinic Tm_2O_3. 10 Raman modes for cubic and 16 Raman modes for monoclinic structure are identified and modes has been assigned based on the literature[103]. Solid green lines represent the individual peaks fitted using the Lorentian peak profile and the solid red line is the sum of all those individual peaks.

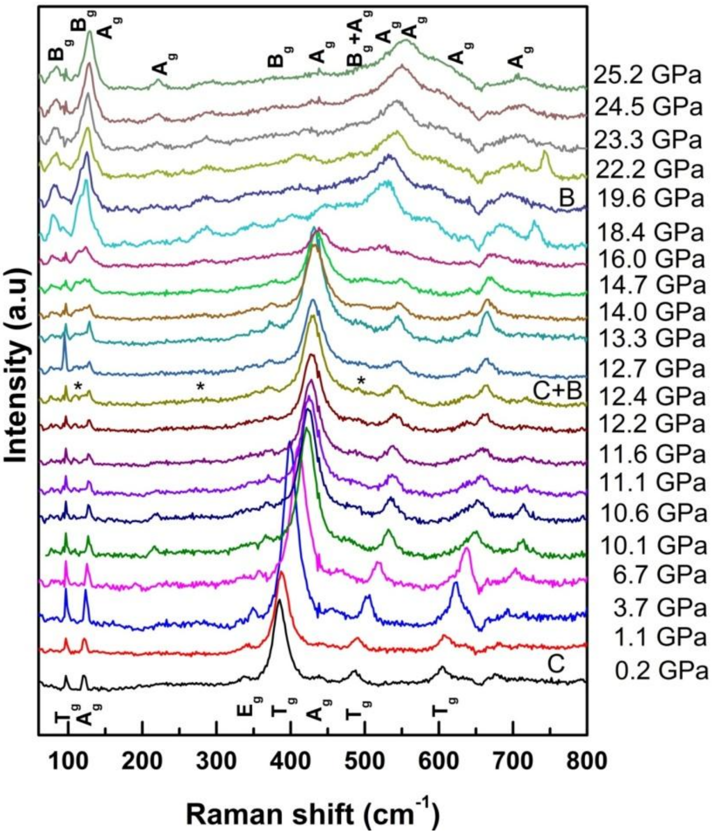

Fig. 4.6 Raman spectra collected at various pressure steps. The * marks indicates the onset of phase transition to the monoclinic phase, represented by the origin of the strong B_g mode.

At 12.4 GPa, the origin of a new mode (indicated by * in Fig. 4.6) at 119.7 cm^{-1} clearly indicates the onset of phase transition in this RES. In addition to the enhancement of intensity of this mode, several other new modes appeared and became predominant at 16 GPa. The intensity of the modes belonging to the parent cubic structure started diminishing at this pressure and the modes were completely absent at 18.4 GPa, indicating the completeness of phase transition. To the best of our knowledge, a Raman spectra of monoclinic Tm_2O_3 is not available elsewhere in the literature. Hence, the mode assignment of the new high pressure phase has been carried out using the existing report on the isostructural Er_2O_3 and Lu_2O_3[103]. The strongest mode of the high pressure phase below 300 cm^{-1} is assigned to the Ag mode. Above 18.4 GPa, no additional modes are observed and no other appreciable change is identified in the Raman spectra till the highest experimental pressure, 25.2 GPa, indicating the stability of monoclinic phase up to this pressure. This is consistent with our high pressure X-ray diffraction measurements. On decompression, the mode frequencies belonging to the monoclinic structure started shifting towards the low frequency region. Apart from the modes belonging to the monoclinic structure, there were no new modes observed during the decompression, indicating the irreversible nature of the phase transition as confirmed by the high pressure X-ray diffraction. Fig. 4.5b shows the Raman spectrum collected from the high pressure retrieved sample. 16 out of the 21 modes has been identified for the monoclinic structure and the mode assignment has been carried out by comparing with the available report on Er_2O_3 and Lu_2O_3[103]. To the best of our knowledge, this is the first report on the Raman spectra of monoclinic Tm_2O_3. The Raman studies show a good agreement with the XRD measurements which also confirm the C→B structural phase transition in the cubic Tm_2O_3.

The type-B monoclinic structure of RES belongs to the centro-symmetric space group *C2/m*, with 6 formula units in a single unit cell. In Tm_2O_3, Tm occupies 3 different 4i Wyckoff positions giving a 7 fold co-ordination environment with the oxygen atoms. The oxygen atoms occupy 5 different Wyckoff positions[19]. The primitive cell of type-B RES contains 15 atoms and hence 42 normal modes are associated with its vibration. From the factor group analysis, 42 normal modes, 14Ag+7Bg+7Au+14Bu, have been calculated for the type-B RES[33, 103, 105]. Out of this 21 (14Ag+7Bg) modes are Raman active. Recent lattice dynamics calculations of cubic Sc_2O_3 single crystal has concluded that all low frequency modes (below 300 cm^{-1}) predominantly arise from the vibrations of rare earth cations and the one above this originate from almost pure oxygen vibrations[102]. Hence, the observed mode frequencies are divided into two regions, above and below 300 cm^{-1}. The pressure dependence of all these modes are shown in the Fig. 4.7a&b. It is evident that the low frequency modes are hardly affected by the increse in pressure, whereas the modes above 300 cm^{-1} shift towards high frequency region indicating the hardening of these modes. In the case of type-B Sm_2O_3, Eu_2O_3 and Gd_2O_3 it has been shown that, the modes above 240 cm^{-1} involve the RE-O stretching vibrations[33]. As the stretching vibrations are more sensitive to the variations in the force constant, the compression of the RE-O bonds leads to an increase in the force constant and hence an increase in the mode frequency in this region. Fig. 4.8 a&b represent the pressure dependance of the mode frequencies of the high pressure monoclinic phase derived from the decompression cycle. Shift of the modes towards the low frequency region indicates the softening of these modes upon releasing the pressure. The effect of compression on the modes can best be represented by a dimensionless quantity called the Gruneisen parameter, represented by $\gamma_i = (B_0/\omega_0)*(d\omega/dp)$, where, B_0 and ω_0 represent the isothermal bulk modulus and the mode frequency at ambient conditions[106]. The ω_0 for the modes of the monoclinic phase are taken from the spectrum collected from the high pressure retrieved sample. *dω/dp* is calculated from a linear fit to the pressure variation for different modes. The *γ* for some of the observed modes for both cubic and monoclinic structure has been claculated using the bulk modulus reported in this study. The obtained *γ* values are tabulated in the Table 4.3. To the best of our knowledge, this is the first report on the *γ* of both monoclinic and cubic Tm_2O_3.

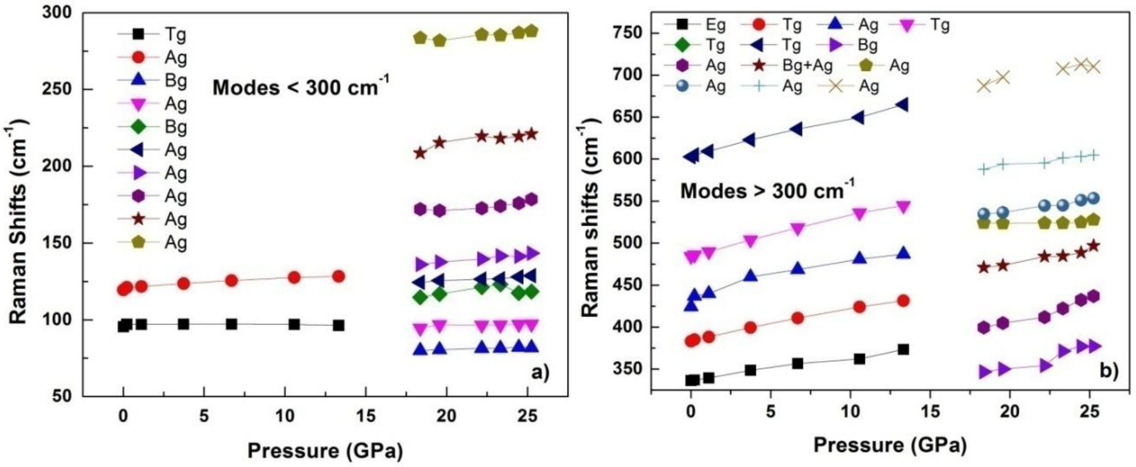

Fig. 4.7 Pressure dependence of the mode frequencies of cubic and monoclinic structure on compression a) Modes <300 cm^{-1} b) Modes >300 cm^{-1}.

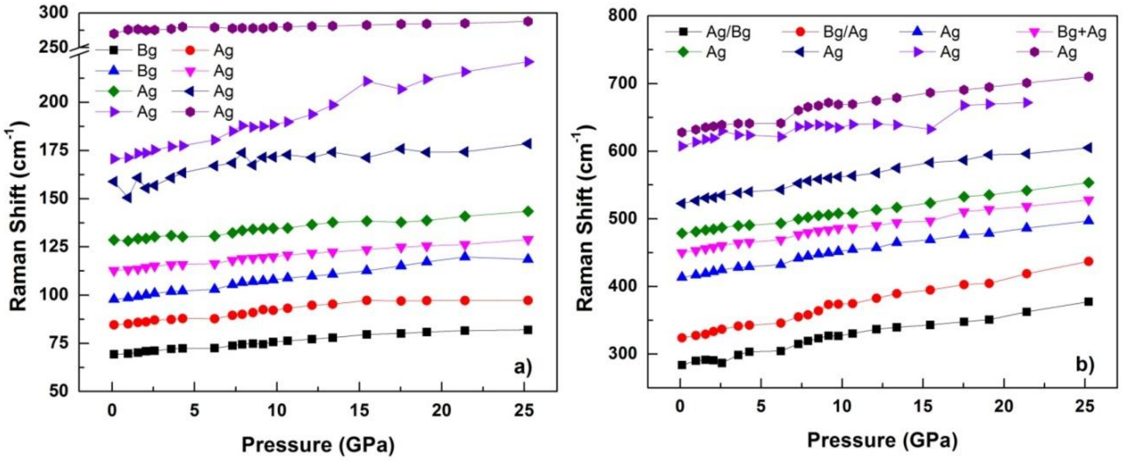

Fig. 4.8 Pressure dependence of the mode frequencies of monoclinic structure on decompression a) Modes <300 cm^{-1} b) Modes >300 cm^{-1}

Table 4.3 Mode Gruneisen parameters for the observed Raman modes of cubic and monoclinic structures

Mode	ω_0 **(cm^{-1})**	**dω/dp**	γ_i	**Mode**	ω_0 **(cm^{-1})**	**dω/dp**	γ_i
Cubic				**Monoclinic**			
$\mathbf{E_g}$	336.5	2.66	1.18	$\mathbf{B_g}$	320.8	5.38	2.83
$\mathbf{T_g}$	383.4	3.66	1.42	$\mathbf{A_g}$	414.6	3.42	1.39
$\mathbf{A_g}$	424.5	4.32	1.52	$\mathbf{A_g}$	479.4	2.71	0.95
$\mathbf{T_g}$	484.4	4.65	1.43	$\mathbf{A_g}$	523.8	2.30	0.74
$\mathbf{T_g}$	602.9	4.51	1.11	$\mathbf{A_g}$	628.3	3.31	0.89

4.2.3. *Ab-initio* density functional calculations

Density functional theory (DFT) calculations on Tm_2O_3 have been carried out using the VASP code. The enthalpies of type-C and type-B structure of Tm_2O_3 were calculated up to 14 GPa within the DFT frame work using the Generalized Gradient Approximation (GGA) and is shown in the Fig. 4.9. The enthalpy curve of type-C structure crosses the type-B structure at a pressure of around 8 GPa, where the monoclinic phase becomes stable over the cubic phase. The calculated free energy curves (see inset of Fig. 4.9) at 5 GPa and 10 GPa clearly shows the stability of the monoclinic over the cubic phase above 10 GPa. The predicted transition pressure is found to underestimate the experimental value of 11.5-12.4 GPa. This early onset of phase transition could be a consequence of the higher compressibility, compared to the experimental value, of the high pressure monoclinic phase obtained from the DFT. Nevertheless, the calculation predicts a bulk modulus of 146.3 GPa and 151.2 GPa for the cubic and monoclinic phase respectively which are in good agreement with the present experimental results. Moreover, the calculated compressibility behaviours (see Fig. 4.4) of both monoclinic and cubic phase also have a good agreement with our experimental data.

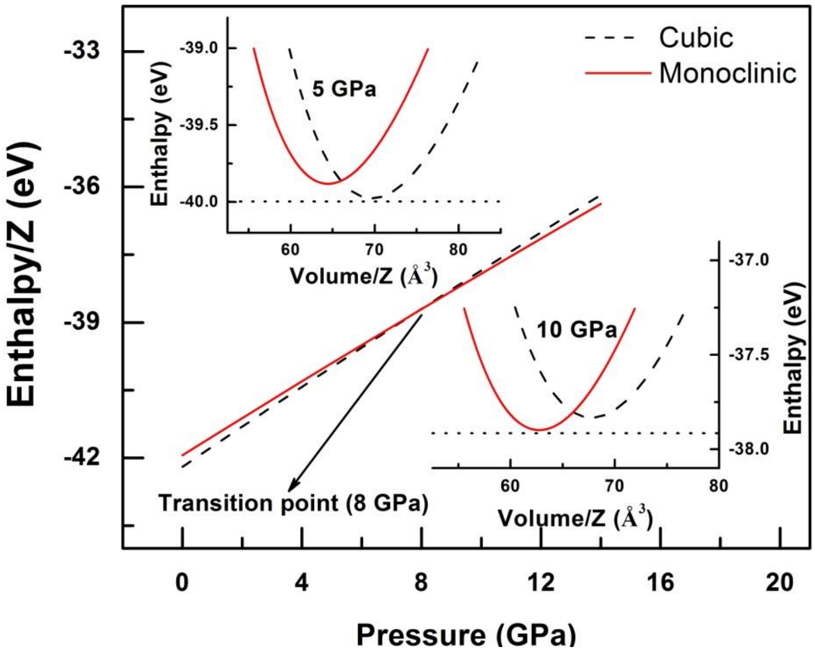

Fig. 4.9 Enthalpy Vs pressure showing the stability of both the cubic and monoclinic structure. Both the curves cross at ~ 8 GPa, where the C→B phase transition is predicted. The inset shows the calculated enthalpy at 5 and 10 GPa for both cubic and monoclinic phase indicating lower enthalpy of monoclinic phase above the transition pressure

The electronic density of states (DOSs) at 0 GPa and 8 GPa for the cubic structure and at 10 GPa for the monoclinic structures have been calculated. Fig. 4.10 a&b show the calculated DOS for the cubic and monoclinic structure at 0 GPa and 10 GPa respectively. The computed band gap of cubic Tm_2O_3 is 3.96 eV, which is found to be lower than the experimental value 5.4 eV[25]. The above discrepancy is due to the fact that, the simple LDA/GGA functionals are inadequate to treat the highly localized *f*-states and itinerant *spd*-states of Lanthanide oxides on an equal footing[26]. The itinerant *spd* states remain uncorrected even after the Hubbard U corrections to the localized *d* or *f* states[26]. In-order to reproduce the exact band gap one has to employ the many body perturbation theory in GW approach[26], which requires enormous computational power. In both cubic and monoclinic structure, the major contribution to the DOS of valence band is from the O-*p* states whereas the Tm-*d* states contribute more to the conduction band. The second significant contribution to the valence band is from Tm-*p* and Tm-*d* states. The former contributes more to the upper valence band while the later to the lower valence band. To understand the pressure effects on the DOS of cubic phase, the calculated total DOS at 0 GPa and 8 GPa are plotted together in Fig. 4.10c. At 8GPa, an increase in the DOS near the Fermi level signifies the instability of the cubic structure. Moreover, a slight increase in the width of the valence band at a pressure of 8 GPa indicates the increasing delocalization of atomic orbitals in the valence band. In Fig. 4.10d, the total DOS calculated for the cubic structure at 8 GPa together with the high-pressure monoclinic structure at 10 GPa is shown. It is seen that, the monoclinic phase has a lower DOS compared to the cubic phase near the Fermi level. Also, the width of the conduction band in the monoclinic phase is appreciably smaller indicating the highly localized nature compared to the cubic structure.

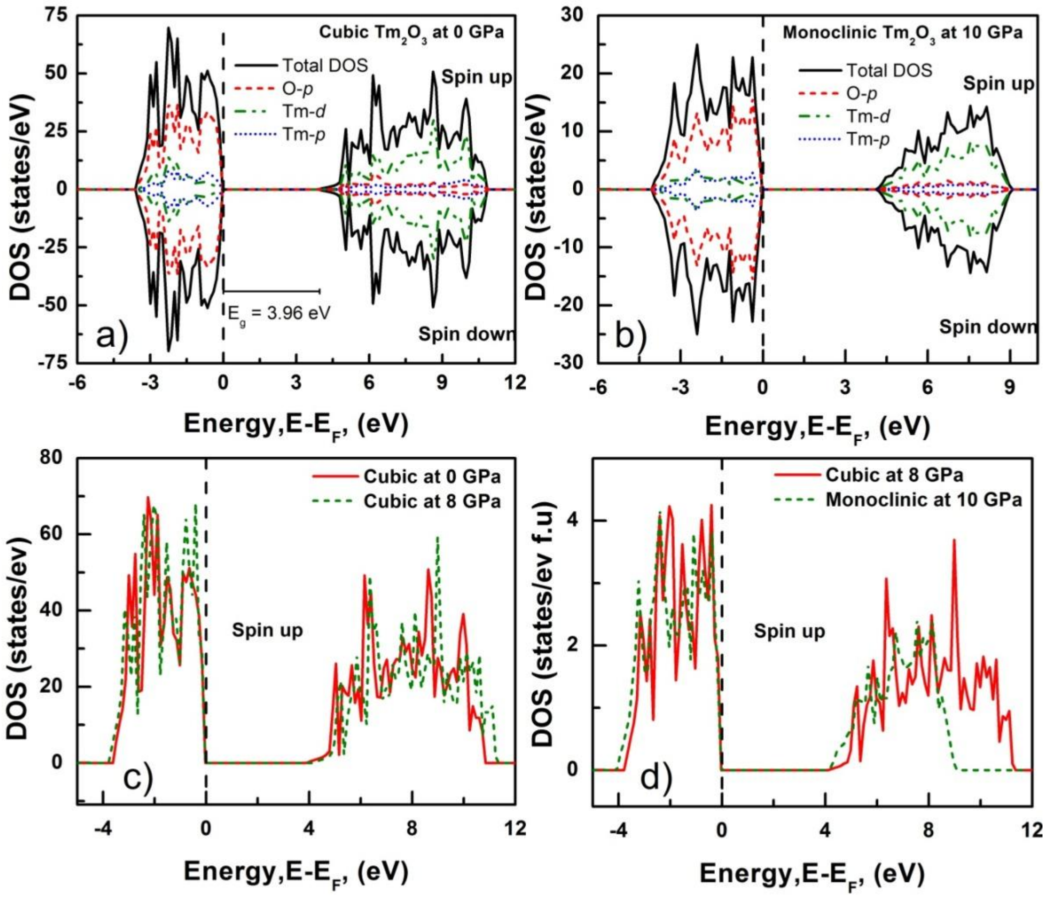

Fig. 4.10 The calculated partial DOS for the cubic and monoclinic structure at 0 GPa and 10 GPa respectively. c) Total DOS at 0 GPa and 8 GPa showing the increase in the DOS near the Fermi level at 8 GPa. d) Plot showing the reduction in the DOSs near the Fermi level once the system undergoes phase transition. The reduction in the width of the conduction band is also visible.

4.3. High pressure phase transition in Eu_2O_3

The following subsections will discuss the results of HPXRD measurements carried out on the B-type monoclinic structure of Eu_2O_3.

4.3.1. X-ray diffraction studies

Cubic Eu_2O_3 (99.9% purity, Alfa Aesar) powder was calcined at 1200 ºC for 12 hours to obtain the monoclinic (type B) phase. The calcined powder was ground well and characterized using the in house micro XRD setup (λ=0.711 Å). In order to confirm the phase purity, Rietveld structure refinement has been carried out to the as collected diffractogram. Fig. 4.11 shows the Rietveld fit to the diffraction data at ambient temperature and pressure. The observed diffraction peaks in the ambient structure could be indexed to the monoclinic phase (type- B) alone with space group (SG) *C*2/*m*[96]. The fairly good fit to the diffraction data shows, there is no trace of cubic phase or any other impurity phases in the observed diffraction data.

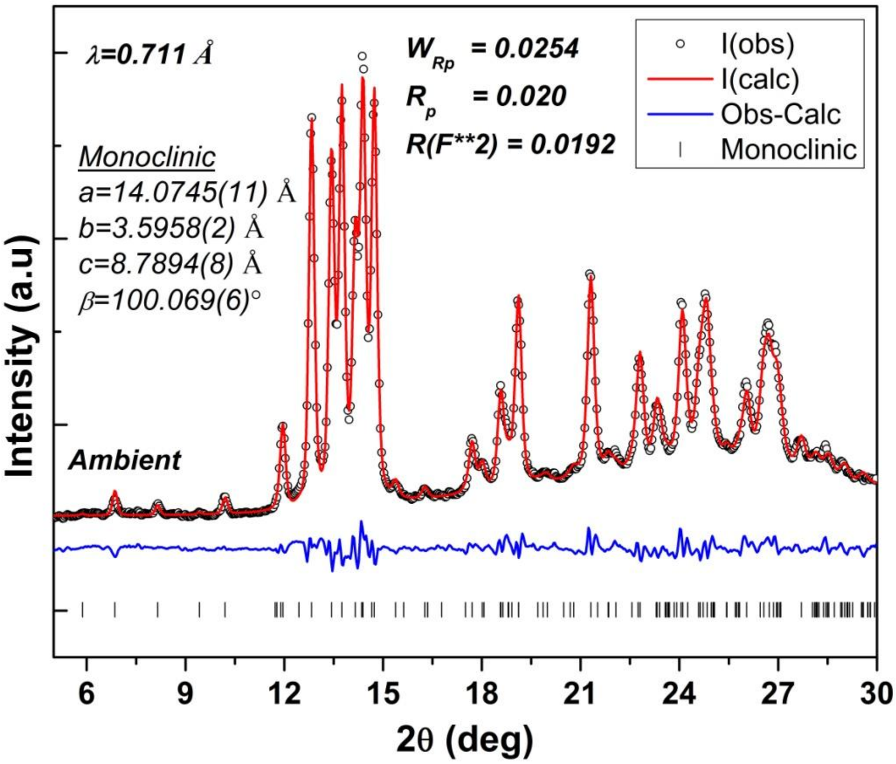

Fig. 4.11 Rietveld plot of the ambient pressure XRD data showing the pure single phase monoclinic structure. The different agreement indices and refined lattice parameters are ascribed in the figure.

Angle dispersive X-ray diffraction pattern (ADXRD) of Eu_2O_3 recorded at various pressure steps at 298 K are shown in Fig. 4.12 a&b. Up to a pressure of 4.3 GPa, a shift in the diffraction peaks towards the higher 2θ angle have been observed, but no structural transition could be observed. As the pressure was increased, a clear broadening of the diffraction peaks could be observed in the monoclinic phase signifying an increase in strain, a common effect in the HPXRD, in the parent phase. At 4.3 GPa, a clear splitting of the *111* peak at 2θ = 12.87° (see Fig. 4.12b) and the emergence of a new high intense peak, near the parent *310* peak, were observed. These clearly signify the onset of a phase transition. The new high pressure phase is indexed to the hexagonal phase (type A) with space group *P-3m1*[96]. The parent monoclinic phase coexisted with the high pressure hexagonal phase up to a pressure of 13 GPa. The high pressure hexagonal phase was found to be stable up to the highest pressure measured, 26 GPa. A substantial broadening of the hexagonal peak with *hkl* index *100* along with no appreciable shift in 2θ position was observed in the 15-25 GPa pressure range. Upon releasing the pressure a significant broadening of the hexagonal *101* peak was observed at 6.8 GPa. The hexagonal phase returned to the parent monoclinic phase when decompressed to the ambient pressure, indicating the reversible nature of the phase transition. B→ A phase transition in medium sized RES, like Sm_2O_3 and Eu_2O_3 have been reported earlier. Sm_2O_3 is found to transform at a pressure of 3.2 GPa, while it was 4-4.7 GPa for Eu_2O_3[35-37]. The observed transition pressure for Eu_2O_3 in the current experiment is found to be in good agreement with the earlier available reports.

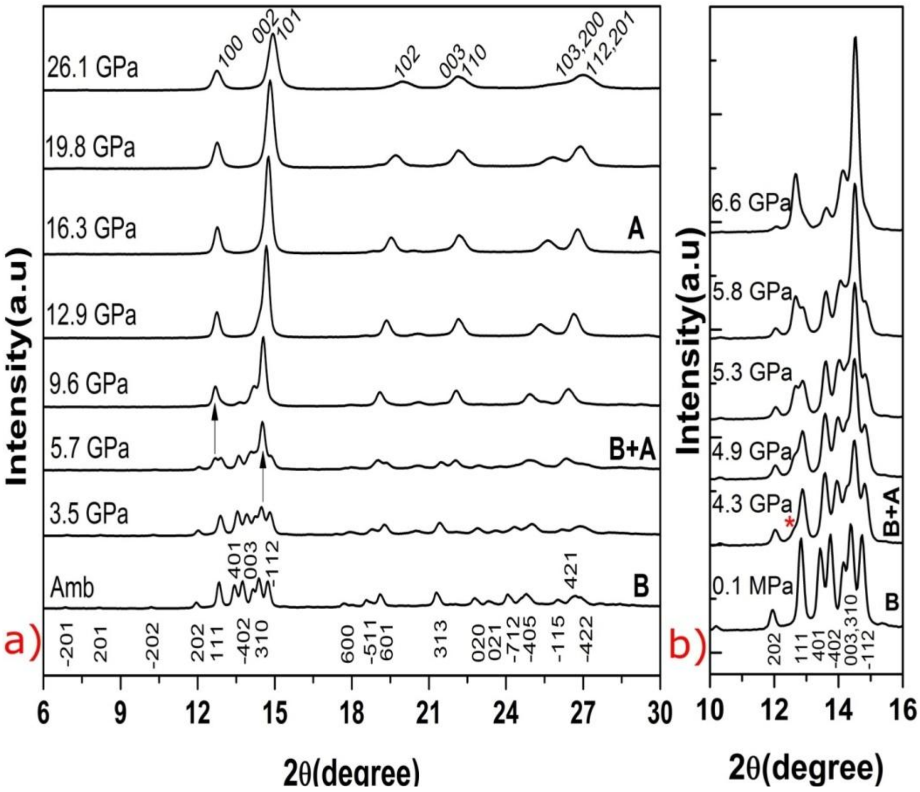

Fig. 4.12 a) HPXRD pattern representing the B→A transition in Eu_2O_3. The ambient and high pressure phases are indexed to monoclinic and hexagonal phase respectively. The arrows indicate the onset of phase transition. b) Experiment repeated with lower pressure steps, the onset of phase transition at 4.3 GPa is indicated with an asterisks.

Rietveld refinement was carried out for all the high pressure X-ray diffraction patterns using the GSAS+EXPGUI software package[70, 71] in order to obtain the structural parameters in the pristine monoclinic type –B phase and also in the transformed hexagonal type-A phase. The refinement was performed by considering the monoclinic Eu_2O_3 and hexagonal Nd_2O_3 as the starting structural models for the parent and high pressure phases respectively[96]. Atomic positions were refined by keeping all the other structural parameters constant. Fractional atomic co-ordinates for monoclinic phase at 3.5 GPa and high pressure hexagonal phase at 19.8 GPa obtained after the Rietveld refinement are listed in Table 4.4. There is no preferred orientation effect observed in the HPXRD patterns. Fig. 4.13 represents the Rietveld fit to the X-ray diffraction data at a pressure of 5.7 GPa. The R factors are reasonable, indicating a good quality fit to the experimental data.

Table 4.4 Refined values of fractional atomic co-ordinates of the parent monoclinic phase of Eu_2O_3 at 3.5 GPa and the high pressure hexagonal phase at 19.8 GPa.

Atom	**x/a**	**y/b**	**z/c**	**Atom**	**x/a**	**y/b**	**z/c**
Monoclinic phase				**Hexagonal phase**			
O_1	0.130(3)	0.0	0.263(4)	Eu_1	0.3333	0.6667	0.262(2)
O_2	0.339(4)	0.5	0.005(5)	O_1	0.0	0.0	0.0
O_3	0.305(5)	0.5	0.331(7)	O_2	0.3333	0.6667	0.697(6)
O_4	0.422(4)	0.0	0.316(4)				
O_5	0.0	0.5	0.0				
Eu_1	0.1424(6)	0.5	0.4888(6)				
Eu_2	0.1944(8)	0.5	0.1395(8)				
Eu_3	0.4672(7)	0.5	0.190(1)				

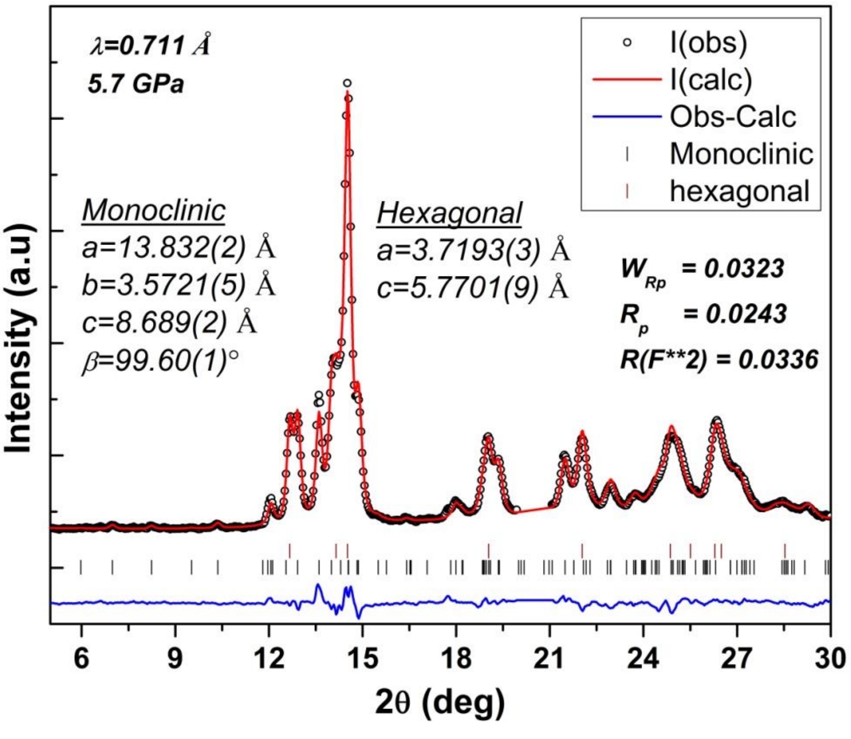

Fig. 4.13 Rietveld fit to the HPXRD data at 5.7 GPa. Different agreement indices are indicated in the figure. Tick marks represent the different phases. Refined lattice parameters at 5.7 GPa for both phases are also indicated.

Lattice compressibility of B-type Eu_2O_3:

Fig. 4.14 represents the variation of lattice parameters of the parent monoclinic phase up to a pressure of 8 GPa. A decrease in lattice parameters with an increase in pressure was observed in the monoclinic phase. These pressure variations of lattice parameters were fitted to the Birch-Murnaghan EOS by considering the cube of the individual lattice parameters[107]. The EOS fit to these parameters resulted in axial compressibilities of β_a=3.33(5) x10^{-3} GPa^{-1}, β_b=1.18(3) x10^{-3} GPa^{-1} and β_c=2.11(4) x10^{-3} GPa^{-1} for *a*, *b* and *c* axes respectively. The axial compressibility is found to be higher in the direction of *a* axis and it can be seen that the compressibility of the parent monoclinic structure follows $\beta_a > \beta_c > \beta_b$. It should be noted that, the compressibility of the *b* axis is lesser compared to both *a* and *c* axis. Such an anisotropic compressibility behaviour was observed in the high pressure phase of isostructural Sc_2O_3[108]. This could be due to the existence of voids along these crystallographic directions, which deforms the unit cell to a greater extent[108].

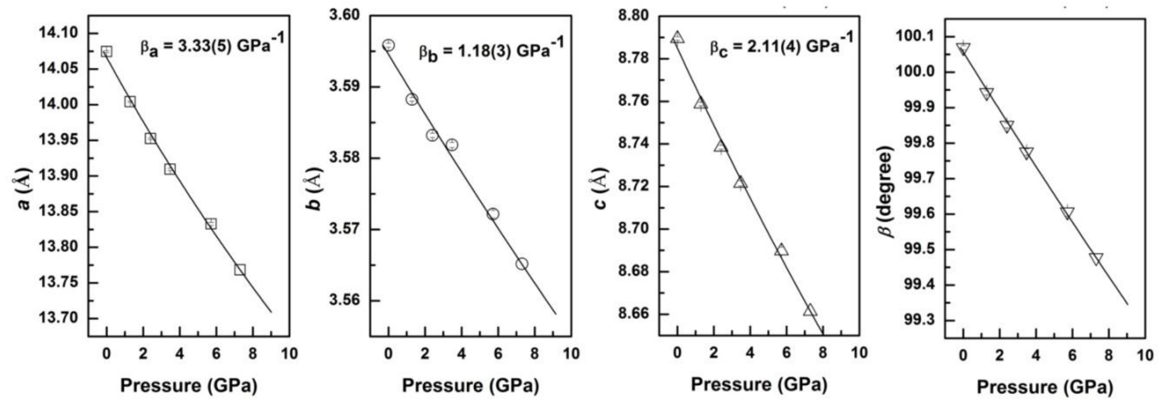

Fig. 4.14 The variation of monoclinic lattice parameters with pressure. The solid lines indicate the EOS fitting as described in [107]. The axial compressibilities quoted are to be multiplied by a factor of 10^{-3}

Anomalous lattice compressibility of hexagonal phase

The hexagonal lattice parameters were observed to be varying anomalously with the increase in pressure. The *a* axis shows a steep decrease up to a pressure of 15 GPa and becomes rigid/less compressible in the 15-25 GPa range. In conjunction with this anomalous behaviour of the hexagonal *a* axis, the *c* axis also shows two different compressibility behaviours. Such an anomalous axial compressibility in the *a* axis was also observed in the intermediate RES, Gd_2O_3[10]. The variation of lattice parameters with pressure is fitted to the Birch-Murnaghan EOS by cubing the individual parameters[107]. Separate EOS fits have been carried out in the two regions, 6-15 GPa and 15-25 GPa. Fig. 4.15 shows EOS fitting to the pressure induced changes in lattice parameters in the two pressure ranges. A visual comparison is made with the data digitized from the earlier reports of Eu_2O_3 and Gd_2O_3[4, 10] which shows a similar trend in the compressibility behaviour. The EOS fitting to the current experimental data yielded axial compressibilities of β_{a1}= 1.05(2) x10^{-3} GPa^{-1} and β_{c1} = 5.23(18) x10^{-3} GPa^{-1} respectively for *a* and *c* axis in the range 5-15 GPa. In the range 15-25 GPa, the *a* axis becomes harder and the EOS fitting to the *c* axis has yielded an axial compressibility of β_{c2} = 11.39(66) x10^{-3} GPa^{-1}, indicating an increased compressibility of *c* axis in this range. The compressibility of the *c* axis is approximately 5 times greater than that of the *a* axis in the 5-15 GPa pressure range. Also, the compressibility of *c* axis in 15-25 GPa range is almost twice as in the 5-15 GPa pressure range. However, in both the cases the *c* axis is found to be more compressible than the *a* axis.

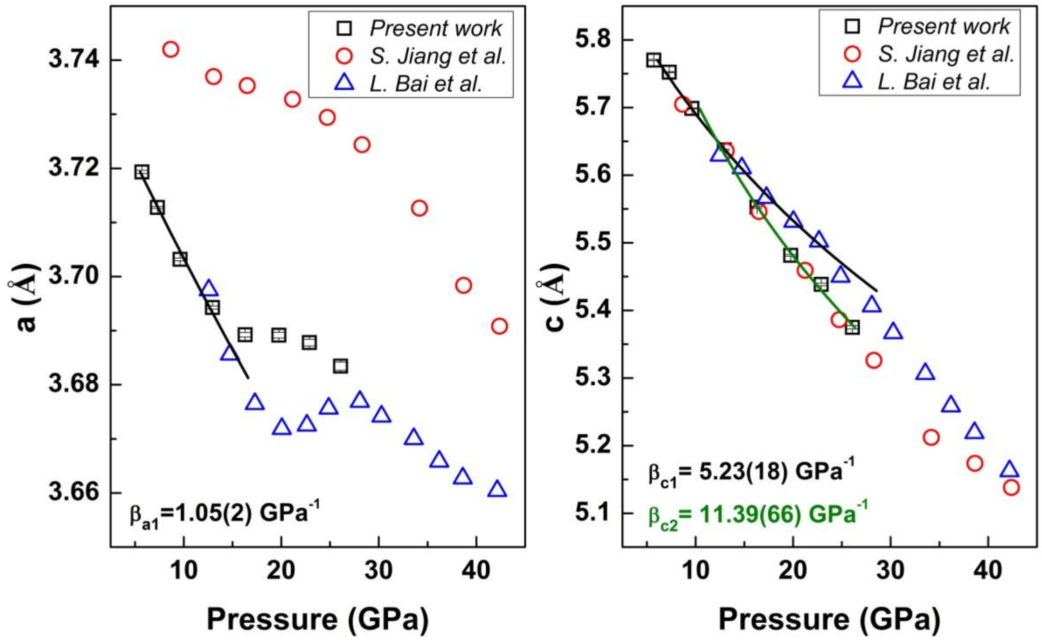

Fig. 4.15 Variations in hexagonal lattice parameter with pressure. Solid lines indicates the EOS fitting as described in[107]. Two distinct compressibility behaviour can be clearly seen. The axial compressibilities quoted are to be multiplied by a factor of 10^{-3}. The data digitized from references[4, 10] are included in the plot for a visual comparison.

This behaviour observed in the high pressure hexagonal phase of Eu_2O_3 under a B→A transition is not reported when a direct C→A transition occurred. Although the anomaly is clearly discernible in the data collected by Jiang *et al*, it was not quantified[4].

Unit cell compressibility and equation of state

The pressure dependence of the unit cell volume at room temperature is shown in Fig. 4.16. The anomalous behaviour of lattice parameter was not reflected in the pressure-volume data. This indicates that, the incompressible nature of the *a* axis in the 15-25 GPa is compensated by the *c* axis by doubling its compressibility as compared to the 5-15 GPa range. Supporting this, a consistent change in the c/a ratio has also been observed throughout the pressure range. Hence, the trend in volume change was consistent throughout the pressure range of investigation. The anomalous behaviour in the axial compressibility was observed at 91.73% of the ambient hexagonal volume (estimated from the EOS fitting). It is expected that, there could be an isosymmetric structural phase transition, which initiates around 15 GPa and completes at 25 GPa, driven by the modification in the electronic structure of the hexagonal phase. A similar behaviour was reported in the pressure induced C→B→A transition of Gd_2O_3, where the anomaly in the hexagonal *a* axis observed in the pressure range 20.1 - 28.1 GPa [10] in turn reflected in a discontinuity in the volume change. Moreover a pressure dependent shift of *100* peak towards the lower angle is observed in Gd_2O_3, indicating a lattice expansion with pressure in this material[109]. These reports along with our present experiments confirm the existence of an anomalous behaviour in the lattice compressibility of high pressure hexagonal phase of intermediate RES. The P-V data for both the phases are fitted to the Birch-Murnaghan EOS (see section 2.4.3). Fitting the experimental data to the EOS, by fixing B_0' =4, results in the bulk moduli of 159(9) GPa and 165(6) GPa and the ambient volume of 72.89(8) $Å^3$ and 71.35(17) $Å^3$ for monoclinic and hexagonal phases respectively. The bulk modulus of both monoclinic and hexagonal phase is more or less the same, indicating similar compressibility for both the structures. The phase transition from type-B monoclinic to type-A hexagonal structure is accompanied by a 2 % volume collapse at 4.3 GPa. Table 4.5 shows the bulk modulus, transition pressure and volume collapse for the monoclinic RES available in the literature. The reported bulk modulus for Eu_2O_3 is found to be slightly smaller compared to the present experimental results. This could be due to the use of methanol ethanol water as pressure transmitting medium, which is known to be more hydrostatic than the silicone oil used in the previous experiments.

Table 4.5 Comparison of bulk modulus, transition pressure and volume reduction of the monoclinic intermediate RES. Present experimental values are in bold.

RES	B_0 (B-type)	B_0 (A-type))	P_t (GPa)	V_{red}(%)
Sm_2O_3	118(2)[3]	125[3]	3.2[37]	2[3]
	153(7)[32]	155(5)[32]	2.6[110], 2.5[32]	1.9[32]
Eu_2O_3	141[35]	151(6)[4]	4.7[35]	1.6[35]
	159(9)	**165(6)**	**4.3**	**2**
Gd_2O_3	147(3)[10]	174(11)[10], 160(21)[5], 142(14)(a)[109]	6.2[5], 8.9[10]	-

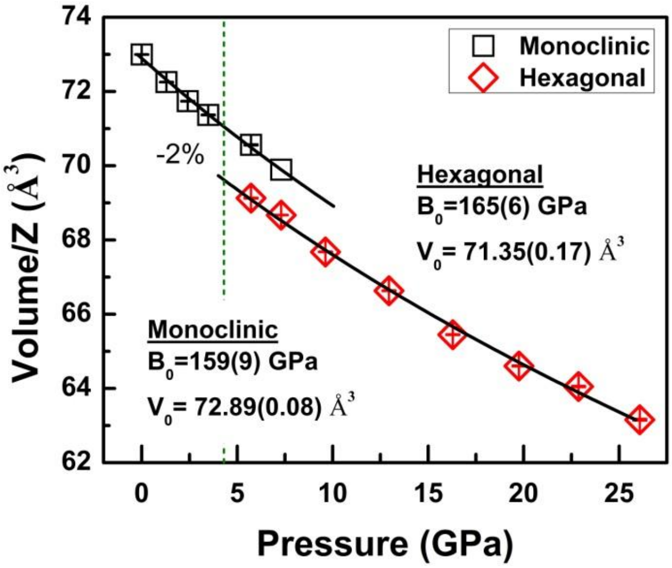

Fig. 4.16 The unit cell compressibility data of Eu_2O_3. Solid lines are the Birch-Murnaghan EOS fit to the experimental data. The bulk modulus, volume reduction and the zero pressure volumes are shown in the figure.

4.4. High pressure studies on La_2O_3

To understand the presence and origin of the observed anomalous lattice compression, a pure A-type RES has been studied under pressure. As there has been no detailed study on the high pressure behavior of A-type La_2O_3, this has been selected for the present study and the results are discussed in the following subsections.

4.4.1. X-ray diffraction studies

Hexagonal La_2O_3 (99.9% purity, Alfa Aesar) powder was preheated at 800 ºC for 12 hours to remove the moisture, carbonates and hydroxides present. This powder was ground well and characterized by angle dispersive X-ray diffraction technique with λ=0.449 Å at Indus 2 synchrotron facility, RRCAT, Indore, India. In order to confirm the phase purity, Rietveld structure refinements have been carried out to the as collected diffractogram. Fig. 4.17 shows the Rietveld fit to the diffraction data at ambient temperature and pressure. The observed diffraction peaks in the ambient structure could be indexed to the hexagonal phase (A-type) with space group (SG) *P-3m1*[111]. It can be seen that, there is no trace amount of carbonates, hydroxides or any other impurity phase present in the observed diffraction data.

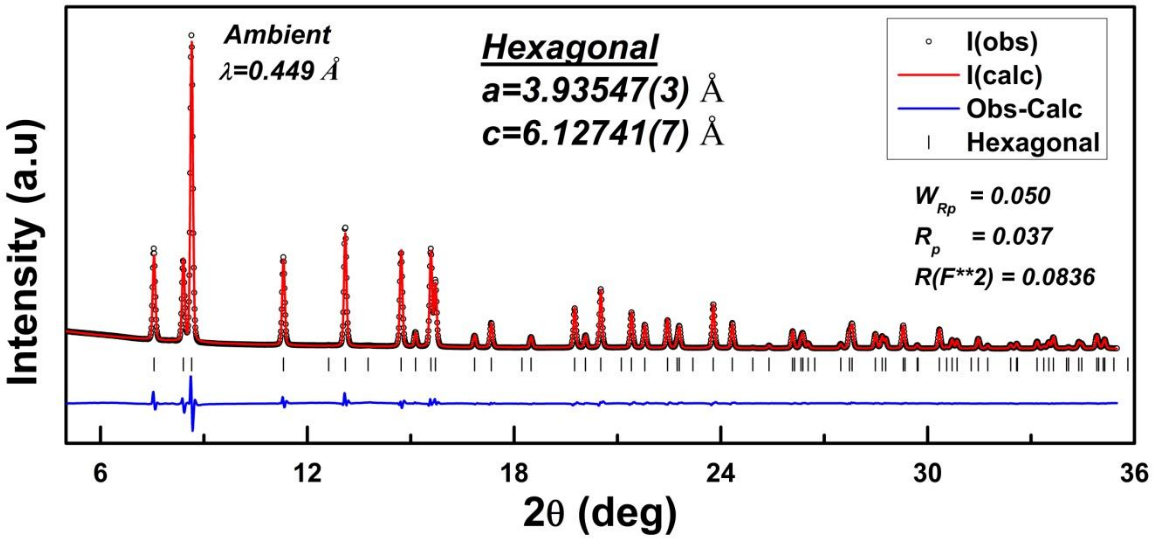

Fig. 4.17 Rietveld fit of the ambient pressure XRD data of La_2O_3 showing the pure single phase hexagonal structure. The different agreement indices and refined lattice parameters are explained in the figure.

Angle dispersive X-ray diffraction pattern (ADXRD) of La_2O_3 recorded at various pressure steps at room temperature are shown in Fig. 4.18 a&b. A shift in the diffraction peaks towards higher 2θ angle is observed, but no structural transition could be observed till the highest experimental pressure, i.e. 26.5 GPa, signifying the structural stability of hexagonal phase of La_2O_3. The observed increase in the FWHM of the X-ray peak within the hydrostatic limit is indicative of the increasing strain in the structure[112]. Another important feature observed here is that the diffraction peak corresponding to the *100 hkl* reflection has been found to be hardly shifting with the pressure in the region 9.7-19.8 GPa. Fig. 4.18b shows the high pressure X-ray diffraction pattern with 2θ limited to 7-10 degree. It can be clearly seen that there is no shift in the observed *100* peak in the above pressure region. In order to show this effect clearly, the shift in the position of *100, 110* and *102* peaks with pressure is plotted in the Fig. 4.19a. Both the *100* and *110* peaks are influenced by the compression along the *a* (hence *b*) axis direction whereas the peak corresponding to the *102* reflection is influenced by the compression along both *a* and *c* axis of the hexagonal structure. It is clear that, the peaks influenced by the hexagonal *a* axis follow a non monotonous shift whereas, the peak influenced by both a and c axis follows a consistent increase in 2θ towards higher angle. Also, Fig. 4.19b shows variation of the FWHM of the *100, 110* and *102* peaks in the whole pressure range studied in this experiment. The FWHM follows a similar kind of systematic behaviour for all the investigated peaks throughout the pressure range studied. This indicates that, the immobility in peak position is real and not due to the lack of quasi hydrostatic conditions. Such an anomalous behaviour was reported in the high pressure hexagonal phase of Gd_2O_3 and Eu_2O_3 in the 20.1-28.1 GPa and 15-25 GPa pressure range respectively[10, 29]. In the case of Eu_2O_3, the incompressibility of the *a* axis in the 15-25 GPa pressure range is balanced by the doubling of the compressibility along the *c* axis, leading to the usual compressibility behaviour of the unit cell volume. However, in a recent report on isostructural Nd_2O_3, it is shown that this anomalous behaviour starts at a comparatively lower pressure range, 10.2-20.3 GPa[9]. These substantiate the fact that, the observed anomaly is a characteristic feature of the hexagonal structure of RES. The authors have postulated that, an isostructural electronic transition resulting from the overlapping of electron wave functions along the *c* axis as a possible reason for this behaviour[9, 10]. However, this has not been confirmed so far. It is proposed that, electronic structure calculation may give more insights to the observed anomaly.

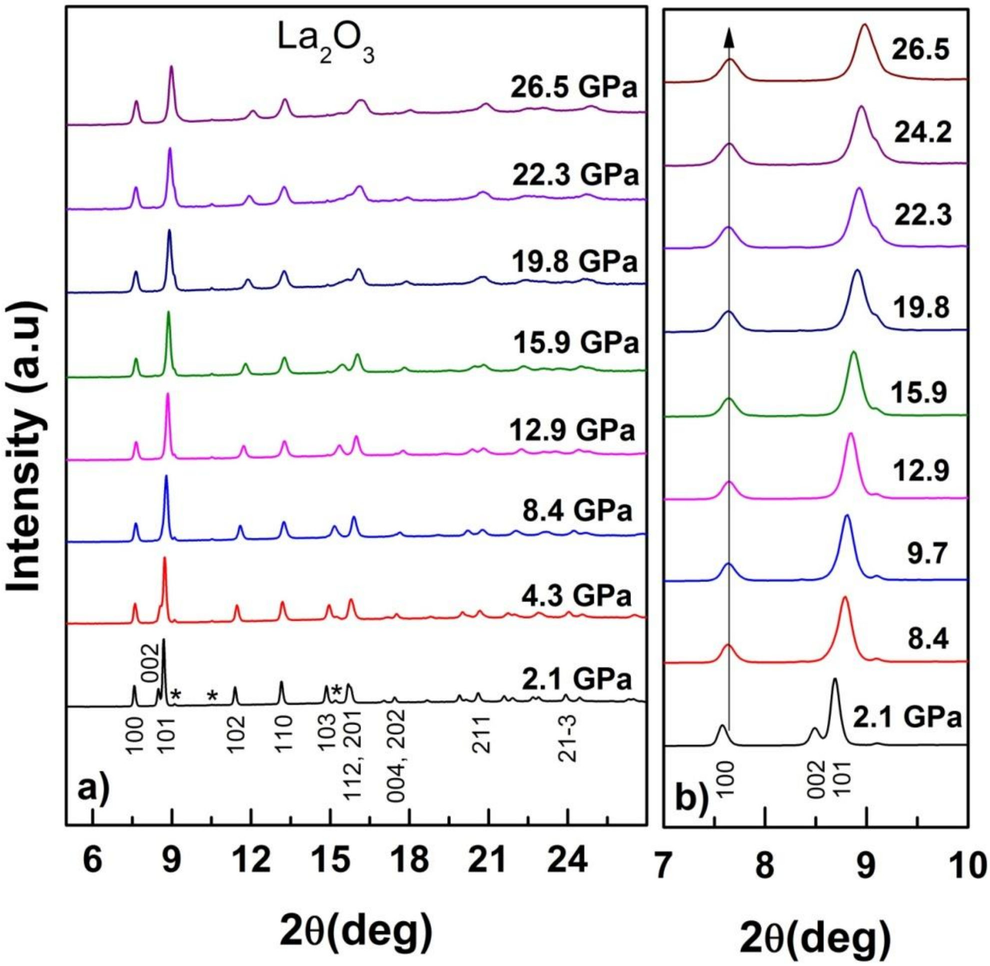

Fig. 4.18 a)HPXRD pattern of hexagonal La_2O_3 collected at various pressure steps. The ambient structure is indexed to the *P-3m1* space group. * marks indicate the Lead peaks observed due to the introduction of a X-ray slit near the diamond table (see Chapter 3 for details) b) The shift of 100 peak of the hexagonal structure with pressure. It can be seen that the 100 peak is hardly moving with pressure in the 9.7-22.3 GPa pressure region. The arrow is guide to the eye.

Even though a super lattice transition resulting from the doubling of the unit cell along the *c* axis is identified in the hexagonal structure of La_2O_3 [6], there are no super lattice reflections observed in the present experiment. HPXRD measurement on the Ce_2O_3 and Nd_2O_3 also has shown that there has been no super lattice transition present in the hexagonal phase of RES[7-9]. However, in the case of Nd_2O_3, a structural transition to a novel low symmetry monoclinic phase with space group *P21/m* at around 27 GPa[7] has been identified. This transition is characterized by the appearance of new diffraction peaks. Nevertheless, there is no such new reflection observed in the present experiment on La_2O_3 within the pressure range studied. Hence, the present experiment neither supports the structural phase transition to a super lattice structure nor a transformation to the predicted novel monoclinic phase.

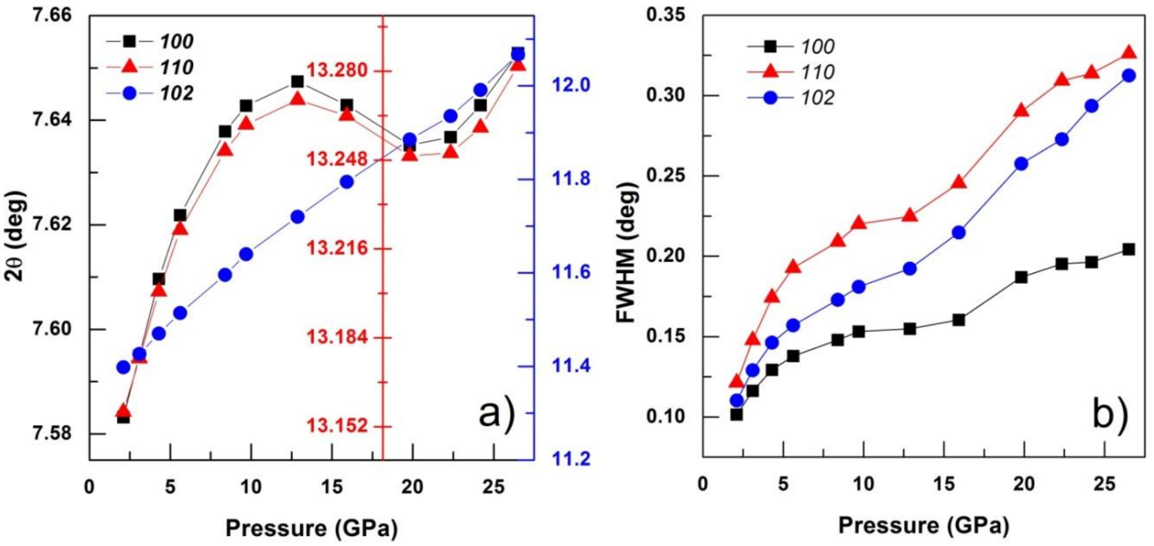

Fig. 4.19 a)Pressure dependant shift in the 2theta position of *100*, *110* and *102* peaks of hexagonal structure. b) Corresponding variations in the FWHM

In order to obtain the structural parameters of the hexagonal phase at each pressure, Rietveld structure refinement has been carried out for all the high pressure X-ray diffraction patterns using the GSAS+EXPGUI software package[70, 71]. The refinement was performed by considering the hexagonal structure derived from the Rietveld analysis of ambient X-ray data of La_2O_3 as the starting structural model. Above 5.6 GPa, the peak profile of *100* and *103* reflections was unable to model properly using the profile function 3 of the GSAS. A substantial difference in the intensity and FWHM of these peaks from the calculated one signifies the presence of anisotropic strain broadening. Hence, the peak profile is fitted with Stephens model of anisotropic strain broadening implemented in the profile function 4 of the GSAS software[113]. This model assumes a distribution of lattice parameters about its mean position and the width of each reflection is expressed in terms of moments of this distribution. The anisotropic strain contribution to the angular width in 2θ of a given reflection is $\delta 2\theta = (360/\pi)(\delta d/d)\, tan\theta$ where, $(\delta d/d) = \pi(S^2)^{1/2}/18000\, d_{hkl}^*$. Here S_{hkl} is the refinable parameter and the number of such parameters depends on the symmetry of the crystal structure. Symmetrically distinct S_{400}, S_{004} and S_{202} parameters are used to model the anisotropic strain in the present case of hexagonal structure. Further description of this model can be seen in the article by Stephens[113]. Atomic positions of RE and oxygen atoms have been refined independently by keeping all other structural parameters constant. The heavy La atom position was refined first followed by the atomic position of lighter oxygen atoms. Fig. 4.20 represent the Rietveld fit to the high pressure X-ray diffraction data at 24.2 GPa. The agreement indices and the difference curve show a good quality of fit.

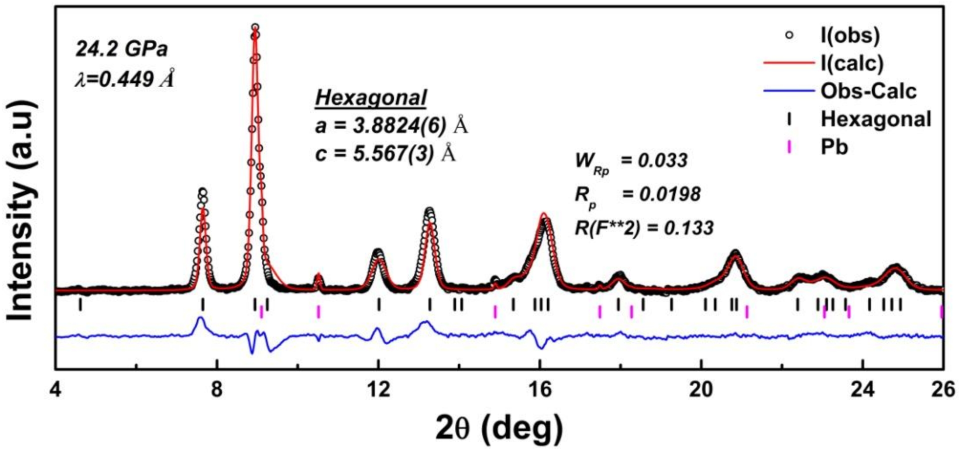

Fig. 4.20 Rietveld fit of the high pressure XRD data of La_2O_3 at 24.2 GPa. The different agreement indices and refined lattice parameters are shown. The presence of lead peaks is due to the introduction of an X-ray slit near the diamond table, see Chapter 3.

Lattice compressibility and equation of state

The pressure dependence of the unit cell parameters has been plotted in the Fig. 4.21a. The pressure variation of normalized lattice parameters shows an anisotropic compressibility behavior up to 9.7 GPa, where the *c* axis is more compressible than the *a* axis. This anisotropic compressibility has been reported in the isostructural hexagonal phase of large cation sized RES like Ce_2O_3 and Nd_2O_3[7-9]. Moreover this anisotropic nature was also observed in the high pressure hexagonal phase of Eu_2O_3, Gd_2O_3, Dy_2O_3 and Ho_2O_3[5, 29, 38, 39]. Due to the layer like structure, the mechanical stiffness along *a* or *b* axis of the hexagonal structure is larger than that of *c* axis[30]. Hence, the observed anisotropy could be due to the weak inter layer Van der waal interaction along the *c* axis. Above 9.7 GPa, the *a* axis shows an anomalous compressibility behavior compared to the *c* axis. The *a* axis is found to be expanding up to 19.8 GPa, then it follows a normal compression behavior. Such an anomalous behavior is not prominent along the *c* axis and the compression is normal in this direction. But similar anomalous compression along the *a* axis of the hexagonal structure has been reported earlier in the high pressure hexagonal phase of Eu_2O_3 (section 4.3), Gd_2O_3 and Er: Gd_2O_3[10, 28]. In the case of Eu_2O_3, the incompressibility along the *a* axis in the 15-25 GPa pressure range is compensated by doubling of the compressibility along the *c* axis. The modification in the topology of the Fermi surface leading to an electronic transition as predicted in the case of Nd_2O_3, Gd_2O_3 and Er: Gd_2O_3 may have a role in this observed anomalous behavior[9, 10, 28]. However, the electronic structure calculations of A-type hexagonal structure of RES do not predict any electronic transitions under pressure[8, 30, 31, 114].

The pressure dependence of the unit cell volume at room temperature is shown in Fig. 4.21b. It can be seen that, the anomalous lattice compressibility has been carried over to the pressure volume data and a slight slope change in the compressibility curve has been observed in this region. This anomaly in the unit cell compressibility has been observed at a volume reduction of 6.55 % It may be possible that, an isostructural electronic transition could be initiating around 9.7 GPa and completing below 22.3 GPa as reported for Eu_2O_3, Gd_2O_3 and Nd_2O_3[9, 10, 29]. Similar to this, a pressure induced expansion in the lattice parameter and a slight discontinuity in the unit cell compressibility curve have been reported for the hexagonal Gd_2O_3 and Nd_2O_3[9, 10, 109]. These substantiate the fact that, the anomalous compressibility is a characteristic of the hexagonal structure of RES. Due to the presence of a slope change in the unit cell compressibility, the experimental pressure volume data has been fitted for the low pressure ($P \leq 9.7$ GPa) and high pressure region ($P \geq 22.3$ GPa) separately. The P-V data of the hexagonal La_2O_3 for $P \leq 9.7$ GPa has been fitted to the Birch-Murnaghan EOS (see section 2.4.3). The EOS fitting to the experimental data yielded a bulk modulus of 102(5) GPa with $B_0' = 9.8(1.0)$ and an ambient volume of 82.15(6) Å^3 for the hexagonal La_2O_3. The compressibility curve above 19.8 GPa has been fitted with the modified Birch - Murnaghan EOS (see section 2.4.3)[90, 91]. P_r has been fixed at 22.3 GPa, the pressure above which the anomaly has disappeared, and correspondingly V_r is fixed to 73.69 Å^3. Due to the insufficient number of data points in this region, the pressure derivative of bulk modulus has been fixed to 4. The bulk modulus at pressure P_r obtained by this method for the high-pressure region is 176(3) GPa. This is much higher than the one obtained at low pressure region, indicating a lower compressibility at high pressure region. Table 4.6 shows the pressure range (P_c) over which the anomaly is observed and the bulk modulus for the hexagonal structure of RES. Comparatively lower bulk modulus for the La_2O_3 from their isostructural Ce_2O_3 and Nd_2O_3 signifies the decreasing nature of compressibility with an increase in the *f* electron occupation. Also the P_c is found to be shifting towards the low pressure region with an increase in cationic radii and decreasing *f* electron occupation.

Table 4.6 Bulk modulus and the region of pressure with anomalous compressibility in the hexagonal phase of RES collected from literature.

Oxides	**P_c (GPa)**	**B_0 (GPa)** $P < P_c$	**B'$_0$**	**B_0 (GPa)** $P > P_c$	**B'$_0$**	**V_c(%)**	**References**
La_2O_3	**9.7-19.8**	**102(5)**	**9.8(1.0)**	**176.7(3.2)**	**4**	**6.55**	**Present work**
Ce_2O_3	-	111(2)[8]	4.7(3)	-	-	-	Lipp et al[8]
Nd_2O_3	10.2-20.3	142(4)	4	183(6)	4	-	Jiang et al [9]
	-	135.6[7]	4	-	-	-	Pandey et al [7]
Eu_2O_3	15-25	165(6)	4	-	-	8.27	Section 4.3.1
Gd_2O_3	20.1-28.1	174(11)	4	125(3)	4	-	Bai et al [10]

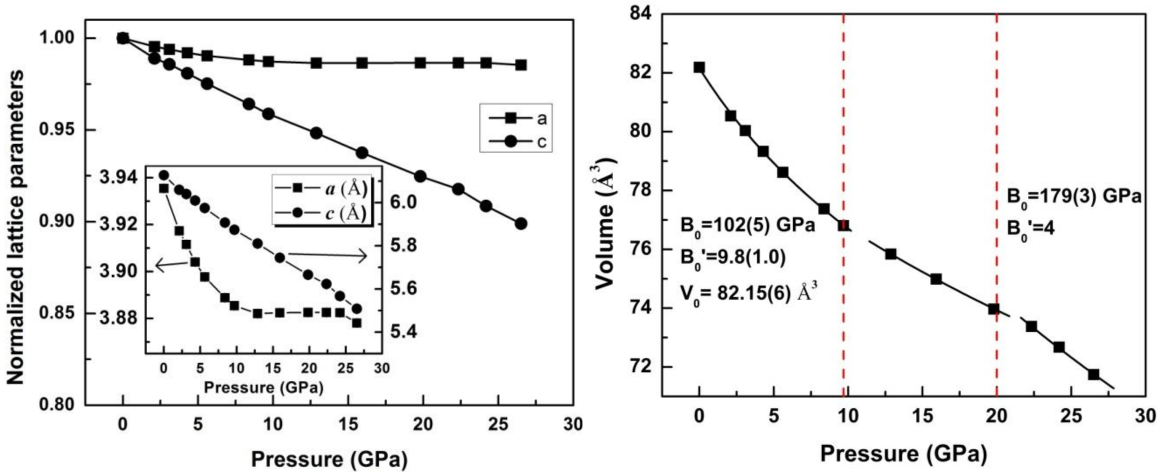

Fig. 4.21 a) Pressure dependence of the normalized unit cell parameters of the hexagonal unit cell, showing anisotropic compressibility of the *a* and *c* axis. The inset shows the pressure dependence of the *a* and *c* axis. The anomalous compressibility can be visualized clearly. b) Unit cell volume compressibility of La_2O_3. The vertical dotted lines separate the two pressure regimes as described in the text. The solid lines are the Birch-Murnaghan EOS fit to the experimental data. The bulk modulus, derivative of the bulk modulus and the zero pressure volumes are also depicted.

Pressure evolution of bond length and bond angles

The rare earth atom in the type-A structure is characterized by 7 fold co-ordination with the oxygen atoms. This 7 fold polyhedron consists of 3 different La-O bonds represented by La(1)-O(1), La(1)-O(2) and La(1)-O(3) (See section 1.2 of Chapter 1). The two cations in the unit cell are linked through O(1) and O(2) and the bond O(1) - O(2) lies in the *110* plane. La(1)-La(2) is the distance between the two rare earth atoms in the unit cell and this also lies in the *110* plane. The bond La(1)-O(1) is directed along the *c* axis whereas the La(1)-O(2) bond is roughly aligned in the *ab* plane. The pressure dependence of the different bonds present in the A-type La_2O_3 is represented in the Fig. 4.22a. It can be clearly seen that, the bond lengths vary monotonously with increasing pressure up to 4.3 GPa. La(1)-O(1), La(1)-O(3) and O(1)-O(2) distance decreases with pressure indicating the strengthening of these bonds whereas, the La(1)-O(2) shows an increase in this region signifying a pressure induced weakening of this bond. The Mulliken population analysis for the charge density of La_2O_3 at zero pressure has clearly shown that, O and La atoms carry negative and positive charges and are significantly different to the nominal valence states of O (-2) and La (+3)[30]. Also it has been shown that, the La(1)-O(3) and La(1)-O(2) bonds are mainly covalent, whereas La(1)-O(1), in the *c* direction, is perfectly ionic[30]. The covalency of La(1)-O(1) bond is found to be increasing with compression whereas, La(1)-O(2) bonds (aligned roughly on x-y plane) are found to be weakening more compared to the La(1)-O bonds in other directions. This is consistent with the experimental observation. However, in the region 9.7-19.8 GPa where an anomalous lattice compressibility is observed, the bonds behave irregularly with pressure. Consequently, O(1)-La(1)-O(2) bond angle is found to be decreasing with pressure till 4.3 GPa and shows an increasing trend above this pressure. In Fig. 4.22b, the variation of selected bond angles with increasing pressure is shown. It can be seen from the hexagonal structure of La_2O_3, the O(3)-La(1)-O(3) bond angle is related to the *a* axis (Fig. 1.1d). If the cation co-ordinate is assumed to be fixed, then the compression along the *a* axis should result in the reduction of O(3)-La(1)-O(3) bond angle. As there is no appreciable change along the *a* axis with increasing pressure in the region 9.7 - 19.8 GPa, the increasing O(3)-La(1)-O(3) bond angle might be a result of the pressure induced cation (La) movement.

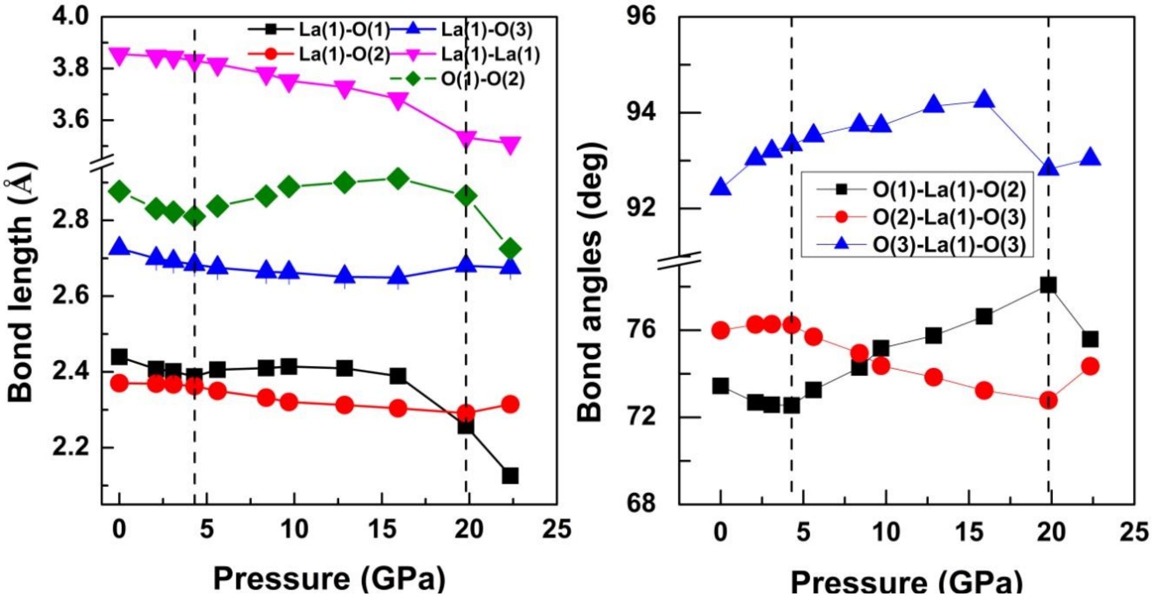

Fig. 4.22 The pressure dependence of: a) different bond distances and b) selected bond angles in the hexagonal La_2O_3 structure. The two dotted lines indicate the region where the anomalous bond behaviour is observed.

Anomalous compressibility and Layer motion

As we have stated earlier, a substantial change in the intensity of the two reflections, *100* and *103*, was the significant change observed in the diffraction pattern during the compression. The square of structure factor (F^2) of these reflections has been extracted through Rietveld structure refinement and is shown in the Fig. 4.23a. A significant increase in the intensity of the *100* reflection and a decrease in the intensity of *103* reflections can be clearly seen from 5.6 GPa onwards. As can be seen in the Fig. 4.23b, the hexagonal structure of La_2O_3 can also be visualized as a layer like structure, consisting of alternate layers of LaO composition[33]. In this representation, a single oxygen plane is stacked in between the two La atom planes. The *100* and *103* plane, where a substantial intensity variation has been observed with the increase of pressure is also shown in the Fig. 4.23b. From the observed, reduction in the F^2 of *103* plane and the significant increase in the F^2 of *100* reflection, it is speculated that, the atoms that are part of *103* plane could have been progressively moving towards the *100* plane with increase of pressure. Such an atomic movement can be realized if successive LaO layers slide over the other in opposite direction perpendicular to the *c* axis (see Fig. 4.23b). Pressure enhances this layered motion and drives the cations towards the *100* plane. As the cations move towards the *100* plane, the atom density in the *100* plane increases considerably with pressure leading to the anisotropic strain broadening and a significant increase of F^2. It can be stated that, above 5.6 GPa, pressure favors the movement of LaO layers in a direction opposite to each other in the *ab* plane rather than compressing along the *a* axis. Hence, an anomalous lattice compressibility is observed along the *a* axis.

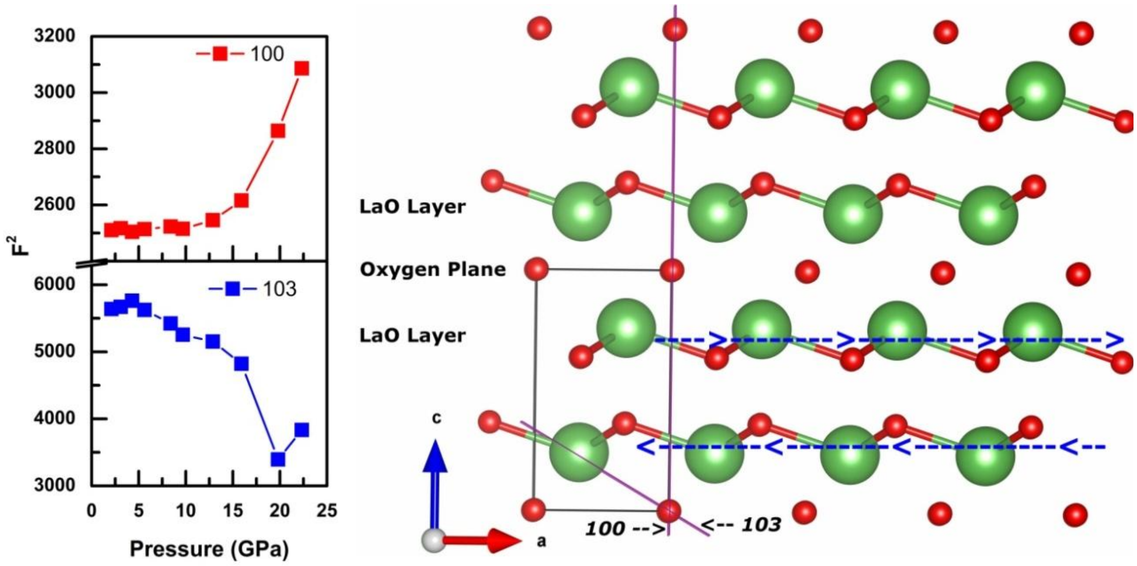

Fig. 4.23 a) The variation in intensity (F^2) of *100* and *103* reflections. The former increases with increasing pressure while the later shows a reduction. b) The layered structure of La_2O_3, in which a single layer of oxygen atoms is present in between two LaO layers. The blue dotted arrows represent the direction of motion of LaO layers.

4.5. Summary and conclusion

In order to understand the structural stability of small, medium and large cation sized RES, three candidate systems namely, Tm_2O_3, Eu_2O_3 and La_2O_3 respectively have been studied under high pressure.

In the case of C-type Tm_2O_3, both the X-ray diffraction and Raman spectroscopic measurements revealed an irreversible polymorphic structural phase transition from C-type cubic to B-type monoclinic at around12 GPa. This is in contradiction with the earlier X-ray diffraction studies in which the same transition was reported at 7 GPa. A zero pressure bulk modulus of 149(2) GPa with the pressure derivatives 4.8(5) for the parent cubic phase and 169(2) GPa with the pressure derivative 4 for the high pressure monoclinic phase, respectively are obtained and are in good agreement with the calculated value of 146 and 151 GPa for the cubic and monoclinic phase respectively. Raman modes for the monoclinic phase of Tm_2O_3 are measured and reported for the first time. The mode Grüneisen parameter of different Raman modes for both cubic and monoclinic phases of Tm_2O_3 has also been determined. The experimental results are correlated with changes in the DOS near the Fermi level which are indicative of structural instabilities in the parent cubic structure.

In the case of Eu_2O_3, pressure induced structural phase transition from monoclinic to hexagonal phase has been observed at 4.3 GPa with 2% volume collapse. Birch – Murnaghan equation of state fit to the pressure volume data yields a bulk modulus of 159(9) GPa and 165(6) GPa for the monoclinic and hexagonal phases respectively. The axial compressibility increases in the order $\beta_a > \beta_c > \beta_b$ for the parent monoclinic phase, showing the least compressibility along *b* axis. Contrary to the available reports, an anomalous lattice compressibility behaviour is observed for the high pressure hexagonal phase, characterized by pronounced hardening along the *a* axis above 15 GPa. The observed incompressible nature along the *a* axis of the hexagonal structure in the pressure range 15-25 GPa is found to be compensated by doubling the compressibility along the *c* axis.

In order to understand the observed anomalous lattice compressibility in the hexagonal rare earth sesquioxides (RES), angle dispersive high pressure synchrotron X-ray diffraction has been carried out for the pure hexagonal La_2O_3 sesquioxide. The *a* axis is found to be compressing up to a critical pressure of 9.7 GPa and then expanding in the region 9.7 GPa < P < 19.8 GPa. The Rietveld structure refinement in conjunction with the

Stephens anisotropic strain broadening model indicate the onset of this anomaly at an earlier pressure of 5.6 GPa, where an atypical bond compression behavior is observed. A significant increase in the intensity of *100* reflection and a reduction in the intensity of *103* reflections suggests a plausible movement of the LaO layers in the opposite direction resulting in the increase/decrease of the atom density of *100*/*103* plane. Bulk modulus value of B_0= 102(5) GPa with B'_0 = 9.8(1.0) in the region P ≤ 9.7 GPa and B_0= 177(3) GPa with B'_0= 4 in the region P ≥ 22.3 GPa are obtained from the EOS fitting.

Chapter 5

Synthesis, structural characterization and high pressure polymorphic phase transitions in $(Eu_{1-x}Ho_x)_2O_3$

5.1. Introduction

The aim of the present chapter is to investigate the effect of cationic radii and pressure on the solid solutions of RESs with similar structure and small difference in cationic radii. Till date, a comprehensive and systematic study which delineates the role of RE cation size in dictating a particular polymorphic structure type of RES is not reported elsewhere in the literature. A smooth variation in the cationic radii of RESs can be achieved by preparing their solid solutions. A systematic investigation on these solid solutions, both at ATP and at high pressures, would be beneficial in understanding the cation size and pressure effect on their crystal structure and phase transitions. To accomplish this, the solid solutions of Eu_2O_3, classified as a medium cation sized RES, and Ho_2O_3 , classified as small cation sized RES [19], with nominal formulae $(Eu_{1-x}Ho_x)_2O_3$, $(0 \leq x \leq 1)$, have been selected for the present study. At ambient conditions, it is known that, both Eu_2O_3 and Ho_2O_3 exist in the cubic structure crystallizing in the *Ia-3* space group. Eu_2O_3, being a medium cation sized RES, shows a direct C→A transition, whereas Ho_2O_3 is a small cation sized RES and it shows a C→B→A transition under pressure[4, 39, 40]. Moreover, as these two RES follow a different transition sequence, a clear cut idea about the limiting cation size, which decides the boundary of these different transition sequences, can be elucidated. Hence, the present chapter will cover the following aspects:

i. A soft chemistry approach to synthesis $(Eu_{1-x}Ho_x)_2O_3$ $[0.0 \leq x \leq 1]$ solid solutions.

ii. A detailed structural and optical characterization of $(Eu_{1-x}Ho_x)_2O_3$ solid solutions as a function of their mean cationic radii

iii. The conclusions drawn from the HPXRD studies on $(Eu_{1-x}Ho_x)_2O_3$

5.2. Chemie douce approach towards the synthesis of mixed RESs

Chemie douse method is a general soft chemistry approach of synthesizing ultra fine powder samples which involves reactions under moderate conditions typically with a temperature of T<500 ^{0}C. In this method of preparation, the structural elements of the reactants are preserved in the final product while the stoichiometry can be varied. The major advantage of this method is the formation of a homogeneous mixture by an atomistic level mixing of the reactants. This method of synthesizing is greatly useful in modifying the electronic structure of solids via doping. Therefore it has been employed to prepare the powder samples of mixed rare earth sesquioxides of $(Eu_{1-x}Ho_x)_2O_3$ and is described in the following section.

5.2.1. Synthesis of $(Eu_{1-x}Ho_x)_2O_3$

Commercially available Eu_2O_3 and Ho_2O_3 (99.9% purity, Alfa Aesar) have been used as starting material for the preparation of solid solutions, $(Eu_{1-x}Ho_x)_2O_3$ $[0.0 \leq x \leq 1]$, without any further purification. Eu_2O_3 and Ho_2O_3 were held in a furnace overnight at 900 °C to remove all the moisture, hydroxide and carbonate contents. The samples were prepared for 1g of the product according to the composition, $(Eu_{1-x}Ho_x)_2O_3$ $[0.0 \leq x \leq 1]$. Appropriate amount (see Table 5.1) of the constituents namely Eu_2O_3 and Ho_2O_3 were weighed, before they absorb moisture, in a weighing pan and transferred to a 500 ml beaker and the resulting mixture was dissolved in diluted (3:1) nitric acid and stirred well to dissolve completely. This solution was heated on a hot plate at around 200 °C to remove excess nitric acid and to ensure complete solubility of the solutes. The resulting solution was mixed with citric acid ($C_6H_8O_7$) and heated at a slow rate until a viscous gel was obtained. The gel was decomposed in air at high temperatures and calcined at 400 °C in a furnace for 6 hours to remove the excess carbon present in the final compound as CO_2. The powder thus obtained was ground well and heat treated at 900°C for 12 hours.

This method of preparation is relatively inexpensive and ensures stochiometrically reliable product formation.

Table 5.1 Nominal weight of the precursors, Eu_2o_3 and Ho_2o_3 taken for the synthesis of $(Eu_{1-x}Ho_x)_2O_3$ [$0.0 \leq x \leq 1$].

x	$(1-x)$*MW_{Eu}	x * MW_{Ho}	MW (g)	W_{Eu}	W_{Ho}	W_{Eum}	W_{Hom}	ΔW_{Eu}	ΔW_{Ho}
0.1	316.735	37.786	354.521	0.8934	0.1066	1.7872#	0.2139#	-0.0004	-0.0007
0.2	281.542	75.572	357.114	0.7884	0.2116	0.7886	0.21193	-0.0002	-0.0003
0.3	246.349	113.358	359.708	0.6849	0.3151	0.6848	0.3164	0.0001	-0.0013
0.4	211.157	151.144	362.301	0.5828	0.4172	0.5830	0.4214	-0.0002	-0.0042
0.5	175.964	188.930	364.894	0.4822	0.5178	0.4825	0.5181	-0.0003	-0.0003
0.6	140.771	226.716	367.487	0.3831	0.6169	0.3834	0.6182	-0.0003	-0.0013
0.7	105.578	264.502	370.081	0.2853	0.7147	0.2836	0.7154	0.0017	-0.0007
0.8	70.386	302.288	372.674	0.1889	0.8111	0.1891	0.8120	-0.0002	-0.0009
0.9	35.193	340.074	375.267	0.0938	0.9062	0.1877#	1.8129#	-0.0001	-0.0005

Prepared for 2 g of the product

MW_{Eu}: 351.928 g, molecular weight of Eu_2O_3
W_{Eu} : weight of Eu_2O_3 for 1g of product
W_{Eum} : measured weight of Eu_2O_3 for 1g of product
MW : total weight

MW_{Ho}: 377.8604 g, molecular weight of Ho_2O_3
W_{Ho} : weight of Ho_2O_3 for 1g of product
W_{Hom} : measured weight of Ho_2O_3 for 1g of product
ΔW_{Eu}, ΔW_{Ho} : error in measured weight

5.3. Crystal structure and optical characterization of $(Eu_{1-x}Ho_x)_2O_3$

The following sub sections will describe the results and conclusions drawn from the X-ray crystal structure characterization and the Raman spectroscopic studies on the as prepared samples of $(Eu_{1-x}Ho_x)_2O_3$.

5.3.1. Synchrotron X-ray diffraction studies

X-ray diffraction patterns of $(Eu_{1-x}Ho_x)_2O_3$ [$0.0 \leq x \leq 1.0$] collected at Indus-2 synchrotron facility at RRCAT, Indore, India are shown in Fig. 5.1. The diffraction patterns of all samples were found to have well resolved sharp peaks. All the diffraction patterns have been indexed to the known type-C cubic structure (*Ia-3*) based on the standard crystal structure data of Eu_2O_3 and Ho_2O_3 available at International Centre for Diffraction Data (ICDD) [115]. The diffraction data show a clear evidence for the formation of solid solution over the whole range of compositions. The diffraction patterns do not show any change except for intensity variation and a systematic shift in peak positions, indicating the formation of a pure single phase nature of the prepared mixed RES. The observed systematic shift in peak positions towards higher angles is attributed to the increasing Ho_2O_3 content; Ho_2O_3 has a lower lattice constant than Eu_2O_3 and hence causes a decrease in lattice parameter a as the concentration of Ho_2O_3 is increased.

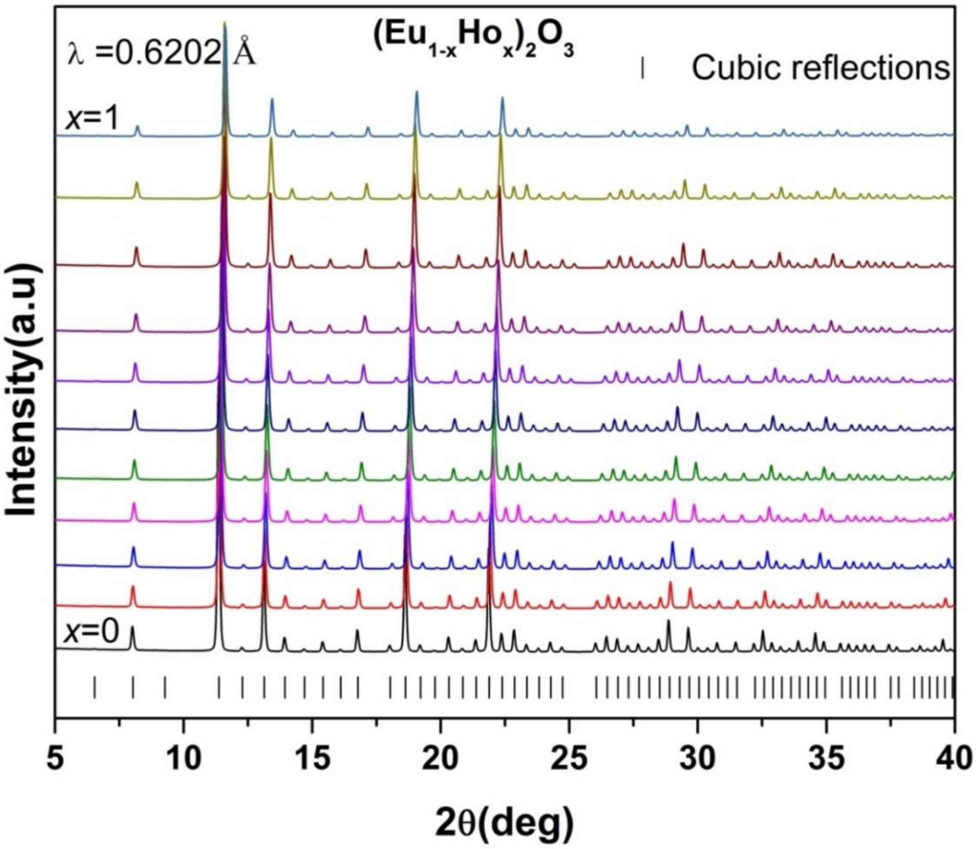

Fig. 5.1 X-ray diffraction pattern of $(Eu_{1-x}Ho_x)_2O_3$ $[0.0 \leq x \leq 1.0]$ collected at Indus 2 synchrotron facility at RRCAT, Indore India. All the peaks are indexed to type-C cubic structure with space group *Ia-3*.

5.3.2. Rietveld refinement

To understand the structural evolution in detail, Rietveld refinement has been carried out for all the diffraction patterns with the aid of GSAS+EXPGUI[70, 71] package. The model structure for the refinement process was taken from the literature[115]. The experimental diffraction peak profiles have been modeled using the Pseudo-Voigt peak shape function (profile function3) as employed in the GSAS+EXPGUI. The instrument parameter file was determined from the refinement of the standard CeO_2 diffraction pattern. GU, GV, GW, LX and LY are the profile shape parameters varied during the refinement. The fractional site occupancy of the RE atoms in the two different crystallographic sites were fixed to their concentration (ie, x) in the early stages of the refinement. In order to match the peak positions, the lattice parameter has been refined in the initial stage. Once all the peak positions of the diffraction pattern were well matched with the modeled peak positions, the peak shape parameters were released one by one in the order GW, LY, LX, GV and GU. After the peak shapes were modeled, the atomic positions and fractional site occupancy and the thermal parameters were refined independently by keeping all other parameters constant. As the heavy atoms contribute more to the diffraction intensity due to their higher scattering factor, the atomic positions of the heavy atoms (RE) were refined prior to the lighter atoms (Oxygen). The fractional site occupancy of RE atoms was refined by constraining the overall occupancy at a particular site to unity. The parameters of the modeled structure at the previous composition serve as the input to the following composition. Fig. 5.2 shows representative Rietveld fits to the experimental diffraction pattern of $x = 0, 0.2, 0.4, 0.6, 0.8$ and 1. The different agreement indices, R_{wp}, R_p and R_F(**2) which are shown in the Fig. 5.2 and the visual observations of the fits confirm the excellent quality of the refinement.

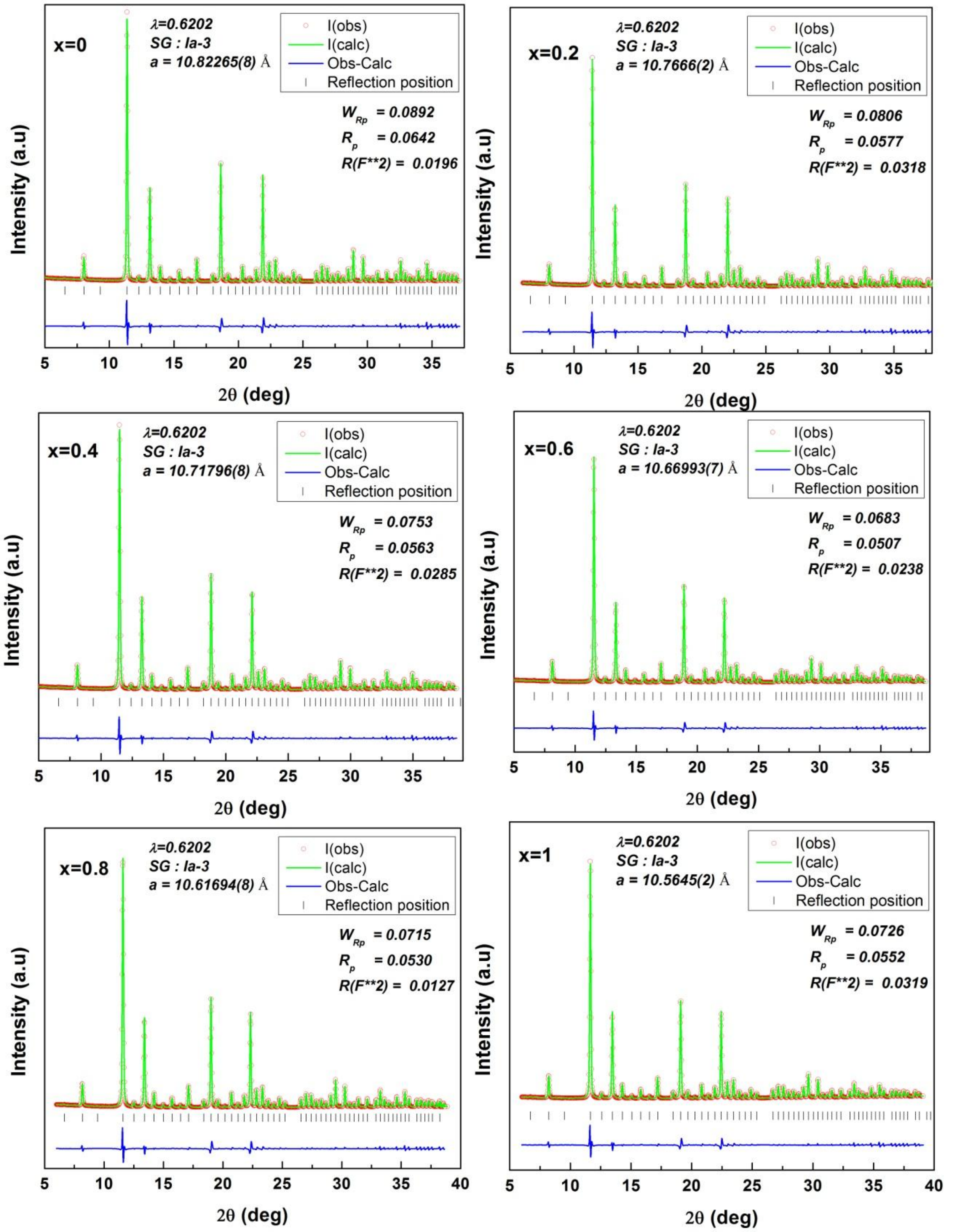

Fig. 5.2 Representative Rietveld refined XRD patterns of $(Eu_{1-x}Ho_x)_2O_3$. The lattice parameter and R factors are indicated in the respective plots.

Shannon *et al* have calculated the ionic radii of Eu^{3+} and Ho^{3+} as 0.950 Å and 0.894 Å respectively when the rare earths occupy octahedral co-ordination [116]. An average cationic radius, R_{RE}, has been calculated from the individual cationic radii of

Eu^{3+} and Ho^{3+} as $R_{RE} = xR_{Ho}+(1-x)R_{Eu}$ .The variation of the refined lattice parameter and the unit cell volume per formulae unit with composition, x, and R_{RE} is shown in Fig. 5.3a.

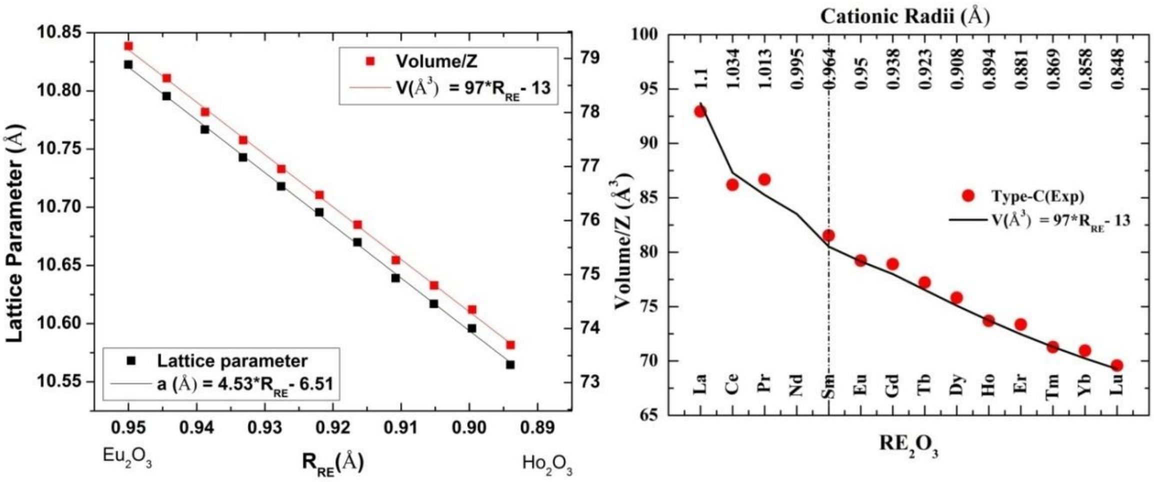

Fig. 5.3 a) Cation size dependence of unit cell parameter and unit cell volume/Z for the cubic $(Eu_{1-x}Ho_x)_2O_3$. Solid lines represent the linear fit to the experimental data and the respective equations are also shown. b) Comparison of the unit cell volume/Z of all the cubic RES reported in the literature with the estimated value from the empirical relation (see text) derived. A good agreement between the literature and the estimated value shows that this relation holds good for any solid solutions of RES in the Sm-Lu region.

It can be seen that the lattice parameter decreases linearly with increasing substitution of Ho_2O_3. This decrease in lattice parameter is a consequence of lanthanide contraction which is attributed to the comparatively poor shielding effect of the 4f electrons leading to a greater contraction in their ionic radii than expected. Due to the replacement of larger cation Eu by the smaller Ho, the cell volume decreases. Further, this linear behaviour indicates adherence to Vegard’s rule, which is an evidence for the complete miscibility of these substituted solid solutions. Variation in both volume and lattice parameters with respect to the R_{RE} can be best fitted to a straight line The linear fits to the experimental data follows the empirical relation $a(R_{RE}) = 4.53*R_{RE} - 6.51$ and $V(R_{RE}) = 97*R_{RE} -13$. Using this relation, the unit cell volume has been estimated for all the cubic RES by making use of their cationic radii from the literature[116]. In Fig. 5.3b, the unit cell volumes of the RES collected from the literature [95] and the estimated volumes according to the above relation have been shown together for comparison. It is seen that, the relation holds pretty good in the Sm-Lu region, where the cubic structure of RES is stable under ambient conditions. However, the relation does not hold in the region La-Sm, probably due to the instability of cubic structure in this region. Hence, this relation can be used to estimate the unit cell volume of those solid solutions of RES crystallizing in the cubic structure.

5.3.3. Evolution of local structure

The unit cell of the type-C structure is composed of 16 formula units with 32 cations distributed over two different crystallographic sites/Wyckoff positions. All cations are in six-fold coordination and occupy special octahedral positions 24d with C_2 site symmetry and 8b with C_{3i} site symmetry and the oxygen ions are in general positions 48e. The octahedral arrangement of the two RE ion sites with respect to the crystallographic unit cell axes are shown in Fig. 5.4a.

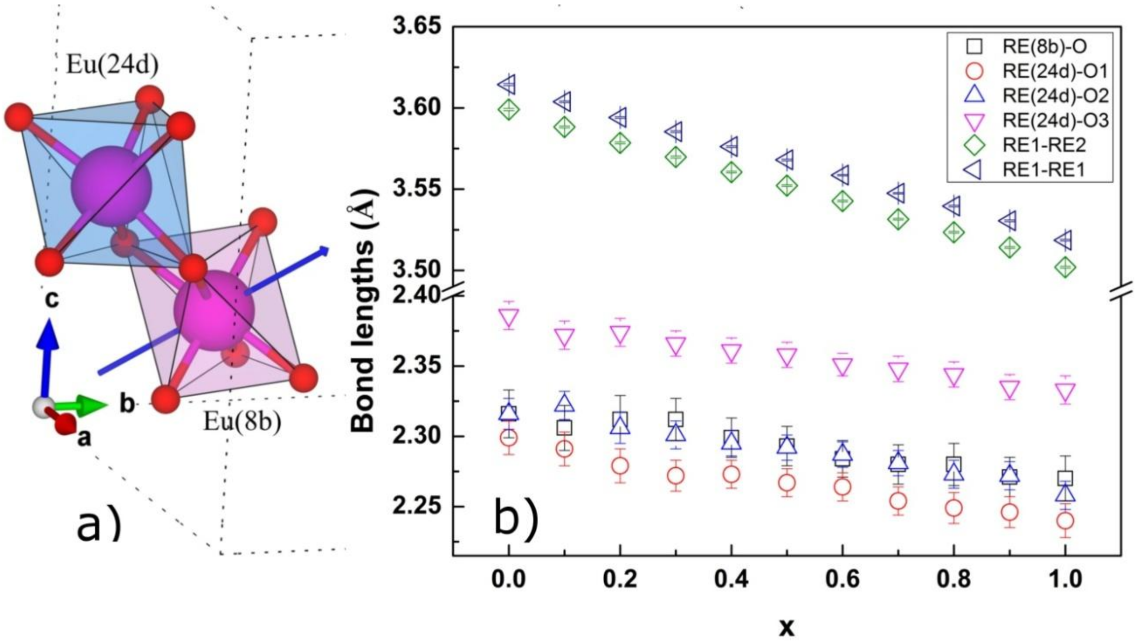

Fig. 5.4 a) The two different kinds of octahedral arrangements around the two cation sites 8*b* and 24*d* with respect to the crystallographic axes. b) Variation of all the octahedral bond lengths along with the two RE-RE bonds. Refer text for the different legends used.

The octahedron with the 8b site is characterized by a single bond length whereas the octahedron with 24d site is made up of three different bond lengths. The variation of RE-O bond length of the RE(8b)O_6 octahedron and the three different RE-O bond lengths (designated as RE(24d)-O1, RE(24d)-O2 and RE(24d)-O3) of the RE(24d)O_6 octahedron with respect to composition are given in the Fig. 5.4b. It indicates that all RE-O bonds show a systematic decrease with composition, *x*. Similar behavior is observed for the changes in the bond length between the two rare earth cation sites and between the same equivalent sites. This systematic decrease in bond lengths is due to the decreasing value of the cationic radii with the increasing composition, *x*.

Refined values of atomic positions along with their site occupancy and the two octahedral volumes are tabulated in Table 5.2. The fractional atomic co-ordinate of the rare earth cation at 24*d* shows a systematic change with composition whereas the oxygen positions are found to be unaffected by these substitutions. The replacement of the lighter Eu atom by the heavier Ho atom leads to a systematic decrease in the cation position at 24*d* site. An identical behavior is observed in $(Er_{1-x}Gd_x)_2O_3$ [117]. To figure out the site preference of the two RE cations, the fractional site occupancy of RE atoms were refined by constraining the overall occupancy at a particular site to unity. Site occupancy of the oxygen atom was not refined and kept as 1. From the individual fractional site occupancy values, the coefficient of cationic distribution, *K*, is calculated as:

$$K = \frac{O_{Eu}(8b)}{O_{Ho}(8b)} \frac{O_{Ho}(24d)}{O_{Eu}(24d)}$$

where, $O_{Eu}(8b)/(24d)$ and $O_{Ho}(8b)/(24d)$ are the fractional site occupancies of Eu^{3+} and Ho^{3+} atoms at 8*b* and 24*d* positions respectively [118]. If *K* is equal to or close to 1, a random cationic distribution is present. The refined values of the occupancy parameter for the Eu atom in the two cation sites and the calculated values of *K* are tabulated in Table 5.2.

Table 5.2 The refined values of fractional atomic co-ordinates, coefficient of cationic distribution (K) and the two octahedral volumes for all the solid solutions along with the parent RES. The octahedral volumes were taken from VESTA [119]. The values in the parenthesis are the error in the last decimal places.

x	**Fractional atomic co-ordinates**				**Site Occupancy**		***K***	**Octahedral volume(Å^3)**	
	RE(24*d*)	**O(x/a)**	**O(y/b)**	**O(z/c)**	**Eu(24*d*)**	**Eu(8*b*)**		**P(24*d*)**	**P(8*b*)**
0	0.96929(9)	0.389(1)	0.151(1)	0.378(1)	1.000(3)	0.997(6)	--	15.157	15.548
0.1	0.96905(9)	0.388(1)	0.1516(9)	0.379(1)	0.89(3)	0.92(7)	1.22931	15.057	15.375
0.2	0.96902(9)	0.390(1)	0.151(1)	0.379(1)	0.80(3)	0.79(7)	1.04397	14.919	15.515
0.3	0.96891(8)	0.390(1)	0.1510(9)	0.379(1)	0.69(3)	0.72(7)	0.98588	14.793	15.503
0.4	0.96876(8)	0.3898(9)	0.1513(8)	0.379(1)	0.59(3)	0.62(7)	0.92773	14.725	15.243
0.5	0.96864(7)	0.3898(9)	0.1516(8)	0.379(1)	0.50(3)	0.51(6)	1.01207	14.658	15.138
0.6	0.96850(7)	0.3896(9)	0.1517(8)	0.379(1)	0.40(2)	0.39(6)	1.09691	14.562	14.975
0.7	0.96837(7)	0.3901(9)	0.1520(8)	0.379(1)	0.30(3)	0.30(7)	1.0908	14.453	14.924
0.8	0.96828(8)	0.390(1)	0.1518(9)	0.379(1)	0.20(3)	0.21(7)	0.96292	14.351	14.905
0.9	0.96792(8)	0.390(1)	0.1521(9)	0.379(1)	0.09(3)	0.12(7)	1.47001	14.283	14.760
1	0.96768(8)	0.390(1)	0.1519(10)	0.379(1)	0	0	--	14.153	14.729

It can be clearly seen that, the values of *K* is near to 1 for all the doped sesquioxides. There was no evidence for the preferential site occupancy in the two cation sites 24*d* and 8*b*. It clearly points to the fact that a random distribution of the cations is preferred in the two octahedral sites over the whole range of composition. Earlier reports show that, site preference of RE cations in mixed rare earth sesquioxides has dependence on the difference in cationic radii, R_d. Lesser the R_d, higher the probability towards random cationic distribution[118, 120]. Since Eu^{3+} and Ho^{3+} are close enough in periodic table, their solid solutions will have lower R_d compared to the Eu-Yb system [118]. Hence a random distribution is favored in this case. Similar studies on the mixed rare earth sesquioxides $(Er_{1-x}Gd_x)_2O_3$[117], $(Gd_{1-x}Ho_x)_2O_3$[121], $Re_xY_{2-x}O_3$ (Re=Dy, Ho, Er) [122], $Sm_xY_{2-x}O_3$[123] and $(Y, Eu)_2O_3$[124] showed a random distribution of the cations at the two sites, whereas a preferential site occupancy over a certain range of doping is confirmed in some of the mixed rare earth sesquioxides $(Gd_{1-x}Yb_x)_2O_3$, $(Dy_{1-x}Er_x)_2O_3$ and $Yb_xY_{2-x}O_3$[121, 125, 126]. Furthermore, the method of sample preparation, difference in cationic radii and the parameters of the synthesis procedure have a major role in deciding the site preference [125].

5.3.4. Raman spectroscopic studies

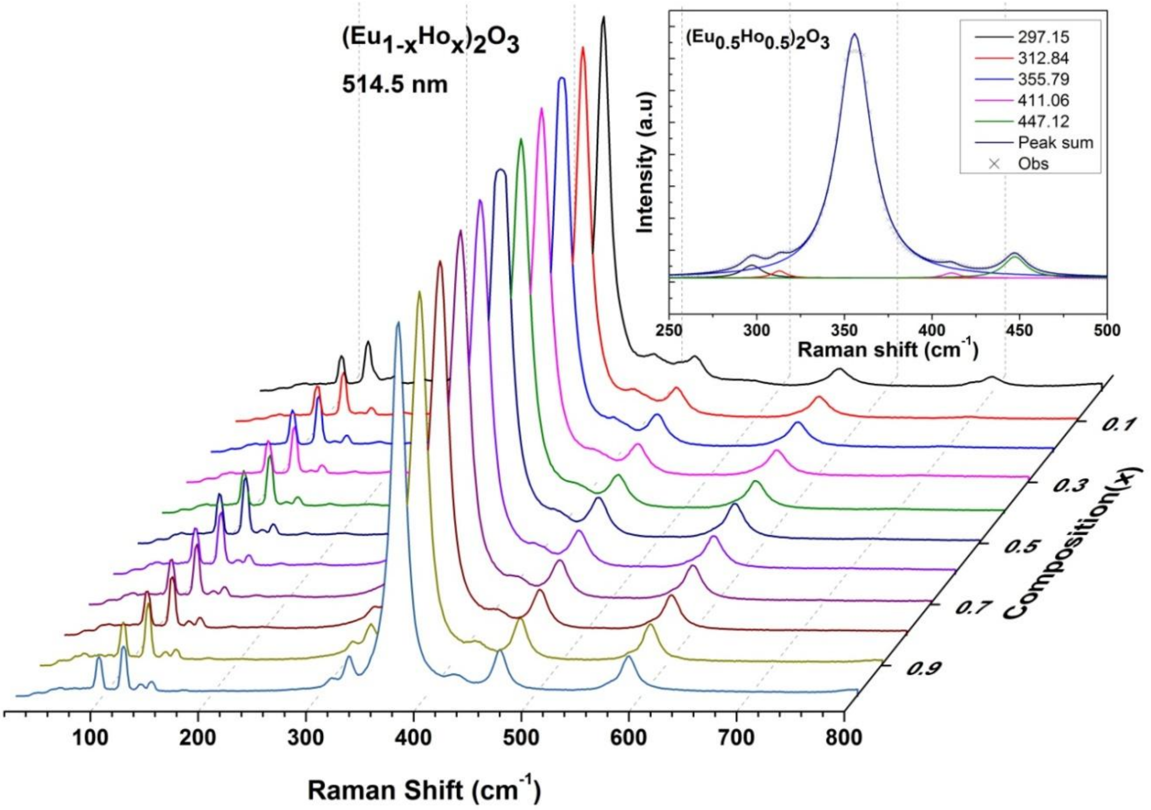

Fig. 5.5 Normalized Raman spectra of $(Eu_{1-x}Ho_x)_2O_3$ in the range $0.0 \leq x \leq 1.0$ at a laser excitation wave length of 514.4 nm with a collection time of 10 sec. The inset figure shows the Lorentzian fit to the partially overlapped peaks for $x = 0.5$

Raman spectra of $(Eu_{1-x}Ho_x)_2O_3$ in the range 80-800 cm^{-1} is given in Fig. 5.5. The most intense vibrational mode was observed between 338 and 375 $cm^{-1}$for all compositions. Factor group analysis for RE_2O_3 compounds with SG *Ia-3* predicted a total of 22 Raman active modes, $4A_g+4E_g+14T_g$ [104]. However, only 13 Raman bands were observed in our experiment, possibly due to accidental degeneracy or insufficient intensities due to the small polarizability of some of the vibrations. Some asymmetric bands (such as 557 cm^{-1}, 338 cm^{-1}, 285 cm^{-1} etc.) could be resolved into their components by fitting to Lorentzian peak functions. Table 5.3 represents the wave numbers corresponding to the observed Raman lines and the assigned symmetry of modes of vibration for all compositions. Modes are assigned by comparing with the existing literature[101, 127]. The main band is assigned to F_g and it corresponds to an RE-O stretching mode [128].

Table 5.3 The observed Raman modes for all the compositions along with the lattice parameter. The symmetry modes are assigned using the modes of different RES reported in the literature. All mode frequencies are in cm^{-1}

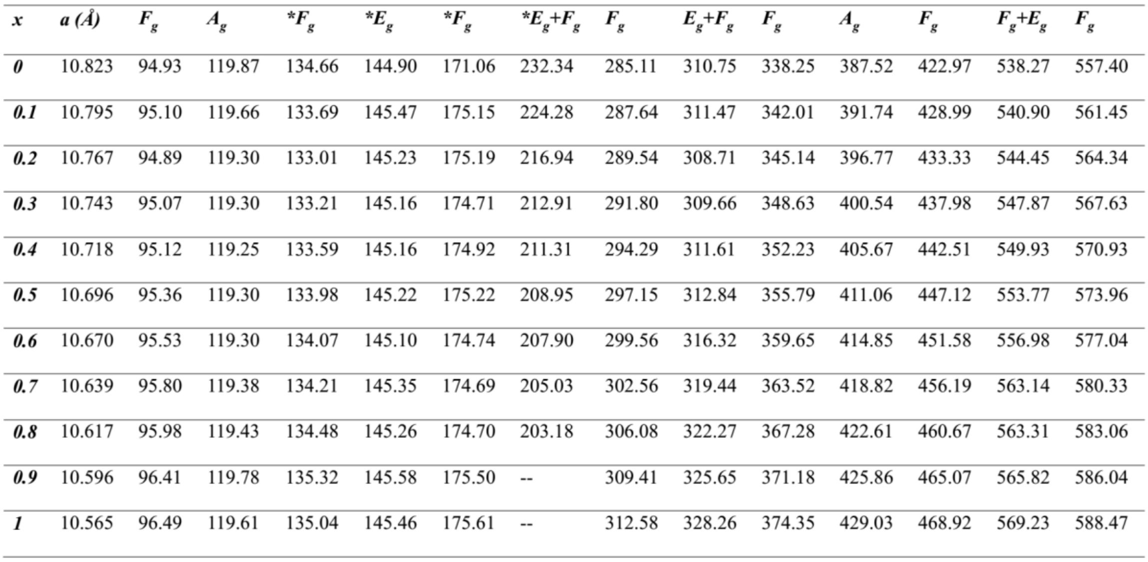

x	*a* (Å)	F_g	A_g	*F_g	*E_g	*F_g	*E_g+F_g	F_g	E_g+F_g	F_g	A_g	F_g	F_g+E_g	F_g
0	10.823	94.93	119.87	134.66	144.90	171.06	232.34	285.11	310.75	338.25	387.52	422.97	538.27	557.40
0.1	10.795	95.10	119.66	133.69	145.47	175.15	224.28	287.64	311.47	342.01	391.74	428.99	540.90	561.45
0.2	10.767	94.89	119.30	133.01	145.23	175.19	216.94	289.54	308.71	345.14	396.77	433.33	544.45	564.34
0.3	10.743	95.07	119.30	133.21	145.16	174.71	212.91	291.80	309.66	348.63	400.54	437.98	547.87	567.63
0.4	10.718	95.12	119.25	133.59	145.16	174.92	211.31	294.29	311.61	352.23	405.67	442.51	549.93	570.93
0.5	10.696	95.36	119.30	133.98	145.22	175.22	208.95	297.15	312.84	355.79	411.06	447.12	553.77	573.96
0.6	10.670	95.53	119.30	134.07	145.10	174.74	207.90	299.56	316.32	359.65	414.85	451.58	556.98	577.04
0.7	10.639	95.80	119.38	134.21	145.35	174.69	205.03	302.56	319.44	363.52	418.82	456.19	563.14	580.33
0.8	10.617	95.98	119.43	134.48	145.26	174.70	203.18	306.08	322.27	367.28	422.61	460.67	563.31	583.06
0.9	10.596	96.41	119.78	135.32	145.58	175.50	--	309.41	325.65	371.18	425.86	465.07	565.82	586.04
1	10.565	96.49	119.61	135.04	145.46	175.61	--	312.58	328.26	374.35	429.03	468.92	569.23	588.47

Recent lattice dynamics calculations of isostructural Sc_2O_3 single crystal have concluded that all low frequency modes (below 300 cm^{-1}) predominantly arise from the vibrations of rare earth cations and the one above this originate from almost pure oxygen vibrations [102]. The dependence of Raman lines on R_{RE} and the lattice constants for the high frequency region are given in the Fig. 5.6a. A systematic increase in the Raman shift with the R_{RE} is observed in this region. The mode frequency is roughly proportional to the square root of the force constant (the measure of the strength of a chemical bond) and inversely proportional to the square root of the reduced mass. The increasing frequency indicates that as the Ho content increases the RE-O bond becomes more and more strong and the structure becomes rigid. As the low frequency modes are mainly due to the stretching vibrations, they are highly sensitive to the change in force constant[120], when the mass difference between cations are less. Fig. 5.6b shows the Raman bands below 300 cm^{-1} where all, except the one around 232 cm^{-1}, remain almost constant for all compositions. This may be due to the competing effects of the increasing mass of the RE ion and the decreasing lattice parameter with an increasing *x* [101]. As the low wave number modes are due to the bending vibrations, they are less sensitive to the variations in force constant[120]. So, mass variation is responsible for the shift in this frequency range. Since Ho and Eu occupy close positions in the periodic table, their difference in mass is too small to make an appreciable change in the Raman shift.

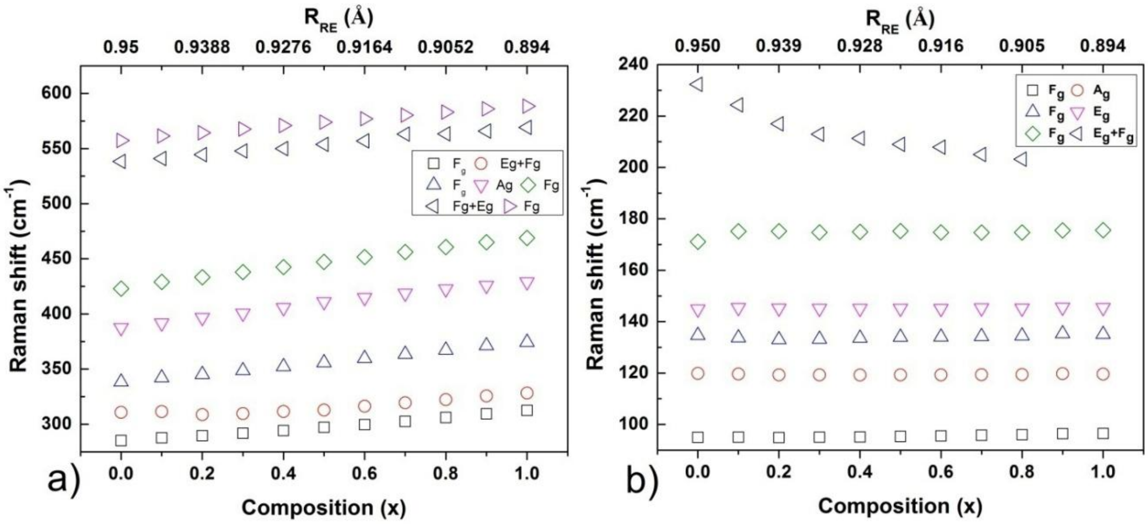

Fig. 5.6 The dependence of x/R_{RE} on the Raman shift a) for the high frequency region (>300cm^{-1}) b) for the low frequency region (<300cm^{-1}). An increase in the Raman shift with the decrease in ionic radii can be clearly seen in the high frequency region. The legends indicate the different symmetry modes assigned using the literature[101, 127].

Further, the weak band around 232 cm^{-1} shows an unusual softening behavior with increasing Ho content and disappears for $x > 0.8$. It has been reported that the low frequency regions are dominated by translational movements of RE ions and vibrational modes of REO$_6$ octahedra[129, 130]. In Fig. 5.7, the change in RE positional coordinate and the softening behavior of the mode at 232 cm^{-1} are shown together for clarity, which indicates that the mode disappears exactly where a sharp change in the slope of x(RE-24*d*) vs. x is seen. It is also seen (from Fig. 5.7) that there exists two regimes: in the region $0.8 \leq x \leq 1$, the 232 cm^{-1} mode does not appear, and there is also a larger slope in x(RE-24*d*) as compared to the other region. This prompts the speculation that for $0.8 \leq x \leq 1$, the Eu atom is sufficiently displaced away to weaken the electrostatic interaction responsible for this mode. For $0 \leq x \leq 0.8$ the 232 cm^{-1} mode becomes increasingly harder, signifying larger contribution of Eu ion to the interaction.

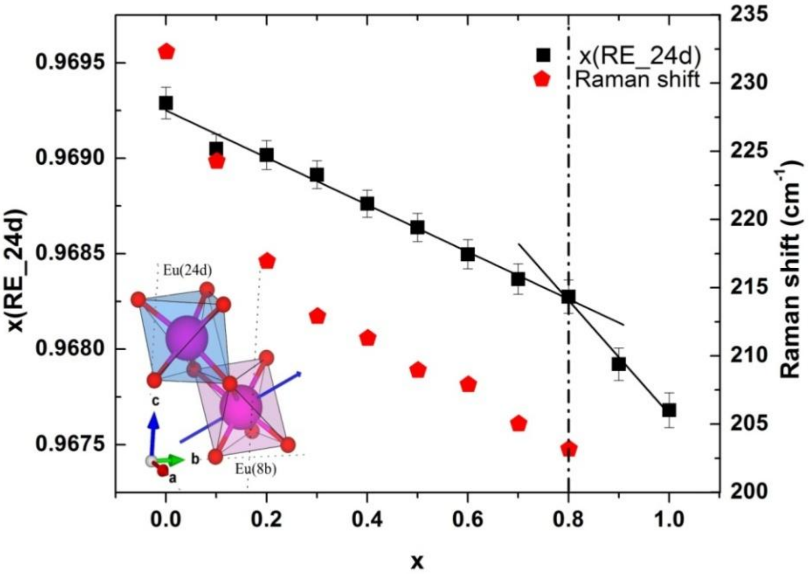

Fig. 5.7 Change in fractional co-ordinate, x, of the RE ion occupying the 24*d* (C$_2$ symmetry) site and the Raman mode around 232 cm^{-1}. The two octahedral arrangements in the unit cell are shown in the inset. The solid lines represent the linear fit to the experimental data showing the distinct slope changes.

5.4. Polymorphic phase transitions in $(Eu_{1-x}Ho_x)_2O_3$ at high pressures

The following sections will contain the results and conclusions drawn from the high pressure synchrotron X-ray diffraction studies.

5.4.1. Identification of phase transitions from high pressure X-ray diffraction

Angle dispersive X-ray diffraction patterns (ADXRD) of $(Eu_{1-x}Ho_x)_2O_3$ [x = 0, 0.2, 0.4, 0.5, 0.6, 0.8, 1] recorded at various pressures are shown in Fig. 5.8 and Fig. 5.9 e-g. It is clear from the diffraction data that the onset of phase transition in all of these mixed oxides are characterized with the origin of a new peak near the parent cubic *123* peak. For x = 0 (Fig. 5.8a), Eu_2O_3, the diffraction pattern does not show any signature of structural phase transition till 5.7 GPa. At 5.7 GPa the emergence of a new peak near the cubic *123* peak indicates the onset of structural phase transition. The high pressure phase could be indexed to the hexagonal phase with space group *P-3m1* [4]. The parent phase co-exists up to 12.9 GPa. The transition pressure, structure of the high pressure phase and the coexisting regime are in agreement with the reported high pressure studies on pristine Eu_2O_3 [4]. For x = 0.2-0.5 (Fig. 5.8b-d), the nucleation of the hexagonal phase (as identified), has been indicated by the emergence of two new peaks near the cubic *123* and *222* peaks. The transition pressures for x = 0.2, 0.4 and 0.5 are 6.7, 7.8 and 7.4 GPa respectively. From detailed analysis, it is also evident that the coexistence regime of cubic and hexagonal phases for x = 0.2, 0.4 and 0.5 are 15.8, 17 and 18.3 GPa respectively.

Unlike mixed oxides with x = 0.2 to 0.5, the one with x = 0.6 shows a very different behavior as a function of pressure. The cubic phase remains stable up to 7.2 GPa and thereafter the transformation to the hexagonal phase is incomplete even at 26 GPa. Despite the presence of a broad monoclinic peak (marked with an asterisk in the Fig. 5.9e)[39], the diffraction data between 19.1-26 GPa could be fitted to the hexagonal structure. In the region 7.2-14.4 GPa, the compression behavior is found to be different from the high pressure region (19.1 to 26 GPa) if fitted to hexagonal phase pointing out to the existence of an anomalous regime. However, the monoclinic phase could not be quantified due to the insufficient number of well resolved peaks.

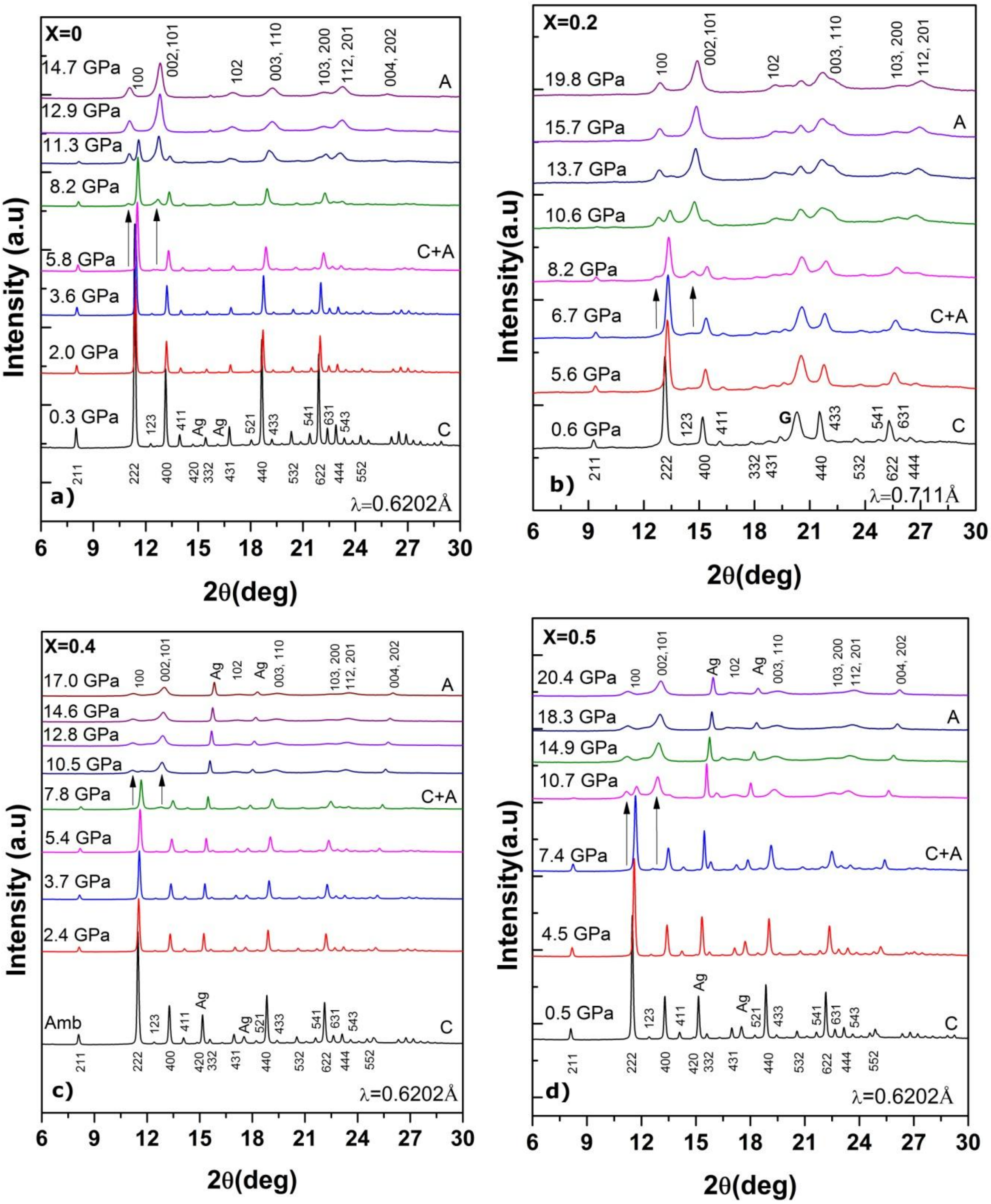

Fig. 5.8 a-d) High pressure X-ray diffraction pattern of $(Eu_{1-x}Ho_x)_2O_3$ [x = 0, 0.2, 0.4, 0.5] at various pressures. The onset of phase transitions is indicated by up arrows. G and Ag stands for the peaks corresponding to the gasket and the silver pressure calibrant respectively. C and A represent the cubic and hexagonal phase respectively.

For $x = 0.8$(Fig. 5.9f) and at 9.1 GPa, the emergence of a new peak near the cubic *123* peak indicates the onset of a phase transition. The diffraction pattern at 13.4 GPa could be indexed to the monoclinic phase (*C2/m*), indicating the C→B nature of phase transition in this oxide. Further, at 16.6 GPa the multiphase Rietveld refinement of the diffraction data indicate the appearance of the new hexagonal structure coexisting with the cubic and monoclinic phase. Fig. 5.10, Fig. 5.11 and Fig. 5.12 shows representative Rietveld fits to the diffraction data at various pressures for $0 \leq x \leq 1$. The unit cell parameters for the cubic, monoclinic and the hexagonal phases along with the different R factors are depicted in the figure. For x= 0.8, all the three phases co-exist up to the highest experimental pressure (20.3 GPa). As reported in the literature[39, 40], the high pressure experiment on cubic Ho_2O_3, i.e., $x = 1$ (Fig. 5.9g), showed a structural transition to the monoclinic phase at 8.8 GPa followed by a complete transition at 16.4 GPa. A B→A transition in Ho_2O_3 was also reported at 14.8 GPa and the hexagonal phase fraction wa predominant at around 26 GPa[39]. However, this transition was not observed till the highest pressure attained in this experiment (16.4 GPa). X-ray diffraction patterns of all the mixed oxides in the range of d spacing 2.5- 3.5 Å, where the onset of phase transition is clearly visible has been shown in Fig. 5.9h. Apart from the origin of a new peak near the cubic *123* peak observed in all the cases, the onset of C→A transition is characterised with the origin of another peak on the left of the *222* peak of the cubic phase. On the other hand this feature is absent in the C→B phase transitions. Hence this feature can be used to distinguish the C→A and C→B phase transitions in these oxides at the early stages of their transitions.

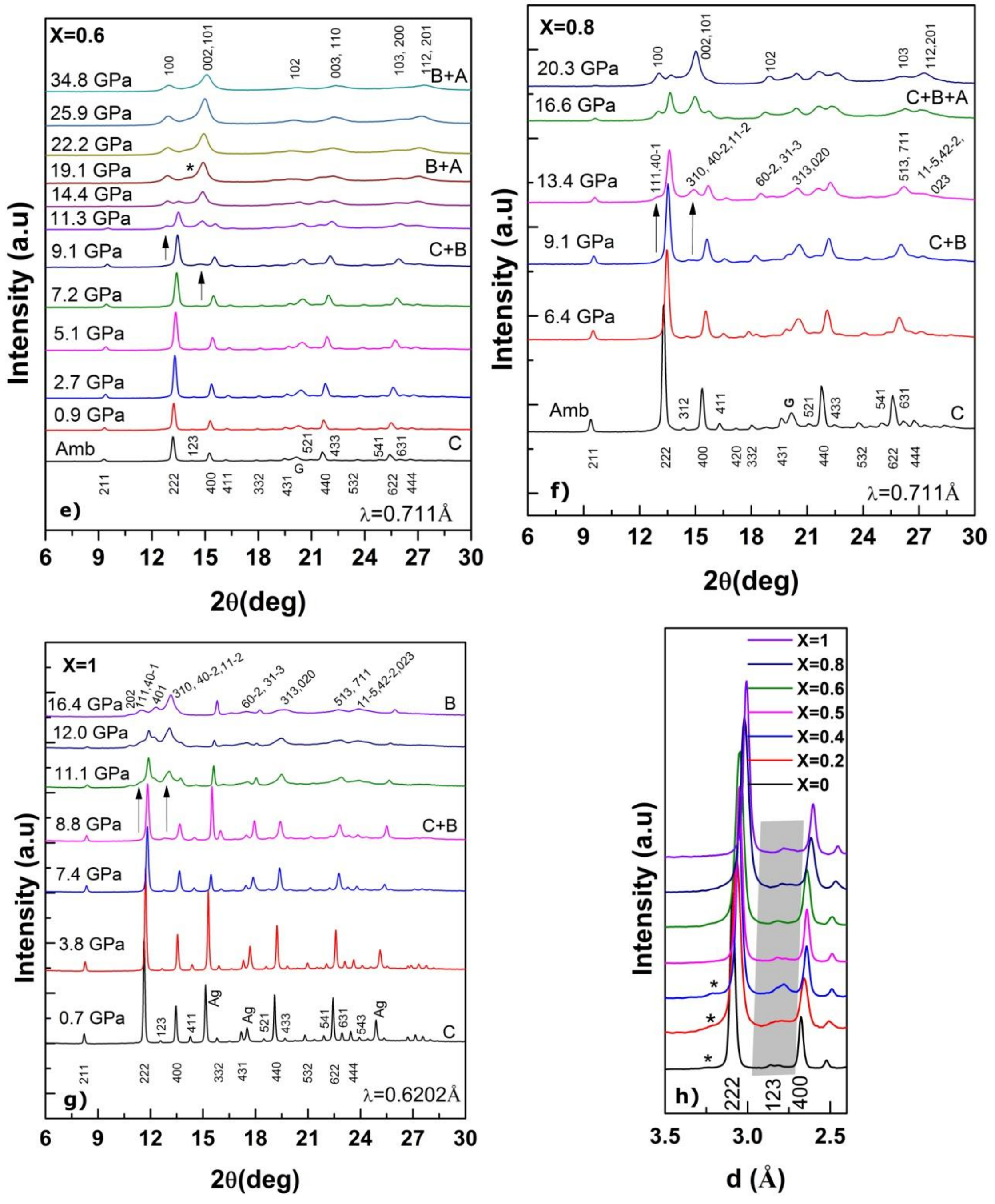

Fig. 5.9 e-g) High pressure X-ray diffraction pattern of $(Eu_{1-x}Ho_x)_2O_3$ [x = 0.6, 0.8 and 1] at various pressures. The onset of phase transitions is indicated by up arrows. G and Ag stands for the peaks corresponding to the gasket and the silver pressure calibrant respectively. C, B and A represents the cubic, monoclinic and hexagonal phase respectively. The * mark in the diffractogram for x=0.6 shows the *401* peak corresponding to the monoclinic structure. h) Diffraction patterns collected at the phase transition pressure. Shaded region shows common signature of C→A and C→B, whereas * marks indicate the feature of C→A transition alone.

It is evident from the high pressure X-ray diffraction data of $(Eu_{1-x}Ho_x)_2O_3$ that, pressure induced structural phase transitions in these oxides strictly depend on x. For $x \leq$

0.5, a C→A transition is favored while for $x \geq 0.6$ C→B is the preferred transition sequence. In general, the transition sequence of these lanthanide sesquioxides are believed to be dependent on the cationic radii [2]. C→A transition for Eu$_2$O$_3$, a medium sized cationic radii, is reported at 5 GPa and the C→B transition in Ho$_2$O$_3$, small sized cationic radii, is reported at 8.9-9.5 GPa [4, 39, 40]. As expected, the transition pressure for all these solid solutions are found to be in between the reported transition pressure for the parent oxides.

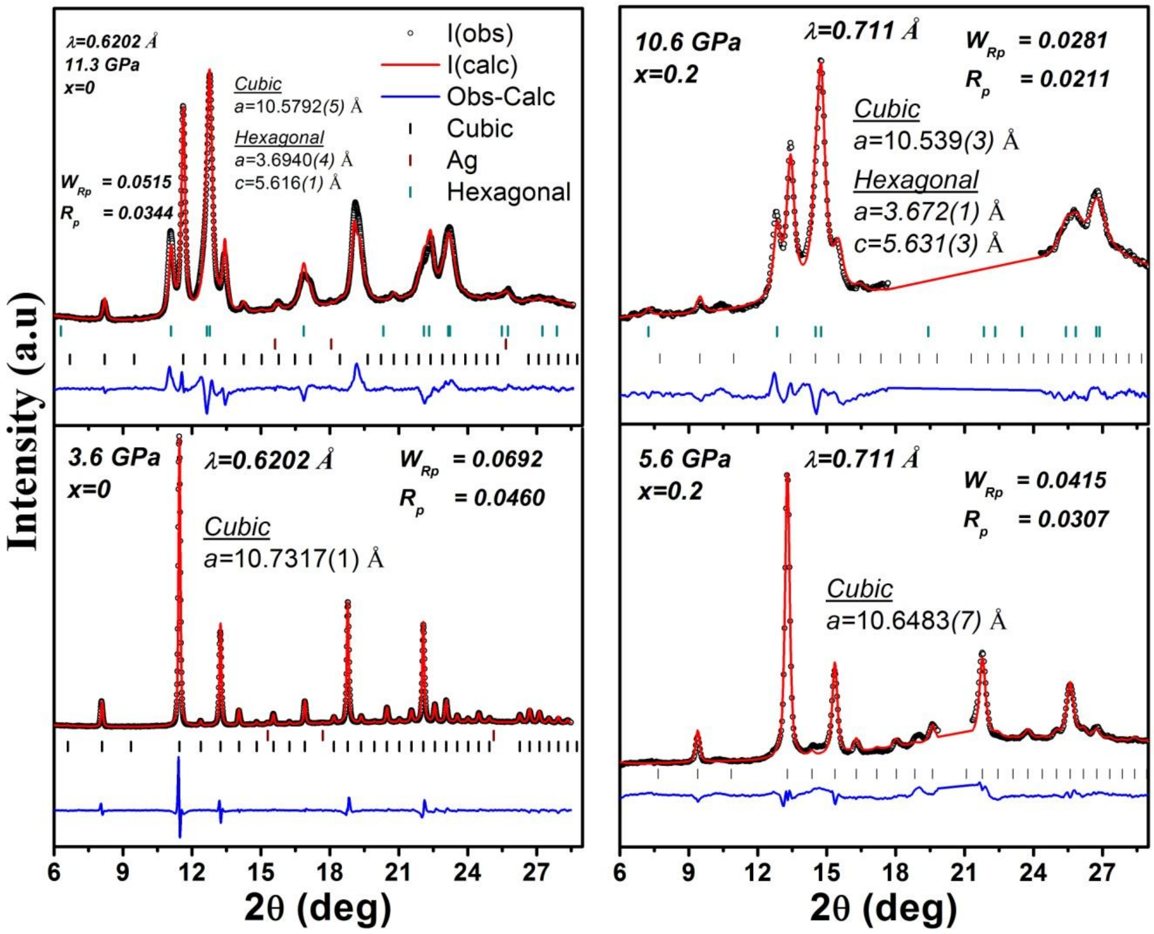

Fig. 5.10 Rietveld fit of high pressure X-ray diffraction data for x=0 at 3.6 & 11.3 GPa (left panel) and for x=0.2 at 5.6 & 10.6 GPa (right panel). The corresponding unit cell parameters and the agreement indices are shown in the respective figures. The masked region in the diffraction pattern was excluded from the refinement due to the overlapping of broad gasket peak with the sample peaks.

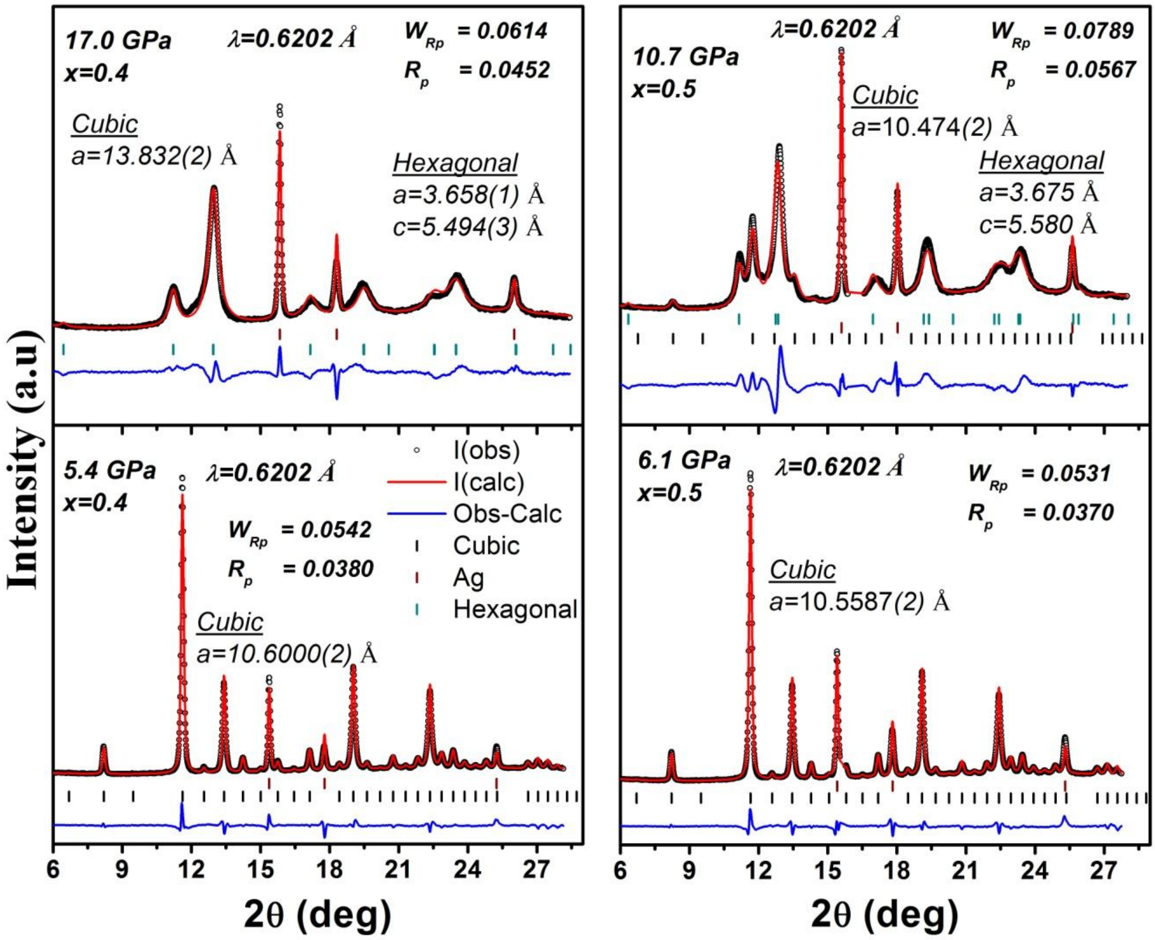

Fig. 5.11 Rietveld fit of high pressure X-ray diffraction data for *x*=0.4 at 5.4 & 17 GPa (left panel) and for *x*=0.5 at 6.1 & 10.7 GPa (right panel). The corresponding unit cell parameters and the agreement indices are shown in the respective figures. The masked region in the diffraction pattern was excluded from the refinement due to the overlapping of broad gasket peak with the sample peaks.

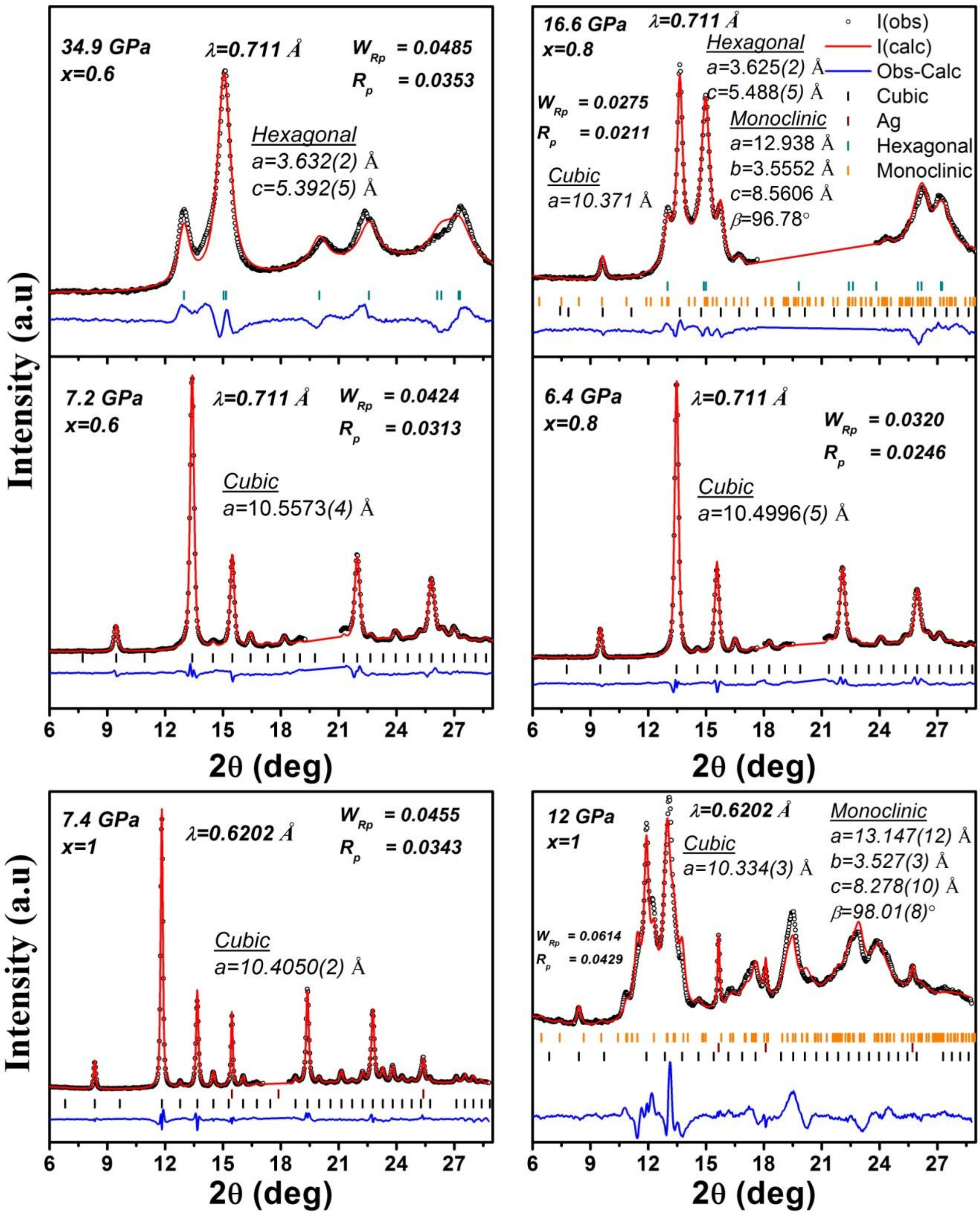

Fig. 5.12 Rietveld fit of high pressure X-ray diffraction data for *x*=0.6 at 7.2 & 34.9 GPa (top left panel), for *x*=0.8 at 6.4 & 16.6 GPa (top right panel) and for *x*=1 at 7.4 & 12 GPa (bottom left & right panel). The corresponding unit cell parameters and the agreement indices are shown in the respective figures. The masked region in the diffraction pattern was excluded from the refinement due to the overlapping of broad gasket peak with the sample peaks.

5.4.2. Unit cell compressibility and equation of states

The pressure dependence of the unit cell volume of all these mixed oxides is shown in Fig. 5.13. The bulk moduli of the parent cubic and the high pressure hexagonal/monoclinic structures of all these mixed oxides were obtained by fitting the experimental data to the Birch-Murnaghan EOS (see 2.4.3)keeping the $B_0' = 4$[131]. The obtained bulk moduli for the ambient and high pressure phases, corresponding reduction in unit cell volume and the transition pressure for these oxides are listed in Table 5.4. These different bulk moduli values indicate that the high pressure phases of the mixed oxides are less compressible than the ambient phase. For a comparative purpose the reported bulk moduli of Eu_2O_3 [4] and Ho_2O_3 [39, 40] are also listed. It is clear that, the current experiment on Ho_2O_3 yields a bulk modulus much less compared to the available reports, whereas for Eu_2O_3 it is in good agreement with the literature. For comparative purpose, all the compressibility curves of C→A and C→B transitions are shown in Fig. 5.14 respectively. The relation $R_{RE} = xR_{Ho}+(1-x)R_{Eu}$ has been used to study the effect of cationic radii on the EOS derived parameters. Fig. 5.15 represents the variation in the cubic bulk modulus, transition pressure and the volume reduction from cubic phase to the respective high pressure phases for all the solid solutions as a function of x/R_{RE}. Even though a general increasing trend is reported for the bulk modulus with decreasing cationic radii, it is not true in the case of these solid solutions. The bulk modulus is found to be minimum for $x = 0.4$ and maximum for $x = 0.8$. Moreover, the observed transition pressure does not show an increasing trend with the decreasing cationic radii, which is in disagreement with the literature reports[2]. Transition pressure was observed to be increasing for $x = 0\text{-}0.4$ and a region of plateau, with a slight decreasing trend, was observed for $x = 0.4\text{-}0.6$. This rise in transition pressure in the region $x = 0\text{-}0.4$ could be due to the increased structural rigidity resulting from the increase in the RE-O bond strength as described in section 5.3.4.

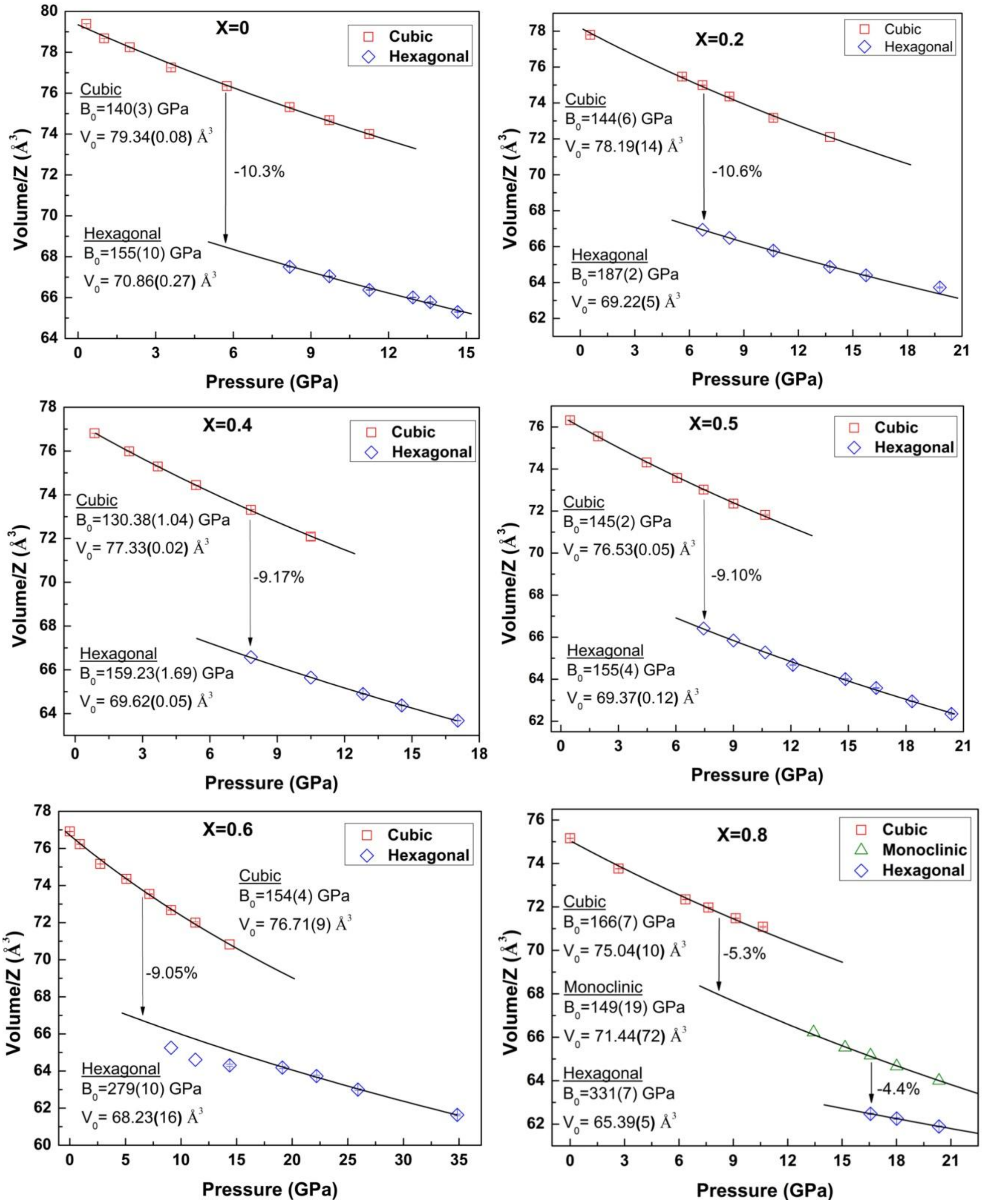

Fig. 5.13 The experimental pressure volume (P-V) data for all the investigated oxides. The solid lines indicate the Birch-Murnaghan equation of state fit to the P-V data. The fitting parameters and the volume drop at the transition pressure are quoted.

The atypical behavior of bulk modulus and the transition pressure in the region *x* = 0.4 - 0.6 from their usual behavior in the RES can be addressed by the doping induced internal strain (micro strain). The Rietveld refined Ly parameter has been used to deduce the microstrain present in all the solid solutions at ambient conditions[94]. From the Ly parameters, the micro strain for all the solid solutions has been calculated relative to that present in the parent Eu_2O_3. Table 5.5 lists out the refined Ly parameters and the associated micro strain calculations. Inset of Fig. 5.15 shows the variation of micro strain, $\varepsilon_{r,}$ in the parent cubic structure relative to the end member as a function of Ho_2O_3 doping. It is evident that the strain follows a non monotonous behavior with doping and is maximum for $x = 0.4 - 0.6$. This indicates that larger the difference in cationic radii the more is the strain in the lattice. A similar kind of strain behavior is observed in the solid solutions of other mixed RES, where the micro strain varies anisotropically with the cationic radii[118, 121]. This manifests as an internal pressure in the crystal structure and results in the reduction of structural stability which in turn leads to the observed reduction in the transition pressure in this region. Further, the reduction in the structural stability leads to the increase in the compressibility, hence a lower bulk modulus, for $x = 0.4$. Similar reduction in transition pressures are reported for mixed oxides of Gd_2O_3- Er_2O_3 and Y_2O_3- Eu_2O_3 [28, 132]. Another fact is that, the volume reduction for $x \leq 0.5$ across the phase transition pressure is found to vary within 9.1 - 10.3%, which falls on the typical limits of volume reduction in C→A transition in RES[3-5]. Contrary to the other RES, a discernable volume reduction has been observed in the case of $x = 0.8$, which undergoes a C→B→A transition. The C→B transition was characterized by 5.3% unit cell volume reduction where as it is 4.4% for B→A transition. Typically, in RESs, the volume reduction for a C→B transition is ~7-8 % and for a B→A is ~1-2 % [38, 39]. This indicates that, a C→B transition becomes possible in this mixed oxide with a comparatively lower reduction in unit cell volume.

Table 5.4 Bulk moduli, transition pressure and volume reduction for all the mixed oxides along with the reported values of the end members. Transition pressure and volume reduction from B→A is separated by a /(slash) in respective columns.

x	**B_0(C) GPa**	**B_0(B) GPa**	**B_0(A) GPa**	**P_t GPa**	**V_{red} (%)**
0	140(3)		155(10)	5.8	10.3
	145(2)		151(6)	5	9[4]
0.2	144(6)		187(2)	6.7	10.6
0.4	130(1)		159(2)	7.8	9.2
0.5	145(2)		155(4)	7.4	9.1
0.6	154(4)	-	279(10)	7.2	9.1
0.8	166(7)	149(19)	331(7)	9.1/16.6	5.3/4.4
1	155(3)	249(33)	-	8.8	8.6
	206(3)	200(7)	204(19)	8.9/16.3	8.1/2.5[39]

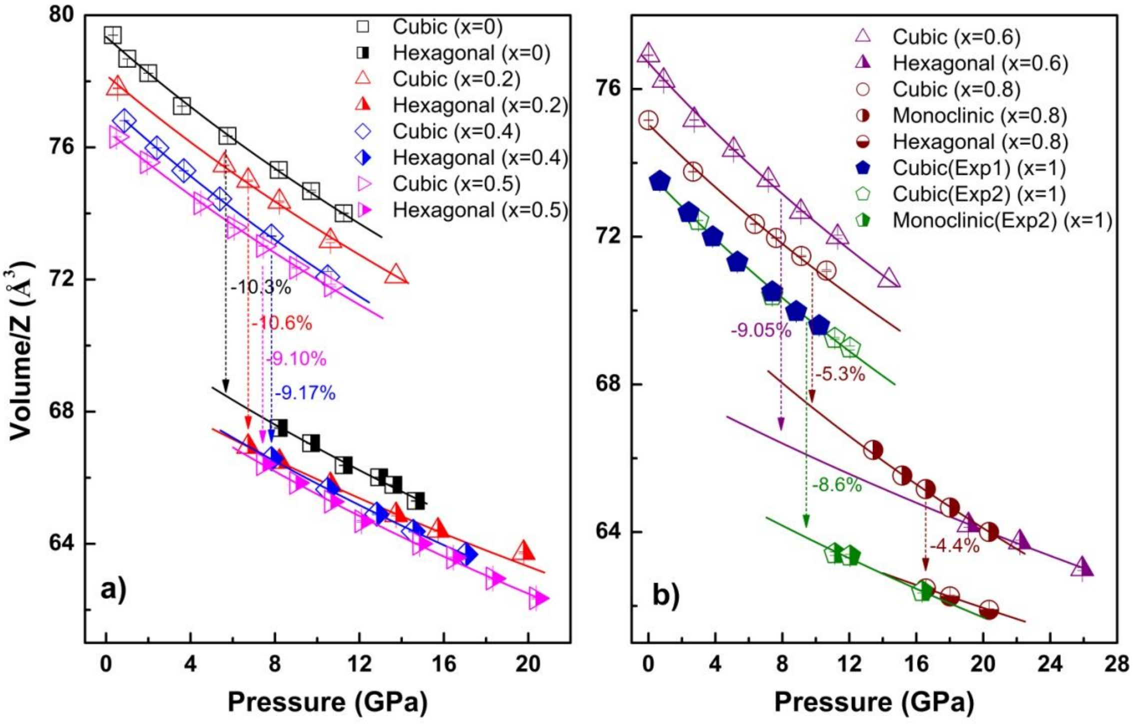

Fig. 5.14 A comparative representation of pressure-volume curves for all the mixed oxides a) with C→A transition b) with C→B transition. The volume drop across the transitions is marked. The solid lines indicate the Birch-Murnaghan EOS fit to the pressure volume data. In the case of pure Ho_2O_3 (*x* = 1), two experiments were done which are marked as Exp1 and Exp2.

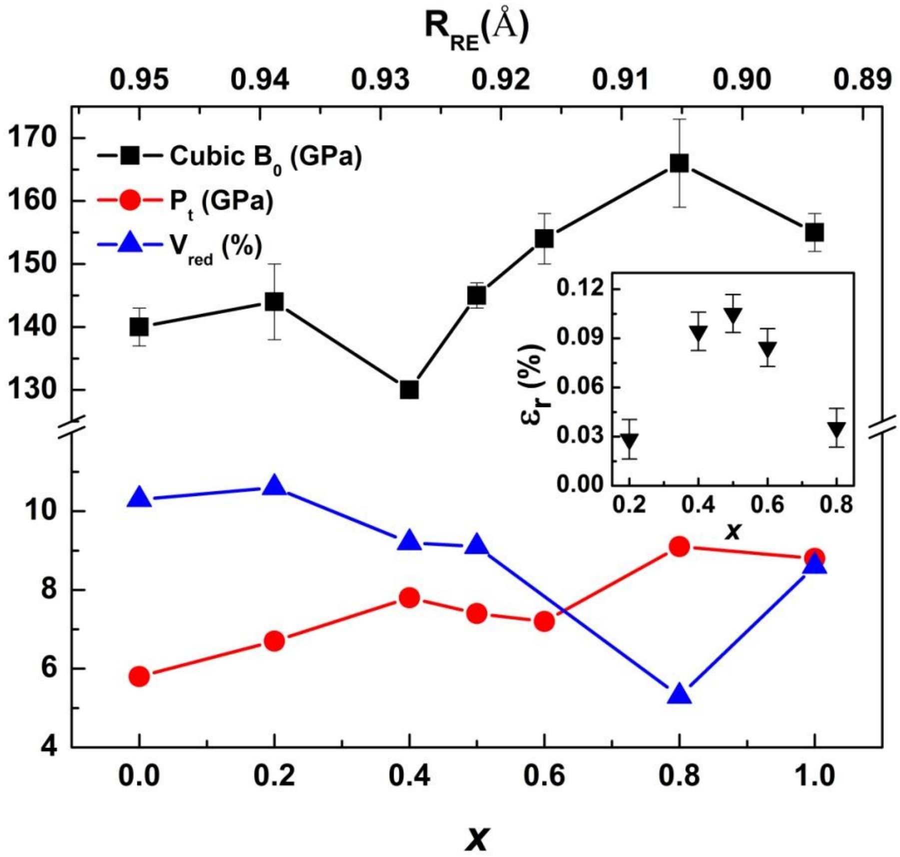

Fig. 5.15 The bulk moduli of cubic phase (B_0), transition pressure (P_t) and the volume reduction (V_{red}) across the transition for $(Eu_{1-x}Ho_x)_2O_3$. The inset shows the relative micro strain, ε_r, at ambient condition. P_t is within an error of ±0.1 GPa.

Table 5.5 Calculation of micro strain from the Rietveld refined Ly parameter of the ambient XRD data

x	Ly	Ly - Ly(x = 0)	ε_r (%)	$\Delta\varepsilon_r$
0	2.992	0	0	0
0.2	4.61(49)	1.62(69)	0.0286	0.01205
0.4	8.39(47)	5.40(67)	0.09427	0.01176
0.5	9.01(46)	6.02(67)	0.10512	0.01161
0.6	7.82(46)	4.83(66)	0.08439	0.01154
0.8	5.01(48)	2.02(68)	0.03534	0.01183

5.5. Pressure concentration phase diagram

Based on our HPXRD investigations, a pressure-concentration (P-*x*) phase diagram for $(Eu_{1-x}Ho_x)_2O_3$ up to a pressure of 15 GPa is constructed which is shown in Fig. 5.16. The stability region of the cubic, hexagonal and monoclinic phases along with their crystal structures are marked as I, II and III respectively. The region marked as IV, is identified as the phase boundary between high pressure hexagonal and monoclinic structures. Average cationic radii corresponding to each x is calculated using the definition of R_{RE} described earlier. In the region IV, the range of average cationic radii (R_r) is found to lie within $0.9164 < R_r < 0.9220$ Å. Hence it is evident that, the average cationic radii equivalent to or below 0.9164 Å prefers a C to B transition whereas cationic radii equivalent to or above 0.9220 Å prefers a transition from C to A.

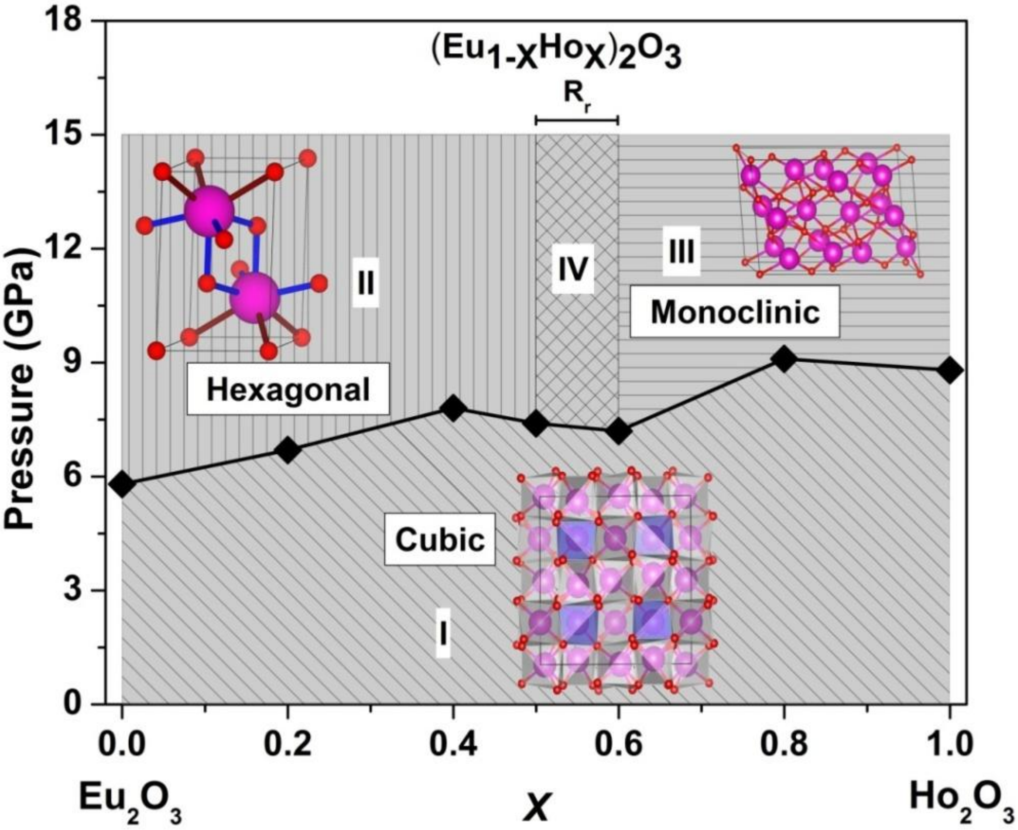

Fig. 5.16 Pressure – concentration (P-x) phase diagram for the solid solution $(Eu_{1-x}Ho_x)_2O_3$. Different crystal structures and their stability regions are marked accordingly. Transition boundary, R_r, is characterized by $0.9164 < R_r < 0.9220$ Å

5.6. Summary and conclusion

Mixed rare earth sesquioxides $(Eu_{1-x}Ho_x)_2O_3$ in the range $0.0 \leq x \leq 1.0$ have been prepared by *chemie douce* method. Formation of solid solutions in the entire range of compositions has been confirmed through X-ray diffraction. Rietveld refinement has been carried out and the structure parameters are reported. A random cationic distribution in the two crystallographic sites and a translational motion of the RE ion in the 24d site have been observed. Hardening of Raman modes in the high frequency range reveals an increase in bond strength, hence an increasing structural rigidity with the decrease in average cationic radii, R_{RE}. The disappearance of a weak low frequency band above $x = 0.8$ together with the slope change of the rare earth ion co-ordinate indicate that, they are correlated.

In order to understand the effect of cationic radii, high pressure behavior of the solid solutions $(Eu_{1-x}Ho_x)_2O_3$ were investigated using the in-situ angle dispersive high pressure X-ray diffraction technique. Our studies on various compositions of the mixed oxide show that when the average cationic radius, R_{RE} is equivalent to or below 0.9164 Å the system prefers a cubic to monoclinic transition as a function of pressure, whereas for average cationic radii equivalent to or above 0.9220 Å it prefers a transition from cubic to hexagonal. In the composition range $0.4 \leq x \leq 0.6$ the following trend is observed: the bulk modulus increases after a drastic reduction at x=0.4, whereas, the transition pressure decreases. This is identified as a consequence of the increasing internal pressure induced by the doping. A pressure concentration phase diagram for $(Eu_{1-x}Ho_x)_2O_3$ upto a pressure of 15 GPa is constructed based on our high pressure structural investigations. The range of average cationic radii $0.9164Å < R_{RE} < 0.9220Å$, represented by R_r in the phase diagram, is beleived to form the phase boundary between the two high pressure phases namely, hexagonal and monoclinic.

Chapter 6

High Pressure phase transitions in $(Eu_{1-x}La_x)_2O_3$

6.1. Introduction

In Chapter 5, the simultaneous effect of cation size and pressure have been presented on the solid solutions of medium cation sized RES (Eu_2O_3) and a small cation sized RES (Ho_2O_3). A single phase solid solution has been observed in the whole range of compositions for these systems with similar structure and very small difference in cationic radii. The present chapter is intended to study the simultaneous effect of cationic radii and pressure on the solid solutions of RES with dissimilar structure and with significant difference in cationic radii. The medium cation sized RES Eu_2O_3, crystallizing in the cubic structure at ATP, and the large cation sized RES La_2O_3, crystallizing in the hexagonal structure at ATP, with the difference of cationic radii 0.15 Å have been selected for the present study. When the difference in cationic radii exceeds the maximum that a particular structure can accommodate, a polymorphic structural phase transition is expected. The gradual increase in the structural instability and the resulting phase transition can be tuned by the systematic variation in R_{RE}. Further, Eu_2O_3 undergoes a direct C→A transition, whereas La_2O_3 shows no structural phase transition under pressure[4]. As these RESs follow completely different behavior, high pressure studies on their solid solutions may yield fundamental informations in understanding their structural stability and phase transitions in these oxides. Hence, the present chapter will cover the following aspects:-

i. Structure and morphological characterization of $(Eu_{1-x}Ho_x)_2O_3$ $[0.0 \leq x \leq 1.0]$ solid solutions using SEM-EDAX and X-ray diffraction at ATP.

ii. HPXRD studies on the selected compositions of $(Eu_{1-x}Ho_x)_2O_3$.

6.2. Ambient Characterization

The solid solutions, $(Eu_{1-x}La_x)_2O_3$ $[0 \leq x \leq 1]$ are synthesized using the method as described in the Chapter 5, section 5.2.1. In order to understand the composition, morphology and crystal structure as a function of R_{RE}, SEM-EDAX and X-ray structure characterizations have been carried out on the as prepared samples. The following sub sections will describe the major conclusions drawn from these studies.

6.2.1. SEM – EDAX

The elemental composition of the as prepared samples obtained from the EDS analysis has been tabulated in Table 6.1. The weight fraction obtained from the EDS analysis of different areas of the sample is in good agreement with the fractional weight of Eu and La consumed during the synthesis. This confirms the homogenous distribution of both the RE elements, Eu and La, with the desired composition. The scanning electron microscopy (SEM) image of $0.0 \leq x \leq 1.0$ samples, representing the $(Eu_{1-x}La_x)_2O_3$ solid solutions, are shown in Fig. 6.1. The particles show no specific morphology and are irregular in shape. The average particle size obtained from the analysis of the SEM image using the Image J software has also been tabulated in the Table 6.1. It is clearly seen that, the particle size of all the samples are in the 0.1-0.2 μm range. Thus, ultra fine particles of submicron range can be obtained by this method of synthesis.

Table 6.1 Composition and average particle size (D) from SEM-EDS measurement.

x	x (EDS)	D (nm)	x	x (EDS)	D (nm)
1	1	203	**0.4**	0.37(3)	141
0.9	0.85(5)	145	**0.3**	0.28(3)	126
0.8	0.75(5)	167	**0.2**	0.20(4)	114
0.7	0.65(3)	117	**0.1**	0.09(3)	111
0.6	0.56(3)	110	**0**	0	126
0.5	0.47(5)	142			

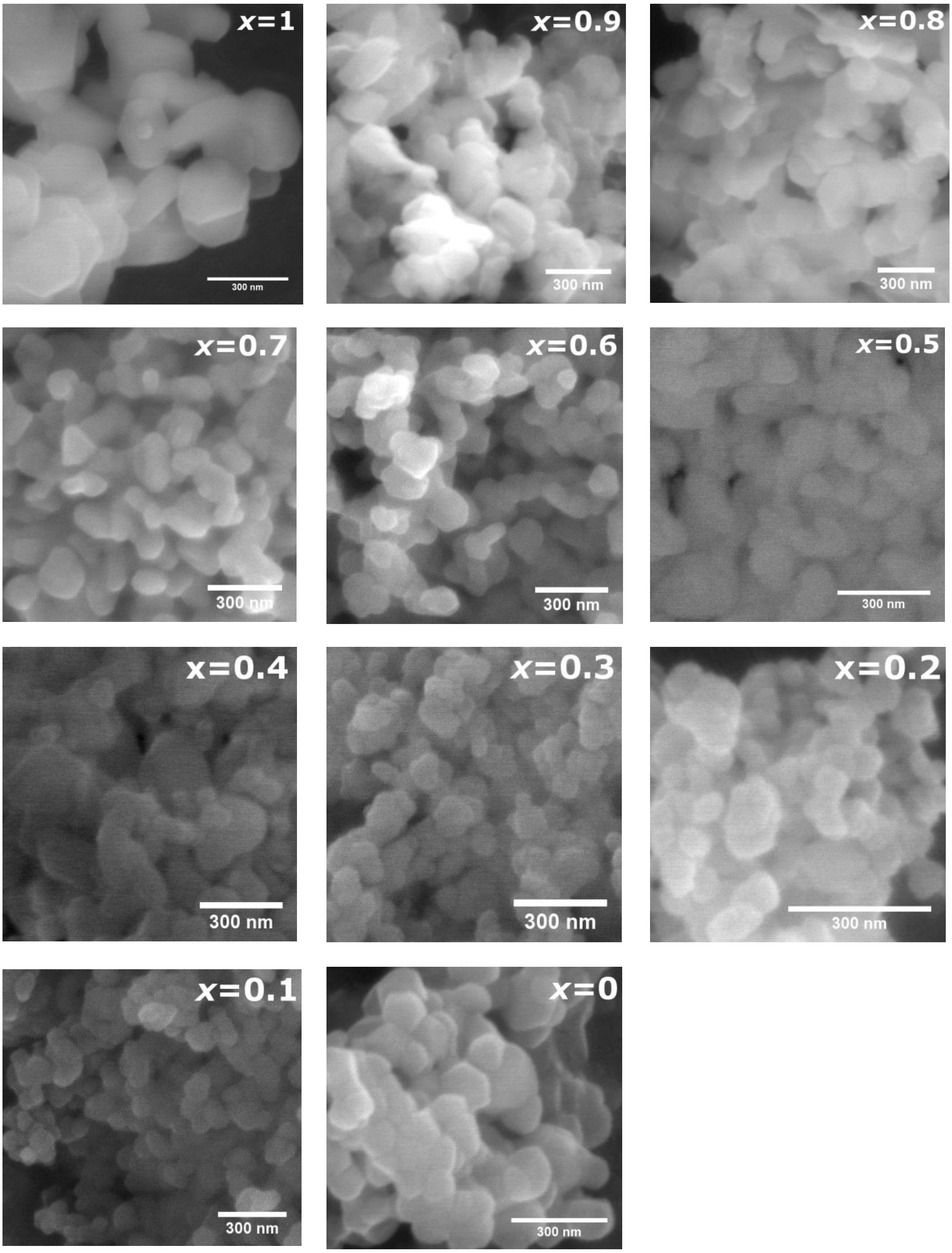

Fig. 6.1 SEM image of $(Eu_{1-x}La_x)_2O_3$, showing the irregularly shaped submicron size particles.

6.2.2. X-ray structure characterization

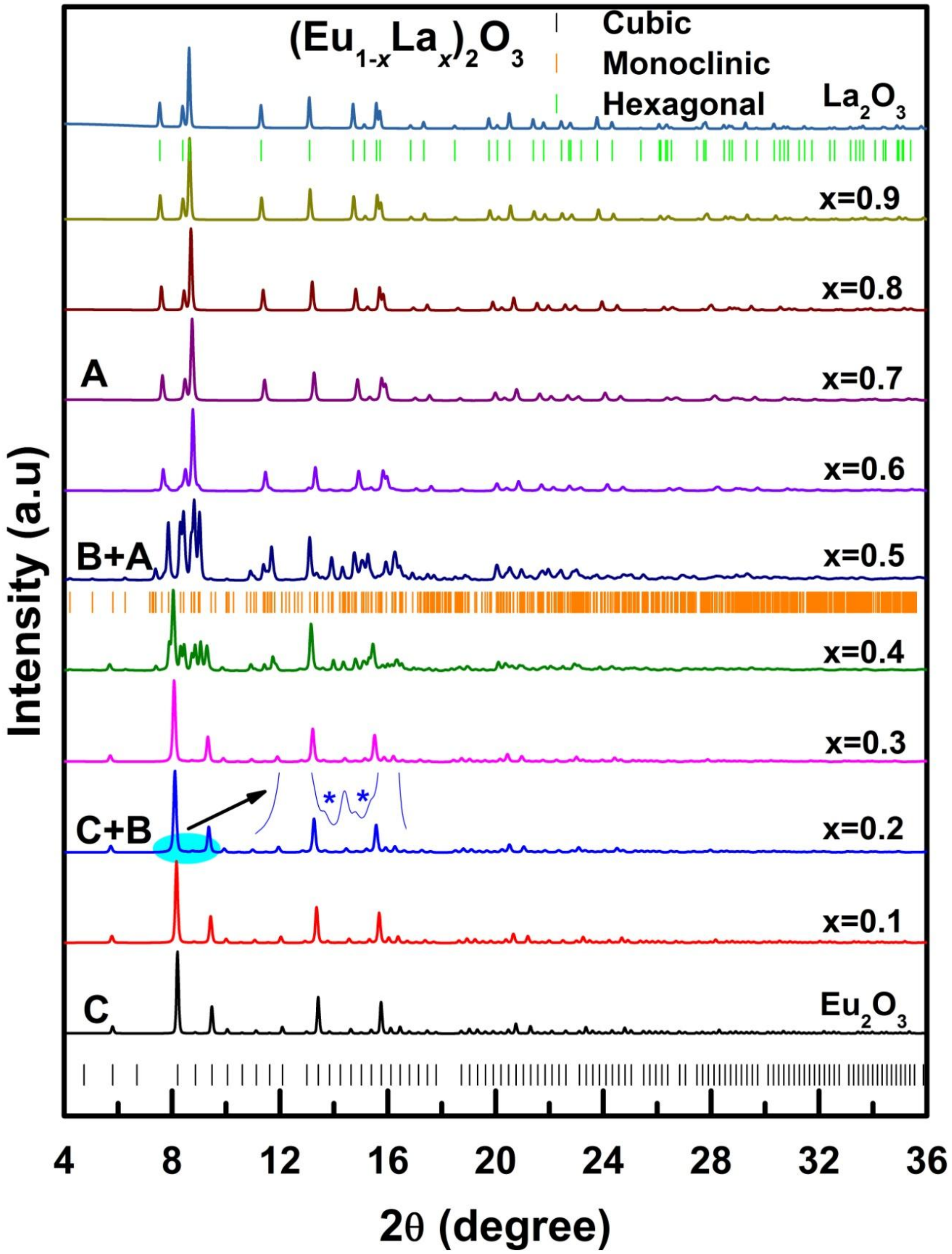

Fig. 6.2 X-ray diffraction pattern of $(Eu_{1-x}La_x)_2O_3$ ($0 \leq x \leq 1$) showing the C→B→A structural phase transition. Tick marks indicate the reflection positions of the cubic, monoclinic and hexagonal phases. The * marks in the zoomed region of x=0.2 diffractogram indicate the reflections from monoclinic phase during the C→B phase transition.

Fig. 6.2 shows the angle dispersive X-ray diffraction pattern of $(Eu_{1-x}La_x)_2O_3$ ($0 \leq x \leq 1$). For x=0, Eu_2O_3, it is found that the diffraction pattern could be indexed to the C-type cubic bixbyite structure. For x=1, all the observed diffraction peaks could be indexed to the A-type hexagonal structure. As the concentration of La doping increased the structural phase transition was clearly evident in these mixed oxides. At x= 0.2, origin of 3 new peaks at 8.48°, 8.91° and 9.12° indicates the onset of a structural phase transition in these oxides. Further with the increase in x, the new phase started growing with the presence of several other new prominent reflections at the expense of the parent cubic phase. At x= 0.4, the new phase thus formed could be clearly indexed to the B-type monoclinic phase. The absence of the parent cubic phase reflections show that the transition to monoclinic phase is complete at x=0.5. Further the Rietveld structure refinement on the x=0.5 sample showed that, even though the parent cubic phase was completely absent, the data could not be fitted to the monoclinic phase alone. This leads to the speculation that, there could be another phase which co-exists with the monoclinic phase at this composition. Obviously, the first possible candidate is its polymorphic phase, namely the A-type hexagonal structure with the space group *Pm-3m*. Hence, a two phase, monoclinic and hexagonal, Rietveld refinement has been carried out for the X-ray diffraction data of x=0.5. The refined structure fits reasonably well with the observed diffraction data, confirming the presence of the hexagonal structure. Fig. 6.3 shows the two phase Rietveld fit corresponding to x=0.5. The lattice parameters and different agreement indices are also indicated in the figure. Although the hexagonal phase co-exists with the monoclinic phase, the volume phase fraction is much less compared to the monoclinic phase (7%, see inset of Fig. 6.4b). Hence the monoclinic phase is the major phase for this composition. For x=0.6, a rapid growth of the hexagonal phase from 7 % to 81% has been observed, indicating the fast and quick rate of transformation. The total disappearance of the monoclinic peaks at *x*=0.7 reveals that, the transition from monoclinic to hexagonal phase is complete and the structure is stable in the hexagonal phase. For *x*=0.8 and 0.9, the single phase hexagonal structure is retained with no further structural phase transition. In addition to the structural phase transition, a significant peak shift towards the lower 2θ is clearly visible in the cubic and hexagonal structure with the increasing La_2O_3 substitution. This shift in peak position indicates an expansion of the lattice spacing due to the substitution of larger La ion with the comparatively smaller Eu ion. Rietveld refinement has been carried out for all the diffraction patterns by taking Eu_2O_3 and La_2O_3 as structural models. Peak profiles are modeled with the constant wavelength profile function 3 as employed in the GSAS+EXPGUI software package. Lattice parameters, profile parameters, atomic positions and iso thermal parameters were refined for all the phases. In the case of monoclinic phase the atom positions are not refined. Assuming that the microstructure remains the same, the peak width parameters of the multiple phases of a single composition has been constrained to have the same value.

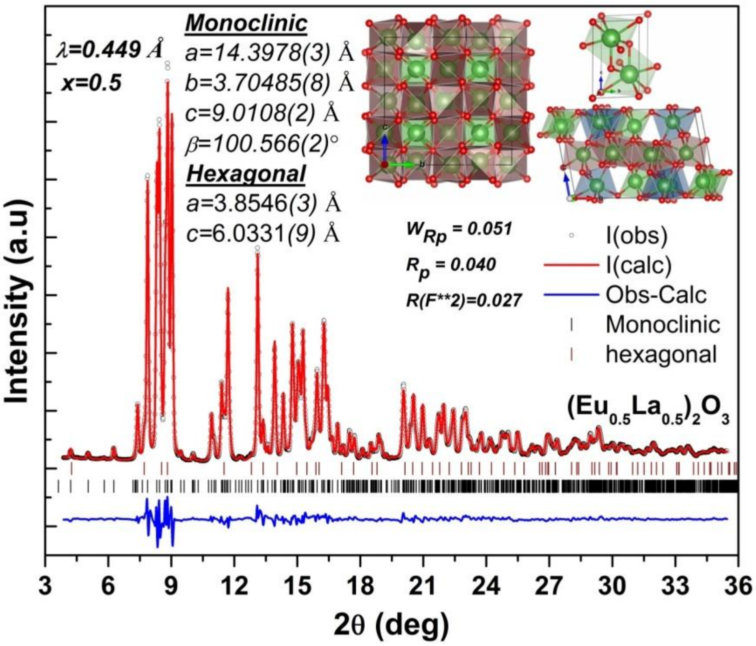

Fig. 6.3 Multi phase Rietveld refined pattern of $(Eu_{0.5}La_{0.5})_2O_3$ with the refined lattice parameters of the monoclinic and hexagonal structure. Unit cell of cubic, monoclinic and hexagonal structure is also depicted. The R factors together with the difference curve indicate a good fit to the experimentally obtained diffractogram.

Evolution of crystal structure with R_{RE}

In order to understand the effect of cationic radii, an average cationic radius, $R_{RE} = xR_{Ho}+(1-x)R_{Eu}$, has been defined as in the case of $(Eu_{1-x}Ho_x)_2O_3$ ($0 \leq x \leq 1$). In Eu_2O_3, the cations are in octahedral co-ordination with the oxygen atoms whereas, in La_2O_3, the cations are in 7 co-ordinations. Ionic radii of Eu^{3+} and La^{3+} in their 6 and 7 co-ordination environment were reported to be R_{Eu} = 0.950 Å and R_{La} = 1.10 Å respectively[116]. The $R_{RE} = xR_{La}+(1-x)R_{Eu}$ can be calculated from the individual cationic radii of Eu and La using the same expression as stated. It is found that, R_{RE} < 0.98 Å (ie, $x<0.2$) remains to be in the C-type structure whereas R_{RE} > 1.04 Å (ie, $x>0.6$) remains to be in the hexagonal structure. Although a single phase monoclinic structure could not be observed in the whole range of composition, the monoclinic structure could be stabilized in the 0.98 Å ≤ R_{RE} ≤ 1.04 Å, with a higher probability of formation in the region 1.010 Å ≤ R_{RE} ≤ 1.025 Å. R_{RE} = 1.04 Å and R_{RE} = 0.98 Å are known to be the largest and smallest ionic radii respectively for which a monoclinic phase has been observed. The present experimental results substantiate the fact that, doping of La_2O_3 induces C→ B → A structural phase transitions in the rare earth sesquioxide Eu_2O_3. The C→ B transition starts at R_{RE}=0.98 Å whereas B→A is at R_{RE}=1.025 Å.

R_{RE} dependence of unit cell

Fig. 6.4a represents the variation in the normalized lattice parameters as a function of R_{RE}/x. It is evident that, the lattice parameters of cubic, monoclinic and hexagonal structures are increasing with an increase in R_{RE}/x. These expansions of the lattice are driven by the steric effect caused by the difference in the size of the rare earth ion. This lattice expansion is controlled by the substitution of larger La^{3+} ions in the place of the smaller Eu^{3+} ions which in turn reflects in the increasing lattice parameters[121, 133]. Further, an anisotropic expansion of lattice parameters for the monoclinic and hexagonal structure has been observed with an increasing R_{RE}/x. In the monoclinic phase a higher rate of expansion is observed along the *b* axis followed by the *c* and the *a* axis. Pauling's rule states that, the shared polyhedral edges and shared polyhedral faces decrease the stability of the crystal structure. This decrease in stability arises from the cation-cation Coulomb terms[134, 135]. The presence of close packed edge sharing octahedral arrangement along the *b* axis (see inset of Fig. 6.3) makes the rare earth ions closer together leading to a significant increase in the repulsive energy[134, 135]. As this is the shortest, and hence strongest, rare earth-rare earth bond in this structure, a lower compressibility and hence a higher rate of expansion is expected. The large number of voids present in both *c* and *a* direction and the presence of additional corner sharing octahedral arrangements make the expansion minimal along the *c* and *a* direction in the monoclinic structure. Similarly, a higher rate of expansion is observed along the *a* axis compared to the *c* axis in the hexagonal structure. Again, the presence of close packed edge sharing polyhedral arrangement along the *a* and *b* axis leads to this anisotropic expansion as discussed earlier. The variation in the axial ratios c_m/a_m, c_m/b_m, a_m/b_m and c_h/a_h (the subscripts *m* and *h* stand for monoclinic and hexagonal structures respectively) for both the monoclinic and hexagonal structures at various R_{RE}/x has been tabulated in Table 6.2. A linear behavior with the increasing R_{RE}/x has been observed for both the phases. It has been found that, the monoclinic phase nucleated with the axial ratios c_m/a_m= 0.623, c_m/b_m= 2.450 and a_m/b_m = 3.934. Correspondingly the hexagonal phase has been found to have a c_h/a_h ratio of 1.565 when it is just nucleated at x=0.5. The variation in the unit cell volume as a function of R_{RE}/x is given in the Fig. 6.4b. An increase in the unit cell volume with an increase in x is observed for all the three phases. The replacement of smaller Eu ion with the larger La ion in the lattice sites of these phases causes an overall expansion of the crystal lattice leading to the observed increase in unit cell volume. Moreover, the C→B transition is accompanied by a 7.7% volume drop at x=0.2 whereas B→A phase transition is accompanied by 1.4 % volume collapse at *x*=0.5. These volume reductions are comparable with the values obtained from the high pressure experiments of these rare earth sesquioxides, in which the typical value of volume reductions for C→B and B→A are found to be 6.5-10% and 1 -2% respectively[2, 5, 41, 43].

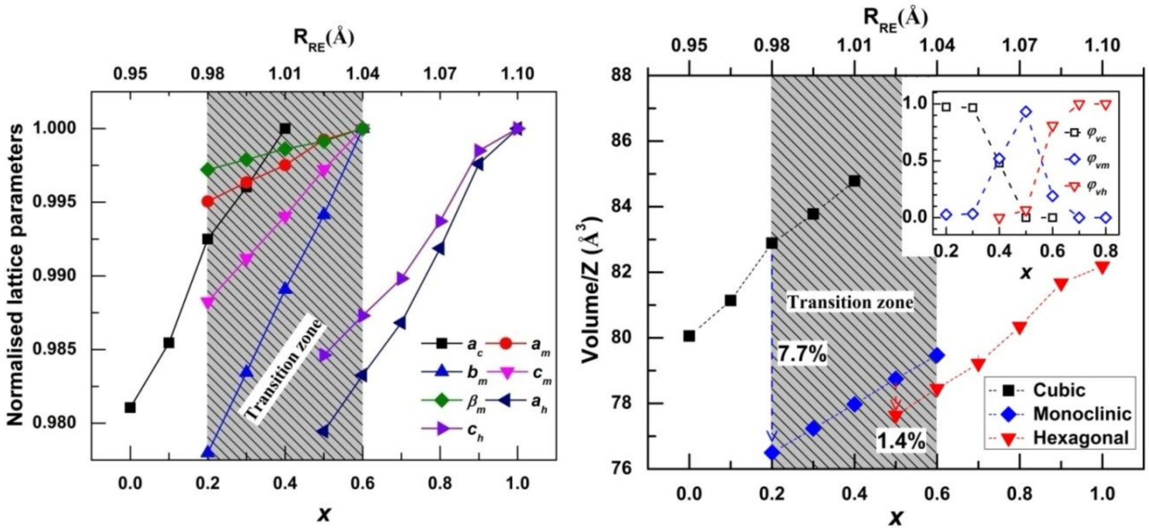

Fig. 6.4 a) Variation of normalized lattice parameters as a function of R_{RE}/x. The shaded region represents the biphasic region of C→B and B→A transitions. b) Evolution of unit cell volume as a function of R_{RE}/x. Shaded region represents the biphasic region, where the C→B and B→A transitions are observed. The volume reductions at the transition points are also shown. The inset shows the growth of the individual phases in terms of the volume phase fraction (ϕ_v). The subscript *c*, *m* and *h* stand for cubic, monoclinic and hexagonal phases respectively.

Table 6.2 The variation of crystallographic axial ratios c_m/a_m, c_m/b_m, a_m/b_m and c_h/a_h (subscripts m and h stands for monoclinic and hexagonal structure respectively) for monoclinic and hexagonal structures and volume of the RE-O polyhedrons of the respective phases as a function of R_{RE}/x.

x	R_{RE} (Å)	c_m/a_m	c_m/b_m	a_m/b_m	c_h/a_h	Polyhedral volume (Å^3)					
						RE_{8b}	RE_{24d}	RE_{4i}	RE_{4i}	RE_{4i}	RE_{2d}
0	0.95					15.234	16.110				
0.1	0.965					15.451	16.373				
0.2	0.98	0.62282	2.45009	3.93389		15.719	17.176				
0.3	0.995	0.62386	2.44374	3.91711		15.844	17.454				
0.4	1.01	0.62493	2.43683	3.89939		16.043	17.790	17.303	21.331	22.687	
0.5	1.025	0.62584	2.43216	3.88621	1.56519			17.262	21.809	21.812	22.270
0.6	1.04	0.62711	2.42465	3.86639	1.56335			17.420	22.009	22.012	22.495
0.7	1.055				1.56169						22.659
0.8	1.07				1.55985						22.981
0.9	1.085				1.55835						23.352
1	1.1				1.55696						23.452

Micro strain and substitutional disorder: Driving force of phase transition

As the particle size estimated from the SEM images showed the micro crystalline character, the X-ray peak width will be predominantly influenced by the micro strain developed on doping. Rietveld refined profile shape parameters are used to deduce the micro strain as described in the GSAS manual[94]. A micro strain parameter, ε_r, is defined relative to the end member, Eu_2O_3, as;

$$\varepsilon_r(\%) = \frac{\pi}{18000}\left[L_{yx} - L_{yo}\right] * 100 \quad (6.1)$$

where, L_{yx} and L_{yo} are the Rietveld refined Lorentian component of the strain parameters for the composition x and x= 0 respectively. Fig. 6.5a shows the variation of micro strain (ε_r) relative to the end member, Eu_2O_3, with increasing La substitution. It is clear that, ε_r follows a non monotonous behavior with R_{RE}/x. Such a strain behavior was observed earlier in the cubic Eu:Ho_2O_3 (Chapter 5), Gd:Ho_2O_3 and Gd:Yb_2O_3 solid solutions[121]. As we have seen earlier, the effect of La substitution results in the expansion of the unit cell volume, the observed micro strain could be treated as tensile in nature. The tensile strain, ε_r , clearly shows an increasing trend with the La substitution up to x=0.3 (R_{RE}=0.995 Å) at which the cubic structure becomes unstable and the onset of C→B transition occurs. Once the nucleation starts, the tensile strain relaxes, in the region $0.3 < x < 0.7$. No further increase in the tensile strain has been observed in the region $0.3 < x < 0.6$. Although, there is no significant increase in the tensile strain in this region, the monoclinic phase transforms to the hexagonal structure (B→A) at x = 0.5. These B→A transitions in rare earth sesquioxide is associated with the minor displacement of the oxygen atoms and hence the transition is displacive in nature[2, 19, 37]. This indicates that, the transition is associated with a lower energy barrier. Therefore, the energy required for the transition might be derived from the fluctuations in the system. Beyond x=0.7, the ε_r , relaxes and a pure hexagonal phase is observed. As this region is purely hexagonal and $R_{RE} < R_{La}$, the cations easily get accommodated in the hexagonal lattice, hence a relaxation in ε_r is observed. In accordance with this, Fig. 6.5b shows the variation in the overall isothermal parameter, U_{iso}, of cubic and hexagonal structure. Typically, atoms with low thermal parameters are considered to be part of a well ordered structure and those with large thermal parameters are part of a structure which is flexible/less ordered. The increasing U_{iso} in the cubic structure with an increase of R_{RE} indicates an increasing substitutional disorder in the system. However, the reduction of U_{iso} in the hexagonal structure with an increasing R_{RE} indicates the progression towards the formation of an ordered structure.

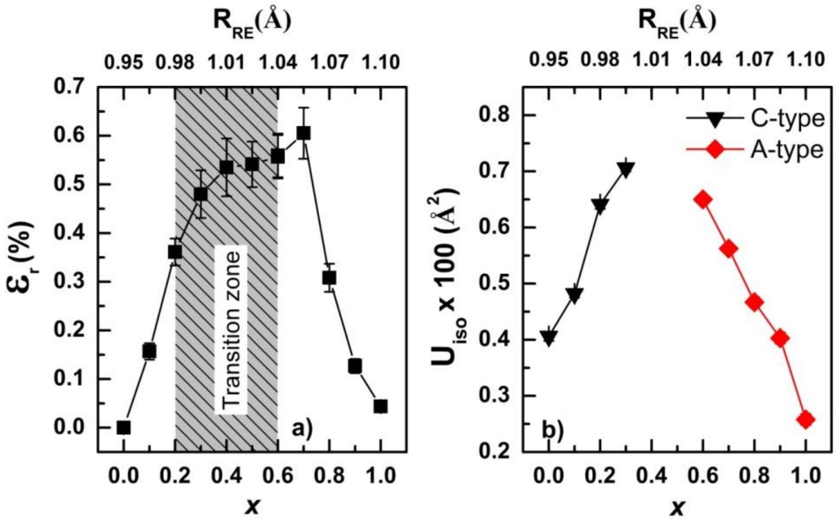

Fig. 6.5 a) The non monotonous behavior of relative micro strain (ε_r) with increasing R_{RE}/x. The shaded region is the transitions zone where ε_r remain almost the same. b) The variation in the isothermal parameter indicating the increasing and decreasing disorder in the cubic and hexagonal structures respectively.

Evolution of local structure

In the cubic structure, the octahedron at 8*b* site is made up of single bond length, designated as RE(8*b*)-O, whereas three different bond lengths, designated as RE(24*d*)-O1, RE(24*d*)-O2 and RE(24*d*)-O3 form the octahedron at 24*d* site. Similarly, in the case of hexagonal structure, the cations are in 7 co-ordination polyhedral environment which is comprised of three different bond lengths designated as RE-O1(2*d*), RE-O2(2*d*) and RE-O1(1*a*). The variation of different bonds in these polymorphic structures as a function of x/R_{RE} is shown in the Fig. 6.6 a&b. A systematic increase in bond length with La substitution has been observed for all the bonds in all phases except the RE(24*d*)-O1of the cubic phase. The increase in bond length with La substitution is a consequence of the larger ionic radii of the La compared to Eu, ie increase in R_{RE}. This decreases the bond strength and eventually the structure loses its rigidity with increasing R_{RE} (Chapter 5). However, RE(24*d*)-O1 bond remains same indicating that there is no elongation in this bond direction. More over the RE and the oxygen atoms (at 2*d*) have been found to be displacing away from each other along the c axis with an increase in the R_{RE}. This is clearly shown in the Fig. 6.6c, in which the fractional co ordinate, z, of rare earth and the oxygen atoms shift away from each other. This could be due to the increasing nature of covalency between the O- p orbital and rare earth-pd orbitals with a decrease in the rare earth ionic radii [19, 24, 31]. This increasing nature of directional covalent bonding brings the rare earth and oxygen atoms together leading to the observed co-operative movement between them.

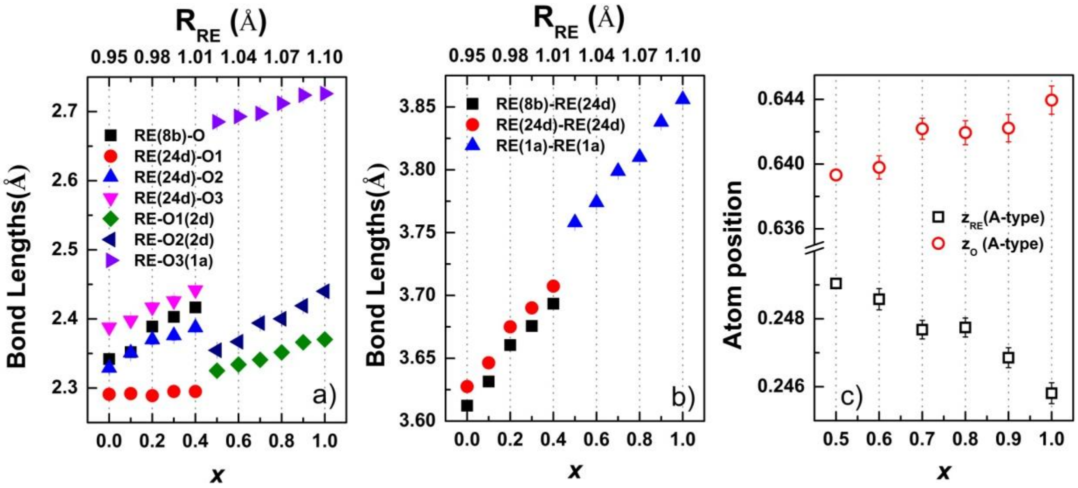

Fig. 6.6 a&b) Variation of bond length in cubic, monoclinic and hexagonal structure, showing the increasing trend with an increase in R_{RE}/x except for RE(24*d*)-O1 where it shows no change . c) The change in fractional z co-ordinate of RE (Z_{RE}) and oxygen (Z_O) atoms in the hexagonal structure.

It is worth to note here that, the steric effect caused by the difference in the size of the rare earth ion results in the development of micro strain within the crystal system. This largely influences the local structure of the crystals in terms of changes in bond lengths, bond angles, and polyhedral distortions[122, 124, 136]. From the present study it can be concluded intuitively that, the micro strain developed on doping manifests as an internal pressure in the crystal structure leading to the observed C→B→A structural phase transition in these oxides. Such a micro strain assisted internal pressure is found to have a significant role in reducing the transition pressure and bulk modulus in a similar rare earth oxide system Eu:Ho_2O_3 (Chapter 5). This signifies that the micro strain plays a substantial role as similar to the external pressure in driving the phase transition in these oxides. In the rare earth sesquioxides, the hexagonal structure has the smallest molar volume followed by monoclinic and cubic structure. Thus the hexagonal phase formation is more favorable under the application of external pressure. Hence, the C→B→A transition observed in the present experiments could be analogous to the pressure induced C→B→A transitions reported in many of the rare earth sesquioxides[2, 19, 38, 114].

6.3. Polymorphic phase transitions in $(Eu_{1-x}La_x)_2O_3$ at high pressures

In the following sub sections, the major results and conclusions drawn from the high pressure synchrotron X-ray diffraction measurements carried out on the $(Eu_{1-x}La_x)_2O_3$ powder samples are presented.

6.3.1. Identification of phase transitions from HPXRD

ADXRD has been carried out at various pressures on the selected compositions of $(Eu_{1-x}La_x)_2O_3$, x =0, 0.2, 0.3, 0.4, 0.5, 0.6, 0.8 and 1. Representatives of the diffractograms recorded at various pressure steps are shown in Fig. 6.7, Fig. 6.8 and Fig. 6.10. For x=1 the detailed results are presented in section 4.4 of Chapter 4. It can be seen that, the diffraction data for x = 1, 0.8, 0.6 , does not show any signature of structural phase transition till the highest experimental pressure, 26.5, 27.4 and 24.2 GPa respectively for x=1, 0.8 and 0.6, achieved for each of them. This implies the stability of the hexagonal structure of these oxides atleast up to 25 GPa . In the case of x= 0.6, even though the ambient data shows the presence of a small fraction of monoclinic phase along with the hexagonal phase, the diffraction pattern at 4.3 GPa clearly shows that, the monoclinic phase is absent. This signifies that, the monoclinic phase is completely transformed to the hexagonal structure well below this pressure. Also, it has been observed that, the *100* peak of the hexagonal structure of x=0.8 and 0.6 hardly shifts with an increase of pressure in the ~10-22 GPa pressure regime, indicative of the presence of anomolous lattice compressibility as observed in the case of La_2O_3 (Chapter 4, section 4.4).

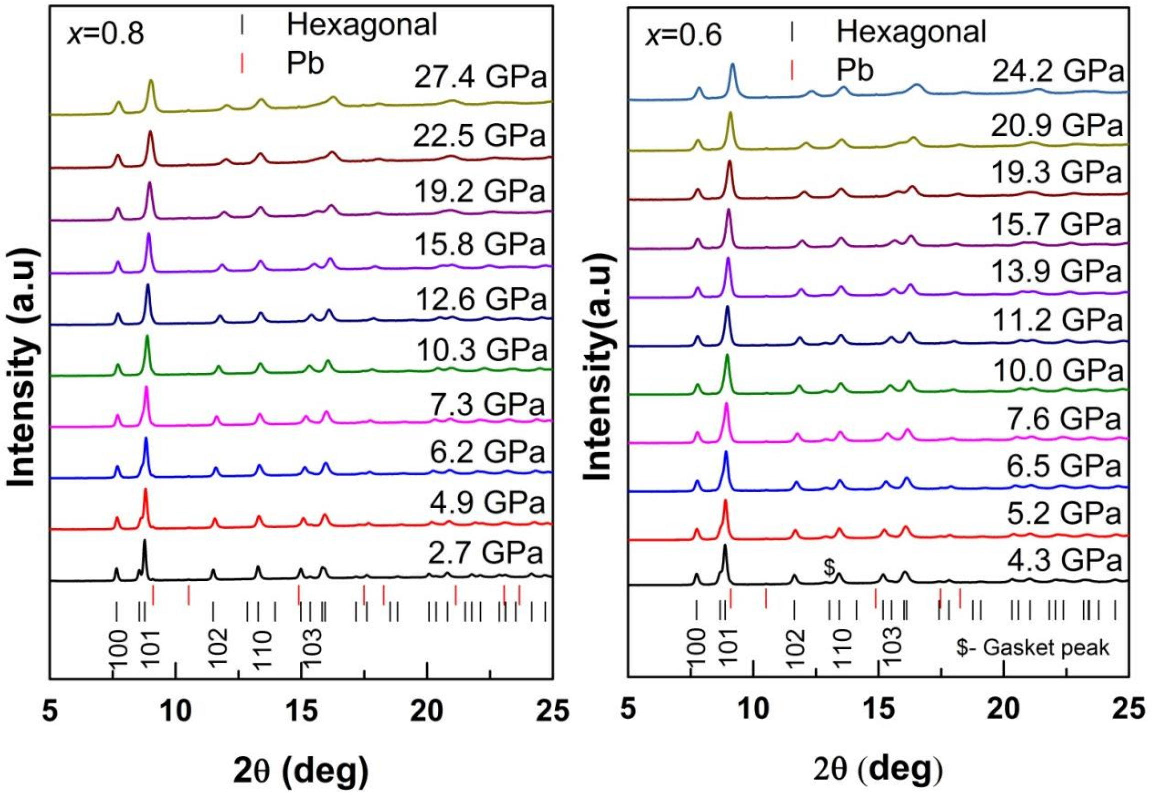

Fig. 6.7 HPXRD pattern of x = 0.8 and 0.6 at various pressures showing the stability of hexagonal structure up to the highest experimental pressure. '$' symbol indicate the peak corresponding to the gasket material. A minor fraction of Lead (Pb) was observed due to the X-ray slit introduced to the DAC (Chapter 3).

For x=0.5, a mixture of monoclinic and hexagonal phase is observed at ATP. HPXRD patterns of x=0.5 is shown in the Fig. 6.8a. With an increase of pressure, the B phase is found to be gradually transforming to the A phase. This transition is completed at 10.2 GPa, where a pure A phase is observed. Further increase in pressure does not induce any structural phase transition and the A phase is found to be stable up to 30.5 GPa. In the case of x=0.4, coexistance of cubic and monoclinic phase is observed and their presence has been verified using the Rietveld structure refinement of the ambient diffraction pattern as described in the section 6.2.2. The HPXRD pattern corresponding to x=0.4 is shown in Fig. 6.8b. As can be seen from the figure, the C+B mixed phase completely transformed to the A phase at 17.1 GPa. Further increase in pressure upto 34 GPa does not show any structural phase transition in this oxide. However, it is difficult to say whether the C→A or the B→A transition takes place first. To remove this ambuiguity, a quantitative multi phase analysis using the Rietveld structure refinement is carried out for all the HPXRD patterns.

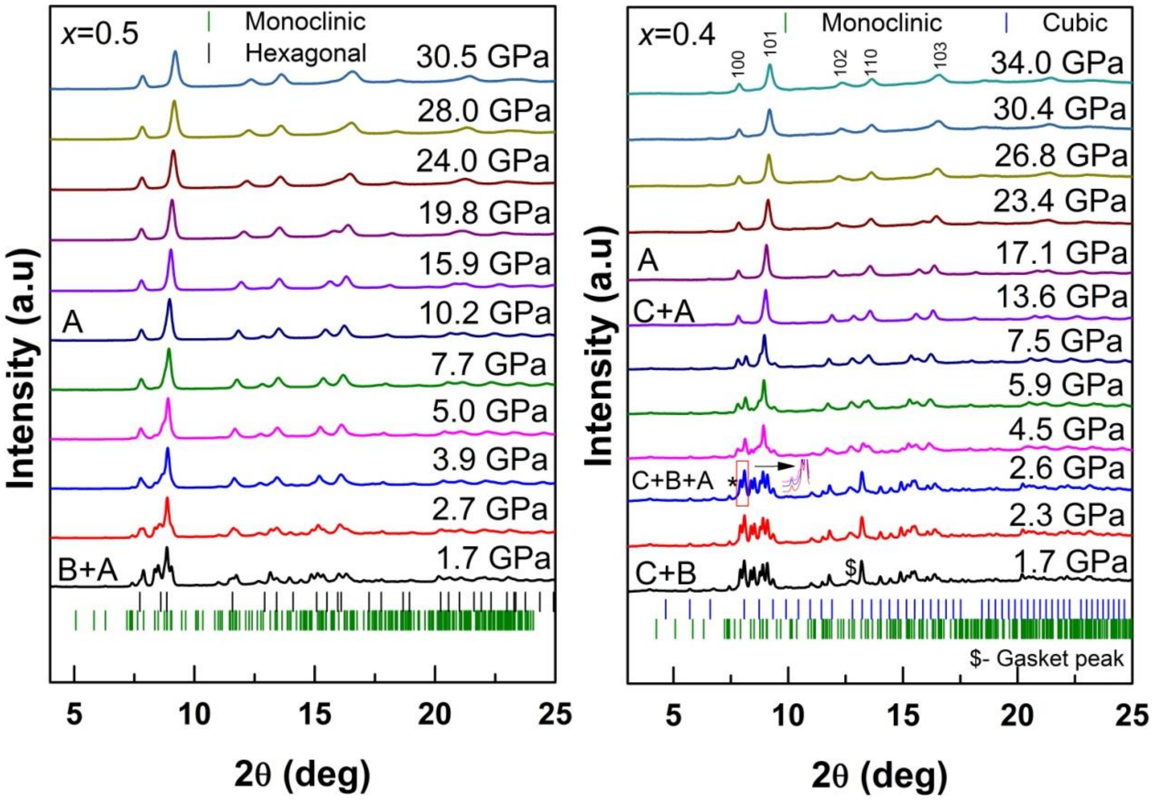

Fig. 6.8 HPXRD pattern of x = 0.5 and 0.4 at various pressures. C, B, A represents the cubic, monoclinic and hexagonal structures respectively. '$' symbol indicate the peak corresponding to the gasket material. The tick marks represent the reflections belonging to the corresponding phases.

The representatives of Rietveld fit corresponding to x=0.4 at various pressure steps, 1.7 GPa, 4.5 GPa and 17.1 GPa, are shown in Fig. 6.9a-c. The unit cell parameters for the cubic, monoclinic and the hexagonal phases along with the different R factors are depicted in the figure. The small values of different agreement indices indicate the excellent quality of the fit to the observed diffractogram. It is worth mentioning here that, the observed diffraction data at 2.6 GPa shows an appreciable intensity difference from the calculated one in the 2θ range 7.75°-8° when fitted with the cubic and the monoclinic phase alone. This suggests the possibility of onset of hexagonal structure in this oxides at this pressure. Hence, the refinement has been carried out by including the hexagonal structure, and the difference in intensity is observed to be minimized. Thus we conclude that, the onset of C/B→A structural phase transition in this oxide is at 2.6 GPa. Further refinement has been carried out using all the three phases and the phase progression is tracked by means of weight fraction of individual phases. Fig. 6.9d represents the weight fraction of cubic monoclinic and hexagonal structures with the increse of applied pressure. It is clear that, till 2.6 GPa, the cubic and monoclinic phase retains its weight fraction. At 2.6 GPa the weight fraction of monoclinic phase starts decreasing whereas the cubic phase does not show any change. Correspondingly, the fraction of hexagonal phase has stepped up to 0.13 and the same amount of reduction has been observed for the monoclinic phase. This drop and rise of weight fraction of monoclinic and hexagonal structure, respectively, clearly indicate the monoclinic to hexagonal transition at 2.6 GPa. The weight fraction of cubic phase continues to remain the same till 5.9 GPa, where a fraction of 0.1 drop has been observed. Also the fraction of monoclinic phase drops to 0.2 at this pressure. These indicate that, B→A is the dominant transition between 2.6-5.9 GPa. Above 5.9 GPa, a gradual reduction in the fraction of cubic and monoclinic phase is observed and B→A transition is complete below 13.6 GPa. This points to the fact that, between 5.9 to 13.6 GPa, both cubic and monoclinic phases contribute towards the growth of hexagonal structure. On further increse in pressure to 17.1 GPa, the remaining cubic phase transforms completely to the hexagonal structure. Beyond this pressure, the hexagonal structure remains stable up to 34 GPa.

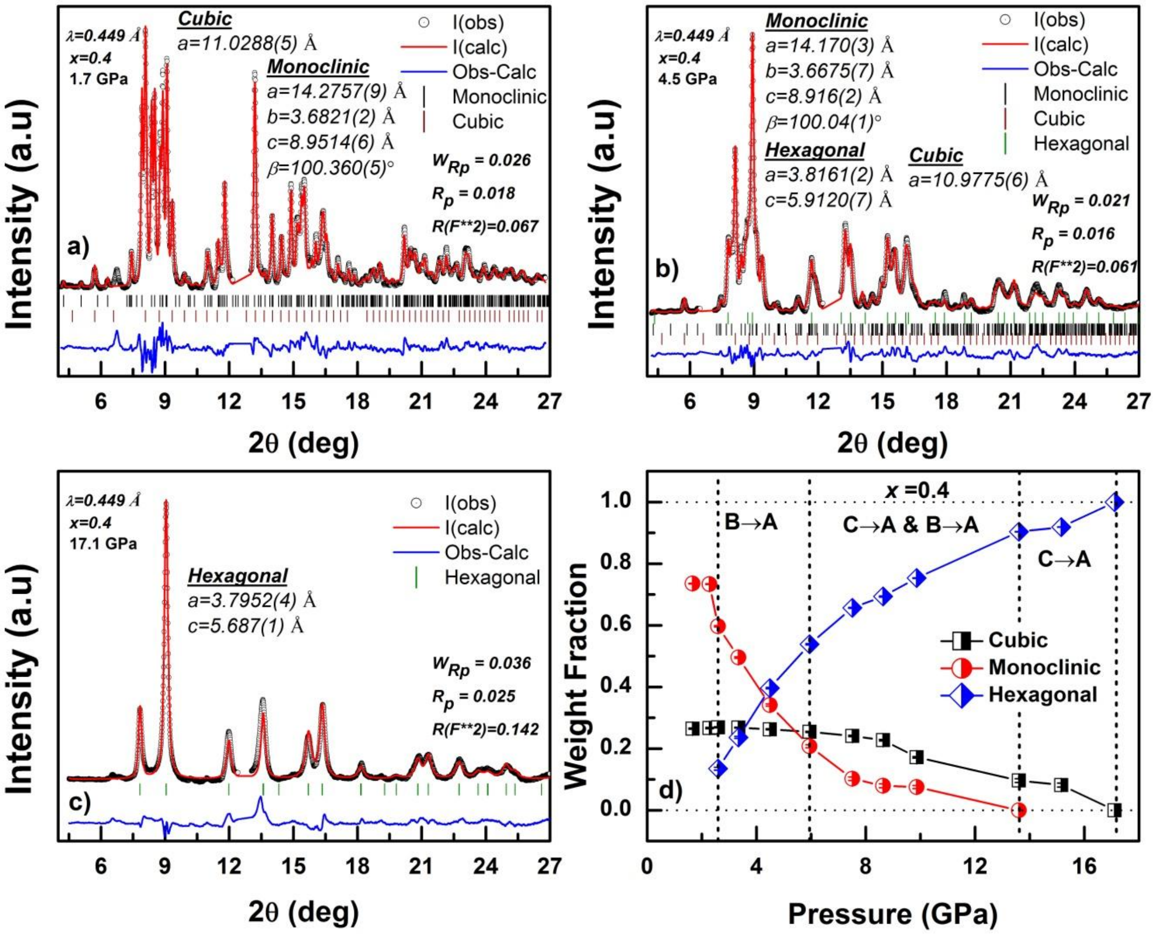

Fig. 6.9 Representative of Rietveld fits for x=0.4 at various pressure steps; a) at 1.7 GPa, b) at 4.5 GPa and c) at 17.1 GPa. The refined values of lattice parameters and the agreement indices are depicted in the respective plots. d) The weight fraction of cubic, monoclinic and hexagonal structures with increasing pressure showing the phase progression. The vertical dotted lines separate the different regions of B→A and C→A transitions.

In the case of *x*= 0.3 and 0.2, coexistance of cubic and monoclinic structure is observed at ATP. However, the phase fraction of the monoclinic phase is significantly low in these two compositions. Hence tracking the monoclinic phase with pressure is found to be extremely difficult. Moreover, considering the absorption of X-rays by diamonds in a DAC, the scattering from a phase with such a low fraction could not be well resolved. Hence, for *x*=0.3 and 0.2, the analysis is carried out by focusing on the major cubic phase and the monoclinic phase is not considered further in the discussion. Fig. 6.10 shows the HPXRD patterns collected for *x*= 0.3 and 0.2 at different pressure steps. Typically, the structural transitions either from C→B or C→A is characterised by the origin of a new peak near the cubic *123* and *222* peak. For *x*=0.3, the diffraction pattern does not show any signature of structural phase transition till 5.8 GPa. The origin of a new peak at 8.96° near the cubic *123* peak at 5.8 GPa indicate the onset of structural phase transition in this oxide. With further increae in pressure, the high pressure phase starts growing and the transition is complete at 14.3 GPa. The high pressure phase could be indexed to the known hexagonal structure with space group *P-3m1* [4]. This C→A transition is much similar to the one observed in the intermediate cation sized rare earth sesquioxides like Sm_2O_3, Eu_2O_3 and Gd_2O_3 [4, 5, 32]. There is no structural phase transitions observed with further increase of pressure up to 29.5 GPa, indicating the stability of the hexagonal structure up to this pressure. For *x*=0.2, a similar transition is observed at 4.3 GPa with the origin of a new peak at 2θ= 9°. Since the transition pressure is comparatively lower than that of the *x*=0.3, it is speculated that, the B→A transition could have taken place before the C→A transition as in the case of *x*=0.4. However, it is difficult to confirm due to the low phase fraction and the absence of well resolved monoclinic peaks in the HPXRD data. The parent phase completely transforms to the high pressure phase below 14.1 GPa. The high pressure phase could be indexed to the hexagonal structure as in the case of *x*=0.3. Further increse in pressure to 31.1 GPa, does not induce any structural phase transition and the system remains in the hexagonal structure. For *x*=0, the pure Eu_2O_3 has been studied up to 28.1 GPa and a phase transition from cubic to hexagonal structure is observed at 5.3 GPa. This is in good agrement with the literature report [4]. The C→A transition in this pure oxide is complete at 19 GPa and the hexagonal structure is found to be stable up to 28.1 GPa.

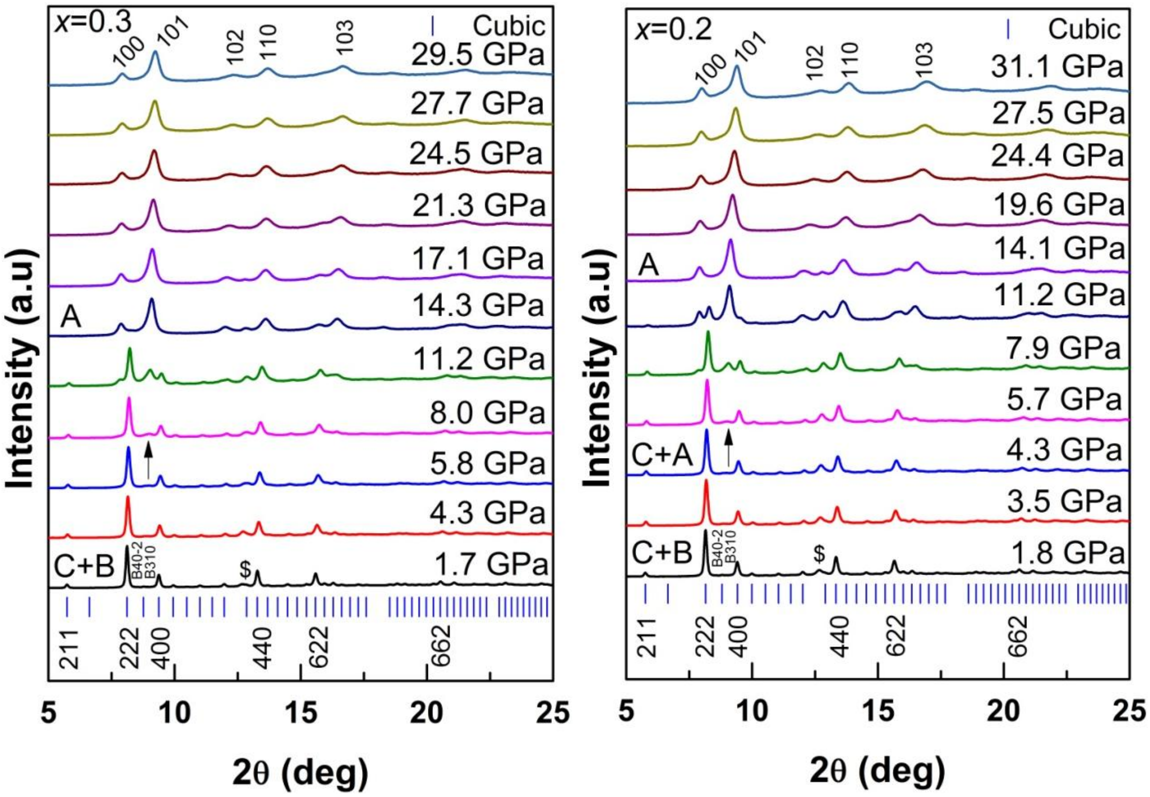

Fig. 6.10 HPXRD pattern of $x = 0.3$ and 0.2 at various pressures. The onset of C/B→A phase transitions is indicated by up arrows. C, B, A represents the cubic, monoclinic and hexagonal structures respectively. '$' symbol indicates the peak corresponding to the gasket material. The tick marks represent the reflection positions belonging to the individual phases.

As we have seen in the section 6.2 of this chapter and Chapter 5, the structure and phase transitions in the RES are highly influenced by their cationic radii. In Chapter 5 we have seen that, increase in cationic radii decreases the tarnsition pressure and bulk moduli and drives the phase transition route from C→B to C→A. Also in the section 6.2.2, we have seen that, these transitions from C→B→A can be realized just by varying the average cationic radii, $R_{RE,}$ in a systematic way. The high pressure studies on these solid solutions have now proved that, the pressure also favours the same transition route which are observed by increasing the R_{RE} of the solid solution. The deviation from this can be seen in the cubic systems, (for x=0, 0.2, and 0.3), in which the increse in R_{RE} induces a

C→B transition whereas the pressure induces a C→A transition. This is due to the comparatively lower stability of monoclinic phase of a particular composition over the cubic phase when treated under pressure, as we have seen in the case of x=0.4. It seems that, the pressure drives the mixed phase, either C+B or B+A, towards the hexagonal structure which is the primary structure exhibited by the RES with large cationic radii. Hence, It is clear that, the C→ B→A transition in $(Eu_{1-x}La_x)_2O_3$ observed with an increase in the R_{RE} is further enhanced with the increase of pressure.

6.3.2. Lattice compressibility and equation of state

Fig. 6.11a-c shows the change in lattice parameters with increasing pressure for those compositions in which the hexagonal structure is found to be stable at ATP. It is clear that, the anomalous lattice compressibility along the *a* axis is present in all the hexagonal structures irrespective of the compositions studied. This is due to the shifting of cations from the *103* plane to the *100* plane. The pressure width of the anomalous region for the hexagonal phase of pure La_2O_3 is about 9.68-24.2 GPa, whereas the region is shifted to 12.42-19.77 GPa in the case of x=0.5. This implies that, not only the onset of the anomaly is shifted to a high pressure region but also, the pressure width where the anomaly is observed shifts to a lower value with a decrease in R_{RE}. This could point to the fact that, the movement of RE-O layers is getting restricted with increase of pressure and decrease of R_{RE}. The *c* axis in these compositions shows a decreasing trend and the *c*/*a* ratio also observed to be monotonously decreasing with pressure. Fig. 6.11d-f show the change in lattice parameters with increasing pressure for those compositions in which the hexagonal structure is found to be stable at high pressures. In this case, the anomaly still holds and it is found to be shifting towards the high pressure region when the R_{RE} decreases. The c axis and the c/a ratio follow the same trend as observed earlier. This concludes that, the anomalous compression is an inherent property of the hexagonal structure of rare earth sesquioxides.

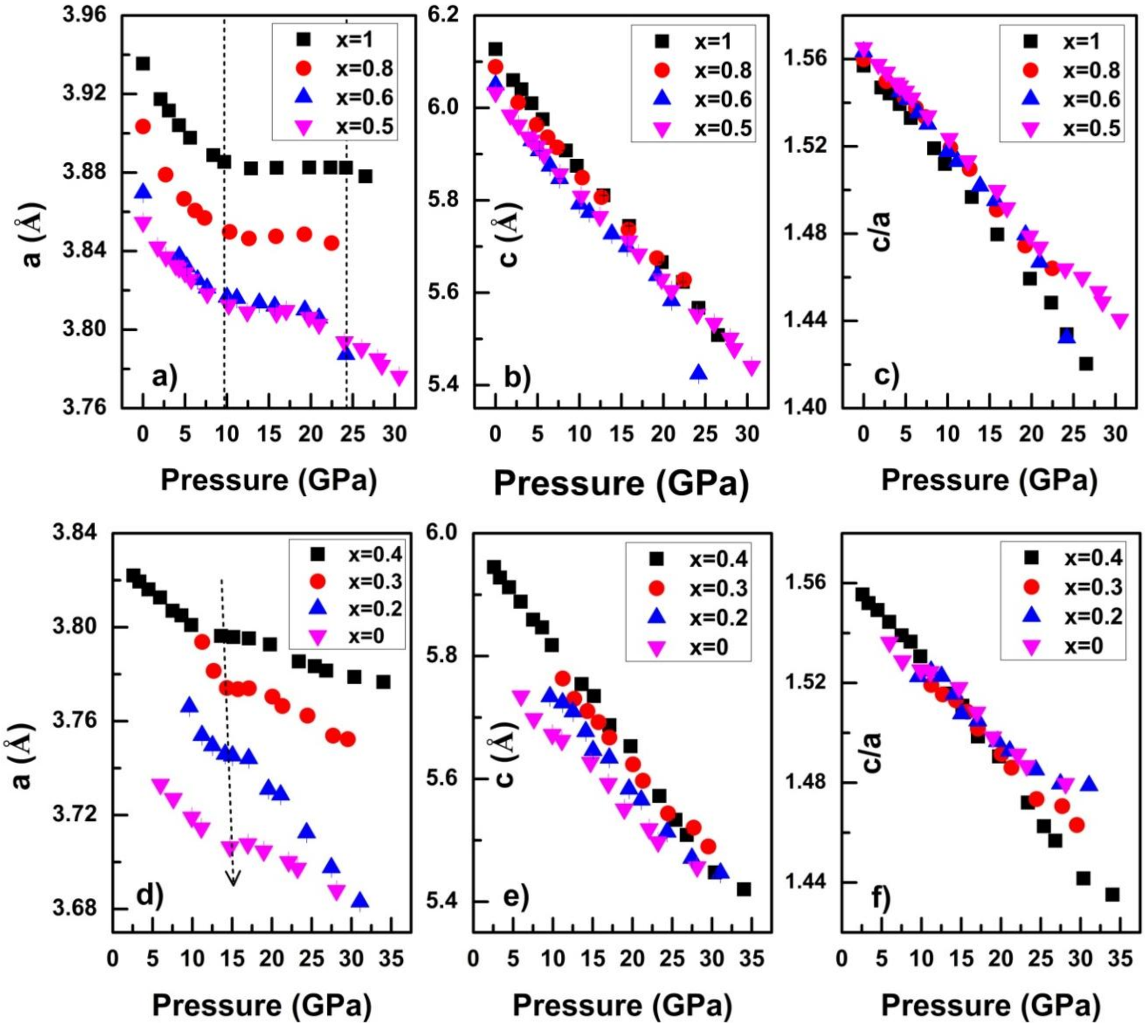

Fig. 6.11 The variation of unit cell parameters and c/a ratio of hexagonal structure with increasing pressure. a-c) for those compositions in which the hexagonal structure is stable at ATP, d-f) for those compositions in which the hexagonal structure is stable at high pressure. The dotted lines represent the pressure width where the anomaly is visible for the pure La_2O_3. The downwards dotted arrow represents the shift in onset of the anomalous compression in the high pressure phase.

Equation of state and unit cell compressibility

Compressibility data of parent and high pressure phases can be best fitted to the Birch-Murnaghan EOS (see section 2.4.3). The bulk moduli of the parent and the high pressure structures of all these oxides were obtained by fitting the experimental data to the above EOS. Only the P-V data below 10 GPa is considered during the fitting to the parent phase whereas the data above 15 GPa is considered for fitting the high pressure phases. A value of B_0'=9.8 is obtained by fitting the compressibility data of x=1, pure La_2O_3. This value has been used (fixed) to fit the compressibility data of hexagonal structures of those compositions for which the hexagonal structure is stable at ATP. In the case of cubic phase of x=0, the data is fitted to the BM-EOS and a value of B_0'= 7.4 is obtained. This value has been used (fixed) in fitting the compressibility data of all the cubic phases. These values are fixed to provide a better comparison with the end members. All other BM-EOS fitting have been carried out with a fixed value of B_0'=4. Fig. 6.12a-c represents the BM-EOS fit to the pressure dependence of the unit cell volume for the different phases of all the compositions studied in the present thesis. The bulk modulus values derived from the EOS fittings are tabulated in Table 6.3. It can be seen that, the bulk modulus of cubic structure increases from 142(5) GPa to 167(2) GPa when the composition is changed from x=0 to 0.4. For x=0.4, the bulk modulus values of monoclinic and the high pressure hexagonal structure are 168(3) and 180(8) respectively, which closely agrees with the values obtained for the cubic structure. This indicates that, at x=0.4, the cubic, monoclinic and hexagonal structures show a similar compressibility behavior. Further, the variation in the bulk modulus of the hexagonal structure with composition, x, is shown in the Fig. 6.13. A monotonous decrease in the bulk modulus can be seen with the increasing x/R_{RE} except for x=0.2 and 0.6. This decreasing trend in the bulk modulus is again attributed to the decreasing bond strength with an increase of x/R_{RE} as observed in the case of $(Eu_{1-x}Ho_x)_2O_3$ system. Such a reduction in bulk modulus for x=0.2 and 0.6 is due to the presence of maximum micro strain in these compositions. For convenience, the variation of micro strain, $\varepsilon_{r,}$ in the parent structures relative to the end member as a function of incresing x/R_{RE} is reproduced and showed as the inset of Fig. 6.13. It is evident that the strain is maximum for these compositions. This increased micro strain manifests as an internal pressure in the crystal structure leading to the reduction in the structural stability and hence a reduction in bulk modulus for x=0.2 and 0.6. Similar behavior has been seen in our earlier investigation of $(Eu_{1-x}Ho_x)_2O_3$ system and also in several other mixed RES systems [28, 132].

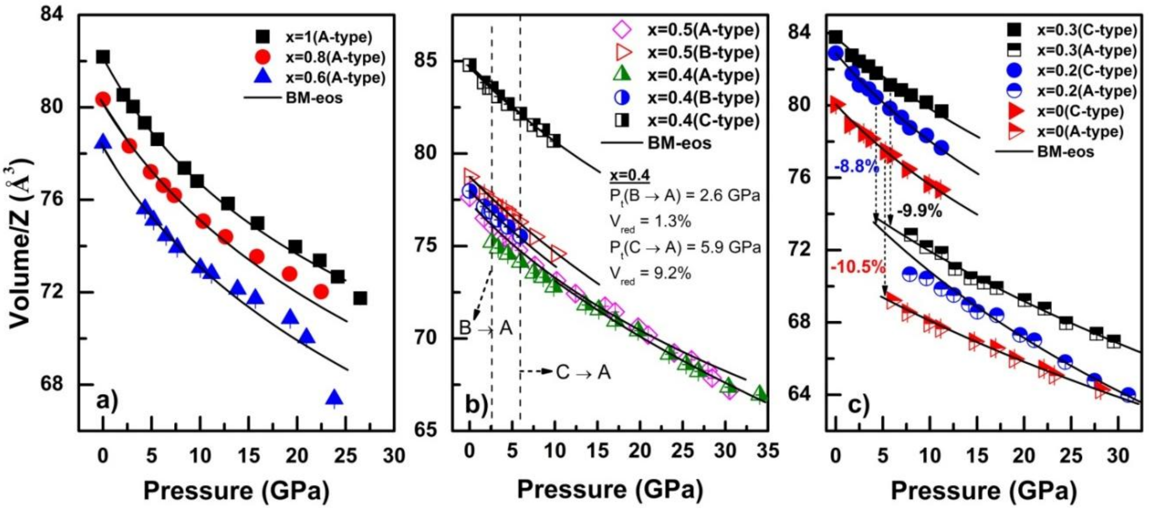

Fig. 6.12 The experimental pressure volume (P-V) data for all the investigated oxides. The solid lines indicate the Birch-Murnaghan equation of state fit to the P-V data. The fitting parameters and volume drops at the transition pressure, P_t, are tabulated in Table 6.3

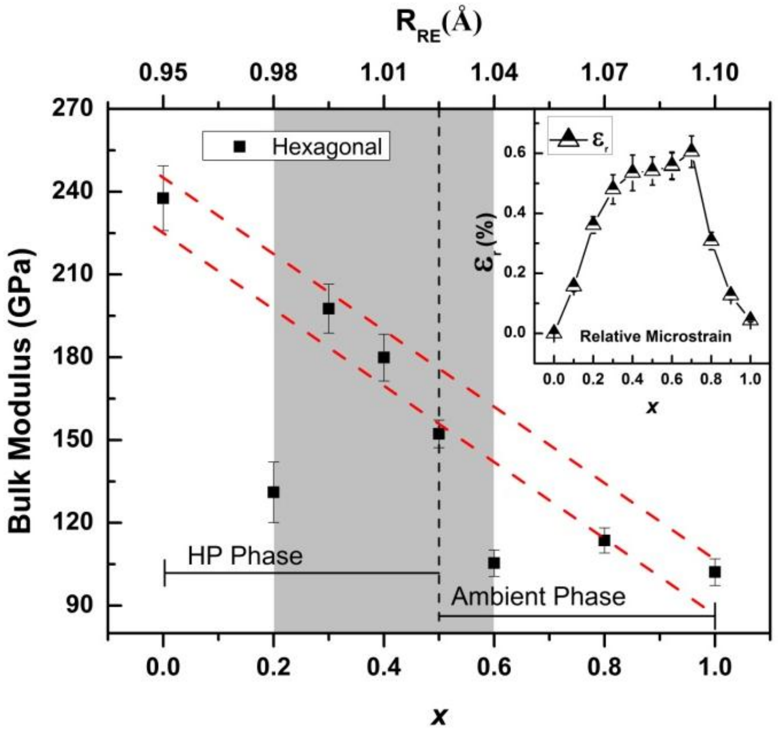

Fig. 6.13 The variation of Bulk modulus of the hexagonal structure with x/R_{RE}. The red dotted lines are guide to the eye, showing the decreasing trend of bulk modulus with increase of R_{RE}. The vertical dotted line at x=0.5 separates the hexagonal phase at ATP from the one at high pressure. The relative micro strain variation reproduced from section 6.2.2 is shown in the inset.

Table 6.3 Bulk moduli, transition pressure and volume reduction for all the mixed oxides along with the reported values of the end members. Transition pressure and volume reduction from B→A is separated by a /(slash) in respective columns.

x	**B_0(C) GPa**	**B_0(B) GPa**	**B_0(A) GPa**	**P_t GPa**	**V_{red} (%)**
0	142(5) 140(3)	-	238(12) 155(10)	5.3 5.8	10.5 10.3 ref section 4.3
0.2	133(3)	-	131(11)	4.3	8.8
0.3	173(4)	-	198(9)	5.8	9.9
0.4	167(2)	168(3)	180(8)	2.6/5.9	1.3/9.2
0.5	-	169(2)	152(5)	-	-
0.6	-	-	105(5)	-	-
0.8	-	-	113(5)	-	-
1	-	-	102(5) 113(1)[6]	- -	- -

6.3.3. Pressure concentration phase diagram

A pressure-concentration (P-*x*) phase diagram upto a pressure of 25 GPa is established from our HPXRD investigation on $(Eu_{1-x}La_x)_2O_3$ and is shown in Fig. 6.14. The stability region of the different polymorphic structures are marked with C, B and A respectively for cubic, monoclinic and hexagonal structures. The bi/triphasic regions are marked as a combination of these. Average cationic radii corresponding to each *x* is calculated using the definition of R_{RE} described earlier. Cubic structure is found to be stable for 0.95 Å ≤ R_{RE} < 0.98 Å at ambient temperature and pressure and it prefers C→ A transition with increasing pressure. A biphasic region of cubic and monoclinic structure is stable for 0.98 Å ≤ R_{RE} < 1.025 Å at ambient temperature and pressure and a C/B→A transition is preferred under pressure. Further a biphasic region of monoclinic and hexagonal structure is favoured for 1.025 Å ≤ R_{RE} <1.055 Å and the B phase progresses towrds the hexagonal A phase under pressure. A pure A phase is obtained for 1.055 Å ≤ R_{RE} ≤ 1.10 Å and the system is structurally stable under pressure.

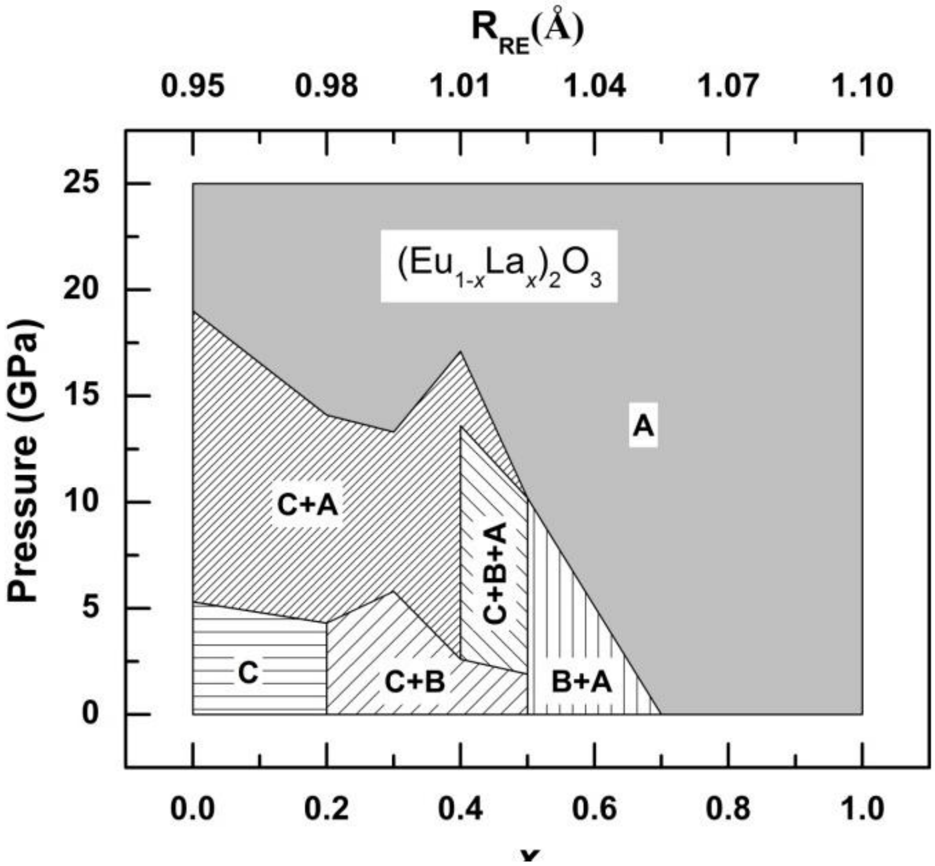

Fig. 6.14 Pressure – concentration (P-x) phase diagram for the solid solution $(Eu_{1-x}La_x)_2O_3$. Single, di and tri phasic regions of different crystal structures and their stability regions are marked accordingly.

6.4. Summary and conclusion

Solid solutions, $(Eu_{1-x}La_x)_2O_3$ ($0 \leq x \leq 1$), of rare earth sesquioxides, Eu_2O_3 and La_2O_3 has been prepared by a simple soft chemistry approach. The composition and morphology of the as synthesized oxides have been characterized using the energy dispersive spectroscopy (EDS) and scanning electron microscopy (SEM).The particles are irregular in shape and are found to be of submicron size. In order to understand the structural evolution as a function of composition, angle dispersive X-ray diffraction (ADXRD) measurements have been carried out and the structural parameters are obtained through Rietveld refinement. A structural phase transition from cubic (C-type) to monoclinic (B-type) and subsequently to the hexagonal (A-type) structure has been observed with an increasing substitution of La. A detailed analysis on the transition boundaries in terms of their average cationic radii, R_{RE}, shows that, the onset of C→ B transition is at R_{RE}=0.980 Å whereas B→A is at R_{RE}=1.025 Å. A biphasic region of cubic and monoclinic structure is observed for $0.2 \leq x \leq 0.4$ and that of monoclinic and hexagonal structure is observed for $0.5 \leq x \leq 0.6$. The micro strain and substitutional disorder induced by the difference in the size of the rare earth ions is a plausible cause for the observed phase transitions in these oxides.

The structural stability and compression behaviour of $(Eu_{1-x}La_x)_2O_3$ solid solutions were investigated under high pressure. Cubic structure is found to be stable for 0.95 Å ≤ R_{RE} < 0.98 Å at ambient temperature and pressure and it prefers C→ A transition with increasing pressure. A biphasic region of cubic and monoclinic structure is stable for 0.98 Å ≤ R_{RE} < 1.025 Å at ambient temperature and pressure and a C/B→A transition is preferred under pressure. Further a biphasic region of monoclinic and hexagonal structure is favoured for 1.025 Å ≤ R_{RE} <1.055 Å and the B phase progress towrds the hexagonal A phase under pressure. A pure A phase is obtained for 1.055 Å ≤ R_{RE} ≤ 1.10 Å and the system becomes structurally stable under pressure. The compressibily data shows a monotonous decrease in the bulk modulus of hexagonal structure with the increasing R_{RE} except for x=0.2 and 0.6. A pressure-concentration (P-x) phase diagram upto a pressure of 25 GPa is constructed from the present HPXRD investigation on $(Eu_{1-x}La_x)_2O_3$ for the first time.

Chapter 7

Summary and Future directions

7.1. Introduction

The understanding of polymorphism and related phase transitions in the rare earth sesquioxides is essential to establish more definitive structure-property correlations which would help further exploration of the functional nature of these oxides. Depending on the cation size, RESs exhibit three different structure types, C-type (small cations), B-type (medium cations) and A-type (large cations), at ATP[19, 20]. As the crystal structure of RESs depends on the size of the cation, a systematic investigation on the cation size dependant structural evolution in these RESs would be more benificial in understanding the preference of one structure type over the other. At high pressures, these oxides show different transition sequences depending on which category they belong to. If they belong to the category of small cations then a C→B→A transition is expected, on the other hand a direct C→A transition is expected for RESs of medium cation size. There are reports on the phase transition (isostructural or by a distortions to the hexagonal structure) in RESs with large cation size, but are debatable due to the contradictory reports from different studies[6-9]. Also There are, ambiguities in the high pressure behavior of RESs with hexagonal structure (large cation size)[6, 7, 9, 10, 28]. The present thesis is intended to shed light on the cation size dependent structural evolution, both at ambient and at high pressures, and to gather more understanding about the polymorphic structural phase transitions occurring in the RESs. To meet the objectives, simple RESs from cubic (small cation size), monoclinic (medium cation size) and hexagonal (large cation size) structures have been investigated at high pressures. The insights from these investigations are used to understand the high pressure behavior of solid solutions of RESs.

The present chapter discusses the important findings of this thesis and the future directions.

7.2. Summary

As a part of the high pressure experimental method, a novel internal X-ray slit assembly to carry out laboratory based HPXRD experiments in a Mao-Bell type diamond anvil cell is developed. This is achieved by introducing a lead sheet with a 100μm hole immediately below the diamond table. The new slit assembly provides high flux, improved resolution and also eliminates the cumbersome and lengthy procedure in collimating the X-ray to the sample in comparison with the previously existing slit in the lab. This slit assembly has been extensively used in collecting laboratory high pressure data of RESs in this study.

Structural stability and compression behaviour of simple rare earth sesquioxides Tm_2O_3, Eu_2O_3 and La_2O_3 crystallizing in the C-type, B-type and A-type respectively have been studied at high pressures. The results of the studies are deliberated under the Chapter 4 of the thesis. To summarize,

Tm_2O_3 samples have been studied using the HP synchrotron X-ray diffraction and HP Raman scattering. Both revealed a structural phase transition from C-type cubic to A type hexagonal structure at ~12 GPa. Further ab initio DFT studies have been carried out to support the experimental observation. The predicted transition pressure of 8 GPa is less than the experimentally observed 11.5-12 GPa. Neverthless the experimentally obtained bulk modulus of 149(2) GPa and 169(2) GPa for the cubic and monoclinic structure are found to be in good agreement with the calculated value ie, 146 GPa and 151 GPa respectively for the cubic and the monoclinic structure. An increase in the DOS near the Fermi level at the transition pressure indicated a clear signature of the structural instability in the system. The mode Grunisen parameter has been determined from the high pressure Raman data and is reported. The modes for the B-type Tm_2O_3, HP retrieved, have been assigned for the first time by comparing with the literature.

A structural phase transition from B-type to A-type has been observed for the Eu_2O_3 sample at 4.3 GPa. A detailed study on the lattice compressibility of B-type and A-type structure has been carried out. The observed low compressibility along the *b* axis followed by *c* and *a* of the B-type structure is attributed to the presence of edge sharing polyhedral arrangement along the *b* axis and the presence of voids along the *c* and a axis. An anomolous lattice compressibility characterised by the pronounced hardening along the a axis was observed in the A-type Eu_2O_3 in the 15-25 GPa pressure regime. The observed incompressibility along the a axis is found to be compensated by the doubling of the compressibility along the *c* axis. However, this anomaly was not reflected in the pressure volume data. The estimated bulk moduli are 159(9) GPa and 165(6) GPa for the parent B-type and high pressure A-type structure.

Compared to the C-type and B-type RES, the A-type La_2O_3 shows no structural phase transitions under pressure. However, the anomolous lattice compressibility observed in the case of high pressure hexagonal phase of Eu_2O_3 is also present in the A-type La_2O_3 at a comparatively earlier pressure of 9.7 GPa. This is associated with a slight expansion along the *a* axis. The substantial increase in the intensity of *100* reflection and a corresponding reduction in the intensity of *103* reflection indicated the shifting of cation from the *100* plane to the *103* plane. A sliding movement of LaO layers one over the other in opposite direction is postulated to explain the observed anomaly in the hexagonal structure. Hence in the region 9.7-19.8 GPa, the effect of pressure is to favour the LaO layer movements rather than the compression along the a axis. The obtained bulk modulus of 102(5) GPa for the A-type La_2O_3 compares well with the trend observed in the RES.

In order to understand the dependence of cation size and pressure on the different structure types, solid solutions of RESs, characterized by a smooth variation in cationic size, have been studied at high pressures. The solid solutions of Eu_2O_3 and Ho_2O_3, having similar structure (cubic) and small difference in cationic radii, and solid solutions of Eu_2O_3 (cubic) and La_2O_3 (hexagonal), having dissimilar structure and significant difference in cationic radii, have been synthesized and investigated both at ambient and at high pressures. The results obtained from the structural studies are consolidated in chapter 5 and chapter 6 of the thesis.

In the case of $(Eu_{1-x}Ho_x)_2O_3$, a single phase solid solutions, crystallizing in the C-type cubic structure is obtained in the entire range of compositions. The crystal structural parameters and their vibrational modes have been investigated and reported for the first time. A decrease in bond lengths and hardening of Raman modes observed in the high frequency range reveal an increase in bond strength, hence an increasing structural rigidity with the decrease of average cationic radii, R_{RE}. Further, disappearance of a weak low frequency band above $x = 0.8$ in conjunction with a slope change in the behavior of rare earth ion positional co-ordinate is also observed. To understand the cation size effect on the high pressure behavior of C-type RES, these solid solutions are studied under high pressures. The HPXRD studies show that, for the average cationic radii, R_{RE}, equivalent to or below 0.9164 Å, the system prefers C→B transition, whereas for R_{RE} equivalent to or above 0.9220 Å a C→A is preferred. Due to the increase in micro strain induced internal pressure, a decrease in the transition pressure and a sudden reduction in bulk modulus is observed in the $0.4 \leq x \leq 0.6$ compositions. The results obtained from the high pressure structural investigations on $(Eu_{1-x}Ho_x)_2O_3$ are consolidated and a pressure concentration phase diagram is constructed. The phase boundary between the two high pressure phases namely, A-type hexagonal and B-type monoclinic, is characterised by an average cationic radii 0.9164Å < R_{RE} < 0.9220Å.

The composition and morphology of the solid solutions of Eu_2O_3 and La_2O_3, $(Eu_{1-x}La_x)_2O_3$ have been investigated using the energy dispersive spectroscopy (EDS) and scanning electron microscopy (SEM). The particles are irregular in shape and are found to be of submicron size. Angle dispersive XRD measurements revealed a structural phase transition from cubic (C-type) to monoclinic (B-type) and subsequently to the hexagonal (A-type) structure with an increasing substitution of La. The onset of C→ B and B→A transition is at R_{RE}=0.980 Å and 1.025 Å respectively. The micro strain and the substitutional disorder induced by the difference in the size of the rare earth ion are considered as a plausible cause for the observed phase transitions in these oxides. In order to figure out the structural stability and compression behaviour, these solid solutions have been investigated at high pressures. Cubic structure is found to be stable for 0.95 Å ≤ R_{RE} < 0.98 Å at ambient temperature and pressure and transform to hexagonal structure at high pressures. A biphasic region of cubic and monoclinic structure is stable for 0.98 Å ≤ R_{RE} < 1.025 Å at ambient temperature and pressure and a C/B→A transition is preferred under pressure. Further, a biphasic region of monoclinic and hexagonal structure is favoured for 1.025 Å ≤ R_{RE} < 1.055 Å and the B phase progresses towrds the hexagonal A phase under pressure. A pure A phase has been obtained for 1.055 Å ≤ R_{RE} ≤ 1.10 Å and the system is structurally stable at high pressures. As in the case of hexagonal La_2O_3, the presence of anomalous lattice compressibility along the *a* axis of the A-type structure is confirmed in all the compositions and is considered as the intrinsic feature of the hexagonal structure of RESs . A monotonous decrease in the bulk modulus of the solid solutions with hexagonal structure with the increasing R_{RE} except for x=0.2 and 0.6 was observed. This reduction is again due to the increased internal pressure in the crystal structure as similar to that of $(Eu_{1-x}Ho_x)_2O_3$.. Using the results obtained from the investigation on $(Eu_{1-x}La_x)_2O_3$, a pressure-concentration (P-x) phase diagram upto a pressure of 25 GPa is established.

7.3. Future directions

i. Though we have proposed a pressure induced sliding of LaO layer for the observed anomalous compressibility behavior of hexagonal RES, this model needs more experimental evidence and validation. A high pressure Raman investigation and simulation of the layer movements at high pressures using the molecular dynamics would be highly beneficial.

ii. In a C→B transition of Gd_2O_3, a small fraction of the cubic phase was recovered by supplying high temperature during the reverse pressure cycle[2]. Except this, there are hardly any reports which deal with the irreversible nature. Hence, studies using the Laser Heated DAC (LHDAC) can be performed to understand the nature of irreversibility of the observed phase transitions in RESs.

iii. High pressure and high temperature (HPHT) studies on these solid solutions of RES can be carried out to understand the temperature dependent phase structure. It is known that, the monoclinic phase of medium cation sized RES is a high temperature phase. Hence, the solid solutions of Eu_2O_3 and Ho_2O_3, showing the direct C→A transition at high pressure alone, can be studied to understand the nucleation mechanism of monoclinic phase.

iv. A recent investigation on the nano Er_2O_3 at high pressures revealed a C→A transition in this RES[137]. This is in contradiction with the high pressure behavior of small cation sized RES where a C→B transition is expected. This indicates, the crystallite size may have a role in dictating the phase transitions. Hence, a systematic investigation of the crystallite size dependant high pressure phase transitions in the RESs needs a through probing.

References

1. L. Eyring, Handbook on the physics and chemistry of rare earths **3**, 337-399 (1979).
2. P. C. Sahu, L. Dayana and N. V. C. Shekar, Journal of Physics: Conference Series **377** (1), 012015 (2012).
3. Q. Guo, Y. Zhao, C. Jiang, W. L. Mao and Z. Wang, Solid State Communications **145** (5–6), 250-254 (2008).
4. S. Jiang, L.-G. Bai, J. Liu, W.-S. Xiao, X.-D. Li, Y.-C. Li, L.-Y. Tang, Y.-F. Zhang, D.-C. Zhang and L.-R. Zheng, Chinese Physics Letters **26** (7), 076101 (2009).
5. F. X. Zhang, M. Lang, J. W. Wang, U. Becker and R. C. Ewing, Physical Review B **78** (6), 064114 (2008).
6. J. P. McClure, Ph. D Thesis, University of Nevada, Las Vegas, 2009.
7. K. K. Pandey, G. Nandini, A. K. Mishra and M. S. Surinder, Journal of Physics: Conference Series **377** (1), 012006 (2012).
8. M. J. Lipp, J. R. Jeffries, H. Cynn, J. H. Park Klepeis, W. J. Evans, D. R. Mortensen, G. T. Seidler, Y. Xiao and P. Chow, Physical Review B **93** (6), 064106 (2016).
9. S. Jiang, J. Liu, L. Bai, X. Li, Y. Li, S. He, S. Yan and D. Liang, AIP Advances **8** (2), 025019 (2018).
10. L. Bai, J. Liu, X. Li, S. Jiang, W. Xiao, Y. Li, L. Tang, Y. Zhang and D. Zhang, Journal of Applied Physics **106** (7), 073507 (2009).
11. C. Kränkel, IEEE Journal of Selected Topics in Quantum Electronics **21** (1), 250-262 (2015).
12. V. Çorumlu, İ. Ermiş, S. D. Acer, T. Çifci, Y. Dağdemir and M. Ari, Journal of Materials Science: Materials in Electronics **27** (6), 5839-5845 (2016).
13. H. Guo, X. Yang, T. Xiao, W. Zhang, L. Lou and J. Mugnier, Applied Surface Science **230** (1–4), 215-221 (2004).
14. Z. Ting, O. Xin, Z. Weifeng, Y. Jiang, X. Yidong and L. Zhiguo, Journal of Physics D: Applied Physics **47** (6), 065302 (2014).
15. B. M. Walsh, J. M. McMahon, W. C. Edwards, N. P. Barnes, R. W. Equall and R. L. Hutcheson, J. Opt. Soc. Am. B **19** (12), 2893-2903 (2002).
16. G. Salek, A. Devoti, A. Garcia, M. Gaudon, V. Jubera and A. Demourgues, RSC Advances **6** (60), 55298-55306 (2016).
17. G. Azimi, R. Dhiman, H.-M. Kwon, A. T. Paxson and K. K. Varanasi, Nat Mater **12** (4), 315-320 (2013).
18. Z. Wang, Z. Quan and J. Lin, Inorganic Chemistry **46** (13), 5237-5242 (2007).
19. M. Zinkevich, Progress in Materials Science **52** (4), 597-647 (2007).
20. L. Eyring, in *Handbook on the Physics and Chemistry of Rare Earths* (Elsevier, 1979), Vol. Volume 3, pp. 337-399.
21. H. R. Hoekstra, Inorganic Chemistry **5** (5), 754-757 (1966).
22. G.-y. Adachi and N. Imanaka, Chemical Reviews **98** (4), 1479-1514 (1998).
23. R. Gillen, S. J. Clark and J. Robertson, Physical Review B **87** (12), 125116 (2013).
24. L. Petit, A. Svane, Z. Szotek and W. M. Temmerman, Physical Review B **72** (20), 205118 (2005).
25. A. V. Prokofiev, A. I. Shelykh and B. T. Melekh, Journal of Alloys and Compounds **242** (1), 41-44 (1996).
26. H. Jiang, P. Rinke and M. Scheffler, Physical Review B **86** (12), 125115 (2012).

27. S. J. Schneider and R. S. Roth, J. Res. Nat. Bur. Stand. A **64A** (4), 317-332 (1960).
28. X. Zou, C. Gong, B. Liu, Q. Li, Z. Li, B. Liu, R. Liu, J. Liu, Z. Chen, B. Zou, T. Cui, X. Bai and H. Song, physica status solidi (b) **248** (5), 1123-1127 (2011).
29. K. A. Irshad and N. V. Chandra Shekar, Materials Chemistry and Physics **195**, 88-93 (2017).
30. Y. F. Li, B. Xiao, L. Sun, Y. M. Gao, S. Q. Ma and D. W. Yi, Journal of Physics and Chemistry of Solids **103**, 49-58 (2017).
31. M. Rahm and N. V. Skorodumova, Physical Review B **80** (10), 104105 (2009).
32. S. Jiang, J. Liu, C. Lin, X. Li and Y. Li, Journal of Applied Physics **113** (11), 113502 (2013).
33. J. Gouteron, D. Michel, A. M. Lejus and J. Zarembowitch, Journal of Solid State Chemistry **38** (3), 288-296 (1981).
34. R. Haire and L. Eyring, Handbook on the Physics and Chemistry of Rare Earths **18**, 413-505 (1994).
35. G. Chen, J. R. Peterson and K. E. Brister, Journal of Solid State Chemistry **111** (2), 437-439 (1994).
36. G. Chen, N. A. Stump, R. G. Haire, J. B. Burns and J. R. Peterson, High Pressure Research **12** (2), 83-90 (1994).
37. T. Atou, K. Kusaba, Y. Tsuchida, W. Utsumi, T. Yagi and Y. Syono, Materials Research Bulletin **24** (9), 1171-1176 (1989).
38. S. Jiang, J. Liu, C. Lin, L. Bai, Y. Zhang, X. Li, Y. Li, L. Tang and H. Wang, Solid State Communications **169** (0), 37-41 (2013).
39. S. Jiang, J. Liu, X. Li, L. Bai, W. Xiao, Y. Zhang, C. Lin, Y. Li and L. Tang, Journal of Applied Physics **110** (1), 013526 (2011).
40. D. Lonappan, N. V. C. Shekar, T. R. Ravindran and P. C. Sahu, Materials Chemistry and Physics **120** (1), 65-67 (2010).
41. Q. Guo, Y. Zhao, C. Jiang, W. L. Mao, Z. Wang, J. Zhang and Y. Wang, Inorganic Chemistry **46** (15), 6164-6169 (2007).
42. C. Meyer, J. P. Sanchez, J. Thomasson and J. P. Itié, Physical Review B **51** (18), 12187-12193 (1995).
43. S. Jiang, J. Liu, C. Lin, L. Bai, W. Xiao, Y. Zhang, D. Zhang, X. Li, Y. Li and L. Tang, Journal of Applied Physics **108** (8), 083541 (2010).
44. M. I. Eremets, *High Pressure Experimental Methods*. (Oxford University Press, New York, Unites States, 1996).
45. J. C. Jamieson, A. Lawson and N. Nachtrieb, Review of Scientific instruments **30** (11), 1016-1019 (1959).
46. C. Weir, E. Lippincott, A. Van Valkenburg and E. Bunting, J. Res. Natl. Bur. Stand. A **63**, 55-62 (1959).
47. G. J. Piermarini, Journal of research of the National Institute of Standards and Technology **106** (6), 889 (2001).
48. C. H. Polsky and E. Van Valkenburg, in *Handbook of Vibrational Spectroscopy* (John Wiley & Sons, Ltd, 2006).
49. T. Johannisson, L. Tegner and C. M. Backman, *High Pressure in Research and Industry: Proceedings of the 8th AIRAPT Conference, 19th EHPRG Conference, 17-22 August 1981, Institute of Physical Chemistry, University of Uppsala, Sweden*. (Arkitektkopia, 1982).

50. G. J. Piermarini, S. Block, J. D. Barnett and R. A. Forman, Journal of Applied Physics **46** (6), 2774-2780 (1975).
51. W. A. Bassett, High Pressure Research **29** (2), 163-186 (2009).
52. A. Jayaraman, Reviews of Modern Physics **55** (1), 65-108 (1983).
53. R. Letoullec, J. P. Pinceaux and P. Loubeyre, High Pressure Research **1** (1), 77-90 (1988).
54. R. Deivasigamani, N. Gunasegran, N. Easwaran, M. Yousuf, K. V. Thomaskutty, P. C. Sahu, N. V. Chandra Shekar, N. Subramanian and K. Govinda Rajan, presented at the Advances in High Pressure Science & Technology, Bangalore, 1995 (unpublished).
55. P. C. Sahu, N. R. S. Kumar, N. V. C. Shekar and N. Subramanian, Powder Diffraction **21** (04), 320-322 (2006).
56. M. Yousuf, High Pressure in Semiconductor Physics II **55**, 381 (1998).
57. E. Soignard and P. F. McMillan, Dordrecht, 2004 (unpublished).
58. A. D. Chijioke, W. J. Nellis, A. Soldatov and I. F. Silvera, Journal of Applied Physics **98** (11), 114905 (2005).
59. S. Klotz, J. C. Chervin, P. Munsch and G. L. Marchand, Journal of Physics D: Applied Physics **42** (7), 075413 (2009).
60. B. Shukla, N. R. Sanjay Kumar, M. Sekar and N. V. Chandra Shekar, J. Instrum. Soc. India **46**, 75-77 (2016).
61. A. Hammersley, S. Svensson, M. Hanfland, A. Fitch and D. Hausermann, International Journal of High Pressure Research **14** (4-6), 235-248 (1996).
62. http://pd.chem.ucl.ac.uk/pdnn/inst2/work.htm.
63. S. Mobilio, F. Boscherini and C. Meneghini, *Synchrotron Radiation: Basics, Methods and Applications*. (Springer Berlin Heidelberg, 2016).
64. http://www.rrcat.gov.in/technology/accel/indus2.html.
65. http://pd.chem.ucl.ac.uk/pdnn/inst2/work.htm
66. http://www.rrcat.gov.in/technology/accel/srul/beamlines/index.html.
67. J. Goldstein, D. E. Newbury, J. R. Michael, N. W. M. Ritchie, J. H. J. Scott and D. C. Joy, *Scanning electron microscopy and x-ray microanalysis*. (Springer, New York, NY, 2018).
68. C. N. Banwell, *Fundamentals of Molecular Spectroscopy*, 3 ed. (McGraw-Hill Book Company Europe, England, 1983).
69. P. Larkin, *Infrared and Raman spectroscopy: principles and spectral interpretation*. (Elsevier, 2017).
70. B. H. Toby, Journal of Applied Crystallography **34** (2), 210-213 (2001).
71. A. C. Larson and R. B. Von Dreele, Los Alamos National Laboratory Report LAUR, 86-748 (2000).
72. R. A. Young, *The Rietveld Method*. (Oxford science publications, International union of crystallography, 1995).
73. hexagonal La_2O_3 (ICDD PDF No. 00-005-0602) , cubic Eu_2O_3 ICDD PDF No. 04-014-9534), monoclinic Eu_2O_3 (ICDD PDF No. 00-005-0602), cubic Tm_2O_3 (ICDD PDF No. 01-082-2416) and cubic Ho_2O_3 (ICDD PDF No. 00-067-0222).
74. M. Born and R. Oppenheimer, Annalen der Physik **389** (20), 457-484 (1927).
75. L. H. Thomas, Mathematical Proceedings of the Cambridge Philosophical Society **23** (5), 542-548 (1927).
76. E. Fermi, Rend. Accad. Naz. Lincei **6** (602-607), 5 (1927).
77. E. Teller, Reviews of Modern Physics **34** (4), 627-631 (1962).

78. P. Hohenberg and W. Kohn, Physical Review **136** (3B), B864-B871 (1964).
79. W. Kohn and L. J. Sham, Physical Review **140** (4A), A1133-A1138 (1965).
80. D. M. Ceperley and B. J. Alder, Physical Review Letters **45** (7), 566-569 (1980).
81. W. Kohn, Reviews of Modern Physics **71** (5), 1253-1266 (1999).
82. J. P. Perdew and A. Zunger, Physical Review B **23** (10), 5048-5079 (1981).
83. D. C. Langreth and M. J. Mehl, Physical Review B **28** (4), 1809-1834 (1983).
84. J. P. Perdew, J. A. Chevary, S. H. Vosko, K. A. Jackson, M. R. Pederson, D. J. Singh and C. Fiolhais, Physical Review B **46** (11), 6671-6687 (1992).
85. J. P. Perdew, K. Burke and M. Ernzerhof, Physical Review Letters **77** (18), 3865-3868 (1996).
86. W. E. Pickett, Computer Physics Reports **9** (3), 115-197 (1989).
87. G. Kresse and J. Furthmüller, Physical Review B **54** (16), 11169-11186 (1996).
88. G. Kresse and J. Hafner, Physical Review B **47** (1), 558-561 (1993).
89. H. J. Monkhorst and J. D. Pack, Physical Review B **13** (12), 5188-5192 (1976).
90. W. A. Grosshans and W. B. Holzapfel, Physical Review B **45** (10), 5171-5178 (1992).
91. P. C. Sahu, N. V. Chandra Shekar, M. Yousuf and K. Govinda Rajan, Physical Review Letters **78** (6), 1054-1057 (1997).
92. V. Kathirvel, D. Lonappan, N. V. Chandra Shekar and P. C. Sahu, Jl. of Instrum. Soc. of India **40** (3), 4 (2010).
93. B. Toby, Journal of Applied Crystallography **38** (6), 1040-1041 (2005).
94. A. C. Larson and R. B. Von Dreele, Los Alamos National Laboratory Report LAUR, 134-136 (2000).
95. ICDD PDF Nos. 04-007-0051, 00-049-1458, 04-001-2094, 00-015-0813, 01-080-6921, 00-023-1418, 00-022-0612, 00-008-0050, 01-082-2416, 01-074-1831, 01-084-5744.
96. (ICDD PDF No: 00-034-0072 and 00-041-1089).
97. X. Ren, X. Yan, Z. Yu, W. Li and L. Wang, Journal of Alloys and Compounds **725**, 941-945 (2017).
98. B. Hunter, International Union of Crystallography Commission on Powder Diffraction Newsletter **No. 20**, (Summer) (1998).
99. Crystal structure of monoclinic Tm_2O_3 (ICDD PDF No: 04-001-8728).
100. S. L. Dole, O. Hunter and F. W. Calderwood, Journal of the American Ceramic Society **60** (3-4), 167-168 (1977).
101. M. V. Abrashev, N. D. Todorov and J. Geshev, Journal of Applied Physics **116** (10), 103508 (2014).
102. N. D. Todorov, M. V. Abrashev, V. Marinova, M. Kadiyski, L. Dimowa and E. Faulques, Physical Review B **87** (10), 104301 (2013).
103. D. Yan, P. Wu, S. P. Zhang, L. Liang, F. Yang, Y. L. Pei and S. Chen, Journal of Applied Physics **114** (19), 193502 (2013).
104. W. B. White and V. G. Keramidas, Spectrochimica Acta Part A: Molecular Spectroscopy **28** (3), 501-509 (1972).
105. J. Zarembowitch, J. Gouteron and A. M. Lejus†, Journal of Raman Spectroscopy **9** (4), 263-265 (1980).
106. N. Dilawar Sharma, J. Singh, A. Vijay, K. Samanta, S. Dogra and A. K. Bandyopadhyay, The Journal of Physical Chemistry C **120** (21), 11679-11689 (2016).
107. R. J. Angel, Reviews in Mineralogy and Geochemistry **41** (1), 35-59 (2000).

108. S. V. Ovsyannikov, E. Bykova, M. Bykov, M. D. Wenz, A. S. Pakhomova, K. Glazyrin, H.-P. Liermann and L. Dubrovinsky, Journal of Applied Physics **118** (16), 165901 (2015).
109. D. Lonappan, N. V. Chandra Shekar, P. C. Sahu, B. V. Kumarasamy, A. K. Bandyopadhyay and M. Rajagopalan, Philosophical Magazine Letters **88** (7), 473-479 (2008).
110. T. Hongo, K.-i. Kondo, K. G. Nakamura and T. Atou, Journal of Materials Science **42** (8), 2582-2585 (2007).
111. Crystal structure of La_2O_3 (ICDD PDF No. 00-005-0602).
112. T. Atou, K. Kusaba, Y. Syono, T. Kikegawa and H. Iwasaki, in *High-Pressure Research: Application to Earth and Planetary Sciences* (American Geophysical Union, 2013), pp. 469-475.
113. P. Stephens, Journal of Applied Crystallography **32** (2), 281-289 (1999).
114. B. Wu, M. Zinkevich, F. Aldinger, D. Wen and L. Chen, Journal of Solid State Chemistry **180** (11), 3280-3287 (2007).
115. ICDD PDF Nos. 03-065-3182 and 04-007-6573.
116. R. D. Shannon and C. T. Prewitt, Acta Crystallographica Section B **25** (5), 925-946 (1969).
117. Z. Heiba, H. Okuyucu and Y. S. Hascicek, Journal of Applied Crystallography **35** (5), 577-580 (2002).
118. Z. K. Heiba, Y. Akin, W. Sigmund and Y. S. Hascicek, Journal of Applied Crystallography **36** (6), 1411-1416 (2003).
119. K. Momma and F. Izumi, Journal of Applied Crystallography **44** (6), 1272-1276 (2011).
120. Z. K. Heiba, M. Bakr Mohamed and H. Fuess, Crystal Research and Technology **47** (5), 535-540 (2012).
121. Z. K. Heiba, L. Arda and Y. S. Hascicek, Journal of Applied Crystallography **38** (2), 306-310 (2005).
122. D. Rodic, B. Antic and M. Mitric, Journal of Magnetism and Magnetic Materials **140–144, Part 2**, 1181-1182 (1995).
123. M. Mitric, J. Blanusa, T. Barudzija, Z. Jaglicic, V. Kusigerski and V. Spasojevic, Journal of Alloys and Compounds **485** (1–2), 473-477 (2009).
124. B. Antic, M. Mitric and D. Rodic, Journal of Physics: Condensed Matter **9** (2), 365 (1997).
125. Z. K. Heiba, M. Bakr Mohamed, M. A. Abdelslam and L. H. Fuess, Crystal Research and Technology **46** (3), 272-276 (2011).
126. M. Mitric, B. Antic, M. Balanda, D. Rodic and M. L. Napijalo, Journal of Physics: Condensed Matter **9** (20), 4103 (1997).
127. Y. Repelin, C. Proust, E. Husson and J. M. Beny, Journal of Solid State Chemistry **118** (1), 163-169 (1995).
128. A. Ubaldini and M. M. Carnasciali, Journal of Alloys and Compounds **454** (1), 374-378 (2008).
129. X. Fu, Y. Xu and J. Zhou, Journal of Materials Science **47** (4), 1697-1701 (2011).
130. G. Schaack and J. A. Koningstein, J. Opt. Soc. Am. **60** (8), 1110-1115 (1970).
131. O. L. Anderson, *Equations of State of Solids for Geophysics and Ceramic Science*. (Oxford University Press, New York, 1995).
132. L. Wang, Y. Pan, Y. Ding, W. Yang, W. L. Mao, S. V. Sinogeikin, Y. Meng, G. Shen and H.-k. Mao, Applied Physics Letters **94** (6), 061921 (2009).

133. R. Hübner, X. Sun, I. Y. Tok Alfred and Y. C. Boey Freddy, in *Zeitschrift für Kristallographie International journal for structural, physical, and chemical aspects of crystalline materials* (2009), Vol. 224, pp. 198.
134. L. Pauling, Journal of the American Chemical Society **51** (4), 1010-1026 (1929).
135. L. Pauling, *The Nature of the Chemical Bond*, 3 ed. (Cornell University Press, Ithaca, United States, 1960).
136. A. Arulraj, N. V. Chandra Shekar and P. C. Sahu, AIP Conference Proceedings **1447** (1), 131-132 (2012).
137. X. Ren, X. Yan, Z. Yu, W. Li, K. Yang, X. Wang, Y. Liu and L. Wang, Applied Physics Letters **112** (14), 143102 (2018).